Site Characterization and Modeling Considerations for Slopes Involving Fine Grained Strain-softening Soils

By

Michael Kiernan

A dissertation submitted to the Graduate Faculty of
Auburn University
in partial fulfillment of the
requirements for the Degree of
Doctor of Philosophy

Auburn, Alabama
December 11, 2021

Keywords: Strain-softening, numerical modeling, site characterization, landslides

Approved by

Jack Montgomery, Chair, Assistant Professor, Department of Civil and Environmental Engineering
J. Brian Anderson, Associate Professor, Department of Civil and Environmental Engineering
Frances O'Donnell, Assistant Professor, Department of Civil and Environmental Engineering
Lorraine Wolf, Professor, Department of Geosciences

ABSTRACT

The potential for strength loss in fine grained soils poses a significant hazard for many geotechnical projects. Damage to infrastructure attributed to strain-softening of clayey soils has been documented in many case histories involving both static and cyclic loading. For critical infrastructure projects, potential deformations due to cyclic loading are increasingly being analyzed using numerical modeling approaches, such as nonlinear deformation analyses (NDAs) for dynamic problems or strength reduction analyses for static problems. These analyses rely on material models which can represent the aspects of soil behavior important to the problem being analyzed. For any analysis method, accurate characterization of a landslide site is key to building reliable models. Supplementing traditional geotechnical explorations, such as borings, with geophysical methods can provide continuous site profiles and help identify changes in soil type or saturation across the site.

This dissertation explores the analysis of static and dynamic failures in strain-softening clays through examination of two landslides, the Fourth Avenue landslide in Anchorage, Alaska and a currently moving landslide along Interstate 65 (I-65) in Conecuh County, Alabama. Methods for characterizing and analyzing strain-softening in clays are reviewed, followed by an analysis of the Fourth Avenue landslide using the constitutive model PM4Silt, which can capture cyclic softening of clays at the field scale. Guidance is provided regarding calibration of PM4Silt and the sensitivity of the solution to the input parameters is explored. The results using PM4Silt are then compared to a total stress-based constitutive model to understand how differences in constitutive model complexity affect the results at both the element scale and field scale. Mesh dependency of the solution using both models is explored with and without regularization approaches.

The evaluation of strain-softening clays under static loading conditions is explored for the I-65 landslide using both tradition limit equilibrium and more advanced strength reduction analyses. Characterization of the materials at the site is performed using results from borings, electrical resistivity imaging and seismic data, along with laboratory testing. The results from the site characterization are used to build a site model for use in slope stability analyses. Limit equilibrium analyses are performed and the results using circular and noncircular failure surfaces are examined. The limit equilibrium results are also compared to strength reduction analyses using the Modified Hoek-Brown constitutive model to represent nonlinear strength envelopes. Sensitivity of the slope stability analysis solutions to model input parameters are studied. The results from these analyses are then used to determine a probable failure mechanism for the site and to provide recommendations for future analyses of similar landslides.

This study shows that simulations using PM4Silt can reproduce the deformation patterns and magnitudes observed at the Fourth Avenue Landslide. Effective stress-based constitutive models are found to be more appropriate than total stress-based models when element level response or a more complete estimation of deformations patterns, both inside and outside the failure mass, is required. Total stress-based models are found to be adequate if the user is primarily interested in whether failure will occur. Mesh dependency is observed in the PM4Silt model, but these effects are reduced by using a displacement-based calibration procedure. Electrical resistivity and seismic methods are shown to be reliable tools for estimating site stratigraphy and can provide information regarding the failure mass and slide plane. The Modified Hoek-Brown constitutive model is shown to be a practical option for representing nonlinear strength envelopes of soils in strength reduction method analyses as slope stability analysis results compare well with limit equilibrium analyses uses power curve fits.

ACKNOWLEDGEMENTS

I would first like to thank my advisor and committee chair Dr. Jack Montgomery for his continual guidance and support. I could not have asked for a better mentor. I would like to express my gratitude to Dr. J. Brian Anderson as his lessons and guidance over the past few years have been invaluable. I would also like to thank to my other committee members, Dr. Frances O'Donnell and Dr. Lorraine Wolf, for providing comments that added value to my dissertation. Dr. Chad Rose also deserves acknowledgement for serving as the university reader. I owe appreciation to Mengwei Xuan, for performing ring shear testing, and Patricia Carcamo Barrientos for collecting and processing seismic data used in my dissertation.

I would also like to thank my parents, Dennis and Wendy Bowers. I could have never gone back to college without their unwavering support. Most importantly I need to thank my wife, Lindsey Kiernan. She has sacrificed a great deal so that I can pursue my ambitions. You have been selfless, and I could not be more grateful.

TABLE OF CONTENTS

LIST OF FIGURES

LIST OF TABLES

CHAPTER 1: INTRODUCTION

1.1 BACKGROUND ON STRAIN-SOFTENING AND LOCALIZATION IN CLAYS

The potential for strength loss in fine grained soils poses a significant hazard for many geotechnical projects. Damage to infrastructure attributed to strain-softening of clayey soils has been documented in many case histories involving both static (e.g., Gregersen 1981, Locat et al. 2017) and cyclic loading (e.g., Shannon and Wilson 1964, Heritage 2013, Nakamura et al. 2014). Fine grained soils that exhibit a post peak reduction in strength include overconsolidated clays, high plasticity clays, and marine clays that have experienced salt-water leaching (L'Heureux et. al 2014). For static loading, such as embankment failures along roadways, slope stability is typically analyzed using the Limit Equilibrium Method (LEM) and Strength Reduction Method (SRM). These analyses do model the strain-softening process directly and materials are represented by a single strength value. Clays are also known to exhibit nonlinear strength envelopes over a wide range of stresses. LEM software packages often include power curve models to account for this nonlinearity, but options for representing this behavior in SRM analyses is limited.

For critical infrastructure projects, potential deformations due to cyclic loading are more commonly being analyzed using nonlinear deformation analyses (NDAs). These analyses rely on constitutive models that can represent the aspects of soil behavior important to the problem. Engineers tasked with evaluating liquefaction-induced deformations can choose between multiple validated constitutive models which have been implemented in user defined numerical codes (e.g., Elgamal et al. 2002) and in publicly available software programs such as FLAC (e.g., Beaty and Byrne 2011, Boulanger and Ziotopoulou 2017). Relatively few models are publicly available to evaluate potential deformations due to cyclic softening in clayey soils. The models that are available generally fall into two categories: total stress- and effective stress-based models. Total stress-based models (e.g., Anderson and Jostad 2005, Beaty and Dickenson 2015, Kiernan and Montgomery 2018) are often easier to calibrate but produce a simplified representation of true stress-strain response of these soils and cannot account for coupling between the soil and pore fluid (Taiebat et al. 2011). More complex effective stress-based models (e.g., Park 2011, Seidalinov and Taiebat 2014, Boulanger and Ziotopoulou 2018) can account for coupling between the solid and fluid phases but can be difficult to calibrate given the limited laboratory test results commonly available in practice.

Strain localization presents an additional challenge when modeling softening of clays. In the field, strains tend to localize into thin shear bands during softening, which can accelerate strength loss (Park 2011). Shear banding in clays has been observed under static loading in lab tests (Gylland et al. 2014) and in the field (Henkel and Skempton 1955). Strain localization has also been observed under both static and dynamic loading conditions in centrifuge tests using clay embankments (Kutter and James 1989) and artificially sensitive clay slopes (Park 2011). The centrifuge test results have shown that under dynamic loading more diffuse failure modes are observed, where multiple slip surfaces develop adjacent to the critical slip surface, compared with a single critical shear band under static loading. The testing performed by Park (2011) does show that for cases with larger deformations, the majority of shear strain tends to eventually localize on a single failure plane. Differences in localization behavior between static and dynamic conditions may be due to the competing effects of strain-softening under large magnitude loads and strain rate effects from dynamic loading (Kutter and James 1989, Park 2011). Localization will increase the loading on a narrow zone of clay, but faster loading rates tend to increase the peak undrained shear strength of clays (e.g., Lefebvre and LeBoeuf 1987, Lefebvre and Pfendler 1996, Boulanger et al. 1998, Diaz-Rodriguez et al. 2009). This increase in strength may cause deformations to shift to a different (weaker) failure plane and this process can repeat resulting in the development of multiple failure surfaces. The residual strength of clays is relatively unaffected by loading rate (e.g., Biscontin and Pestana 2001, Scaringi and Di Maio 2016) and so the failure tends to coalesce around a single critical failure surface.

In numerical simulations, strains tend to localize over a single row of elements resulting in a mesh dependent solution (e.g., Thakur et al. 2006). To overcome this, various approaches have been developed to introduce a length scale into the constitutive model through a regularization technique. Regularization techniques that have been applied to the problem of strain-softening clays include softening scaling (e.g., Pietruszczak and Mróz 1981, Kiernan and Montgomery 2018), non-local constitutive models (e.g., Brinkgreve 1994), interface elements (e.g., Jostad and Andersen 2004), extended finite elements (e.g., Septanika et al. 2007), rate dependent models (e.g., Park 2011) and pore fluid coupling (e.g., Thakur et al. 2006). Effective stress-based constitutive models consider coupling of the mechanical and fluid responses, but it is not clear if this is enough to overcome mesh dependency in full scale simulations. Thakur et al. (2006) report pore fluid coupling alone is not adequate in regularizing numerical solutions and proposed that rate dependence incorporated with pore fluid coupling may be more successful in reducing mesh dependency.

1.2 CHARACTERIZATION OF LANDSLIDES INVOLVING STRAIN-SOFTENING CLAY

Detailed characterization of landslide sites is important to build models for use in slope stability analyses. An accurate assessment of site stratigraphy is needed as well as an estimation of soil properties that represent the scenario to be modeled. Site stratigraphy is typically estimated from drilling explorations that provide data only at discrete points (DeJong et al. 2016). Geophysical methods offer a means to supplement boring data and can often provide a more detailed estimation of the subsurface. Electrical resistivity imaging (ERI) provides 2D or 3D profiles of subsurface resistivity distribution which can be used to delineate clayey soils from sandy soils and rock (e.g., Loke 2004, Perrone et al. 2014). Seismic methods provide an estimate of elastic moduli via shear wave velocity measurements and are sometimes used to provide 2D or 3D profiles (e.g., Jongmans and Garambois 2007).

Standard penetration testing (SPT) can provide strength estimates for sandy soils but is not well suited for estimating properties of sensitive clays (Holtz et al. 2013). Cone penetration testing (CPT) can provide detailed information regarding soil layering and mechanical properties of soils but cannot be used at sites with significant amounts of gravel or rock intervals (Schmertmann 1978). Direct simple shear tests can provide an estimate of drained (Bjerrum and Landva 1966) or undrained fine grained soil strength under cyclic (Vucetic and Dobry 1987, Boulanger and Idriss 2007) or monotonic loading (e.g., Woodward-Clyde 1982, Mayne 1985). Ring shear testing is typically used to estimate drained strength parameters of clays (e.g., Wright et al. 2007, Xuan et al. 2021) and can provide a means for calibrating material models to expected soil behavior such as nonlinear strength, modulus reduction and damping behavior, and cyclic softening.

The data from each of these methods should be used to inform each other in a site characterization program to create geologically based models for the purpose of analysis (DeJong et al. 2016). Comparison of geophysical results to SPT or CPT provides ground truth for interpretation of soil type, site stratigraphy and geologic features identified from ERI or seismic profiles. Seismic data can also be used to guide interpretation of ERI results as soft saturated clay and fractured limestone below the water table may both exhibit low resistivity, but soft clay is expected to have a lower velocity. In-situ and lab test results can provide additional information related to soil behavior and strength in soil layers identified from the geotechnical and geophysical investigations. This study uses traditional geotechnical explorations and lab testing to characterize the Fourth Avenue landslide site to build a site model for use in dynamic simulations. This study also integrates the use of geophysics with traditional geotechnical explorations and lab testing to characterize a landslide site along a roadway embankment.

1.2.1 Drilling and Standard Penetration Tests (SPT)

Drilling and sampling is primarily used to identify soil types and site stratigraphy and can provide an estimate of the water table location for landslide sites. Standard penetration testing (SPT) testing is commonly performed during drilling providing highly disturbed soil samples for classification purposes and an estimate of coarse grained soil strength based on SPT blow counts. The SPT is performed by driving a standard split-spoon sampler a distance of 45.7 cm (18") with a 63.5 kg (140 Lbf) hammer dropped a height of 76 cm (30") (Holtz and Kovacs 1981). The measured blow count (N) is the number of blows to drive the sampler the final 30 cm (12"). The measured blow count can then be corrected to account for overburden stress, energy ratio based on hammer type, rod length, borehole diameter and sampler liners (Bowles 1996). This process provides a corrected blow count [$(N_1)_{60}$] that allows data collected using different equipment, or at different depths, to be compared more accurately. Correlations have been developed to estimate coarse grained soil properties from SPT $(N_1)_{60}$ values. However, SPT correlations can be difficult to develop for soft soils due to the low blow counts and existing correlations cannot be used to estimate residual strength of clays. SPT tests are typically conducted at intervals of about 1.5m (5 ft). The SPT is therefore suitable for estimating stratigraphy, water table location and coarse grained soil properties at landslide sites. SPT data at this site is only used to determine relative density, effective stress friction angles, and unit weights for coarse grained soil layers.

1.2.2 Cone Penetration Tests

Cone penetration testing (CPT) is a quasi-static test where a small cone is slowly (2 cm/s) pushed into the soil (Schmertmann 1978). No sample is collected, but cone tip resistance, sleeve friction, and pore pressure are commonly measured during testing (Roberston 1990). Measurements are recorded at intervals of about 5 cm compared to the SPT at intervals of 1.5 m, providing nearly continuous data with depth. Correlations are available to estimate soil behavior type as well as undrained shear strength (S_u) and sensitivity (S_t) of fine grained soils (e.g., Robertson 2009, 2016). Pore pressure measurements can also be used to estimate the water table location. The CPT is relatively fast and can provide precise estimations of soil stratigraphy, but problems can arise in very dense soils or if gravels, cobbles, or boulders are encountered (Schmertmann 1978). The CPT is therefore suitable for estimating stratigraphy, water table location and some properties of both coarse and fine grained layers at landslide sites.

1.2.3 Electrical Resistivity Imaging (ERI)

Electrical resistivity geophysical techniques typically utilize four electrode arrays placed on the ground surface to provide an estimate of subsurface resistivity distribution (Loke 2004). Known amperage is injected through two current electrodes and the resulting potential difference is measured between different pairs of potential electrodes. An ‘apparent’ resistivity distribution is then calculated using the known injected current, the potential voltage difference and a geometric factor that is related to the geometry of the selected array. This ‘apparent’ resistivity is the value of resistivity that would be measured for the given electrode geometry in a half space of homogenous resistivity. An inversion procedure is then required to estimate the true subsurface resistivity distribution from the measured ‘apparent’ resistivity values. More details on resistivity theory are outlined in Loke (2004).

Inversion of the resistivity data is performed by converting the measured field data, such as potential difference (ΔV) and injected current (I), to an ‘apparent’ resistivity $(\rho_a = kR)$ using the measured resistance $(R = \Delta V / I)$ value and a geometric factor (k) that depends on the geometry of the current ($C1$ and $C2$) and potential electrodes ($P1$ and $P2$) (Loke 2004). These calculated ρ_a values represent the resistivity of a homogenous half space that would be measured for a given geometric factor (Loke 2004). Numerical inversion of the measured data is then required to obtain an estimate of the true subsurface resistivity distribution. The resistivity of geologic materials depends primarily on mineral content, porosity, and degree of saturation (Loke 2004).

Inversion techniques seek to find a synthetic subsurface model that produces an apparent resistivity distribution that closely matches the measured data. The starting synthetic model for inversion of the data in this dissertation is commonly a homogenous finite element mesh with a resistivity equal to the average of the measured apparent resistivity values. The model is then updated to reduce the difference between the measured data and the model. The inversion procedure produces a non-unique estimate of the subsurface resistivity distribution as an infinite number of synthetic models may exist that fit the data equally well (DeGroot-Hedlin and Constable 1990). Resistivity data for this dissertation is inverted in EarthImager2D (AGI 2014) using a smoothness-constrained procedure known as Occam’s inversion (AGI 2014). Occam’s inversion seeks to find solutions that are never more complex than the true subsurface resistivity distribution

(Constable et al. 1987) by producing the smoothest possible model whose apparent resistivity distribution fits the measured data to an a-priori Chi-squared statistic (AGI 2014).

The information gained from ERI surveys can be useful for characterizing landslides in several different ways. Failure planes in landslides sometimes occur near an interface between different soil strata with contrasting resistive properties which can be identified using ERI (Jongmans and Garambois 2007). Perrone et al. (2014) compiled data from 63 different landslide case histories involving ERI surveys to identify common resistive features associated with the failure masses. The failure mass is found to be less resistive than the surrounding soils in 65% of the case histories but this is primarily due to the clayey soils with high water contents involved in these failures. The failure mass is more resistive than the surrounding soils in 22% of the case and not well defined in the remaining 13% of cases. ERI has also been found useful for identifying critical layers in landslides involving marine clays. Marine clays can attain high degrees of sensitivity due to saltwater leaching. Leaching of the saltwater makes the clay less conductive allowing the most sensitive zones in a marine clay slope to be identified as having relatively higher resistivity values than surrounding clays in an ERI profile (L'Heureux et. al 2014). Disadvantages associated with ERI include loss of resolution with depth, results that are not easily correlated to geotechnical properties, and an inversion process is required which produces a non-unique solution (Jongmans and Garambois 2007).

1.2.4 Multi-Channel Analysis of Surface Waves (MASW)

Multi-channel analysis of surface waves (MASW) is a seismic-based geophysical method, which takes advantage of the velocity and frequency characteristics of surface waves. A benefit of seismic methods is they provide a direct estimate of shear wave velocity (Uhlemann et al. 2016). MASW surveys typically utilize 24 or 48 evenly spaced geophones to record ground velocity

(Reynolds 2011). Active surveys can be performed using an input source, such as sledgehammer on a plate, and have investigation depths of about 10 m to 40 m depending on site conditions (Park et al. 1999). Passive surveys do not use an active source but instead measure vibrational noise from the environment such as traffic vibrations along a highway and can measure much deeper than active surveys (Park and Miller 2008). More details regarding MASW data collection can be found in Park et al. (1999).

Shear wave velocities are estimated from MASW results through an inversion process (Reynolds 2011). A vital step when processing MASW data is to determine a dispersion curve which relates wave energy to frequency content and phase velocity (Park et al. 2011). Dispersion curves are often generated using commercial software, but the user is still required to select an appropriate dispersion curve which can be difficult. Several modes may exist in a dispersion curve (Gao et al. 2015) but proper selection of the fundamental mode is important for an accurate estimation of shear wave velocity (Wathelet 2005). Once the dispersion curve is selected it is used in an inversion procedure to obtain a shear wave velocity profile. The inversion procedure requires estimations of an initial earth model, soil density and Poisson's ratio (Park et al. 1999). Further details regarding inversion of MASW data can be found in Wathelet (2005).

Resolution of the MASW profiles near the surface depends on the shortest wavelengths (highest frequencies) that can be represented in the dispersion curve which is controlled by the geophone spacing (Lin et al. 2004). The shortest wavelength required to detect a surface layer of a given thickness is equal to twice the minimum surface layer thickness and the geophone spacing required to estimate shear wave velocity is equal to the surface layer thickness (Park et al. 1999). This means that a geophone spacing of 1 m is required to detect surface layers as small as 1 m thick and to represent wavelengths as small as 2m. The shortest wavelength represented in the dispersion curve may also be estimated from the highest frequency on the selected dispersion curve and the corresponding velocity. Soil layers thinner than the geophone spacing may be detected at greater depths due to the interaction of surface waves with differing frequencies and velocities. The maximum depth of investigation for a MASW survey depends on the longest wavelength (lowest frequencies) measured by the geophones which depends on the frequency characteristics of the subsurface and the seismic source and the survey length (Taipodia et al. 2018).

Seismic methods are often used in conjunction with ERI to investigate landslides (e.g., Donohue et al. 2009, Jongmans et al. 2009, Huntley et al. 2019). Jongmans and Garambois (2007) compiled data from geophysical landslide investigations and show that the seismic velocities of the failure mass tend to be lower than the surrounding soils, allowing the geometry of the failure mass to be estimated using seismic methods. Disadvantages of seismic methods include complex processing, which is time consuming and subject to user interpretation. Data collected along roadways may also be affected by vibrational traffic noise (Kiernan et al. 2021). For surveys along highways, the effects of traffic noise can be reduced by timing shots to occur during relatively quiet periods between large vehicles. As with ERI, the inversion process for seismic data is uncertain and the inverted solution is non-unique (e.g., Foti et al. 2009).

1.2.5 Direct Simple Shear Tests (DSS)

Direct simple shear (DSS) tests can be used to determine the peak undrained shear strength of fine grained soils, but do not typically provide much post-peak information to estimate softening rate or residual strength due to limitations in the maximum strain level. Soil specimens are sealed in a latex membrane and enclosed in a stack of metal rings to prevent radial displacement (Duncan et al. 2014). Clay soils can be consolidated prior to shearing to represent the stress history and normalized soil engineering properties (SHANSEP) (Ladd and Foot 1974) of the clay under varying levels of consolidation stress. DSS results are typically represented as the peak undrained shear strength normalized by vertical effective stress ($S_{u,pk}/\sigma'_v$) versus overconsolidation ratio (*OCR*). Undrained shear strengths obtained from DSS tests are typically lower than those obtained in triaxial compression tests (Mayne 1985), but DSS tests are thought to better represent horizontal shear stresses induced by earthquake shaking (Idriss 1985).

1.2.6 Ring Shear Tests (RS)

Ring shear tests are typically used to estimate the drained strength of fine grained soils using specimens reconstituted to a desired water content (Stark and Vettel 1992). Details regarding ring shear testing for drained strength parameters can be found in Stark and Vettel (1992), Kennedy (2019), ASTM D6467, and ASTM D7608. Undrained strengths can also be obtained if constant volume ring shear (CVRS) devices are used (e.g., Stark and Contreras 1996). Ring shear tests provide an estimate of fully softened and residual shear strengths. The residual strength obtained from ring shear tests is defined as the minimum shear resistance of a reconstituted specimen where the shear resistance becomes constant as shear displacement becomes large (ASTM D6467). Residual strength of clays occurs at a state where the soil fabric is broken down and the clay particles become oriented parallel to the failure plane. The measured residual strength in ring shear testing therefore accurately represents in-situ soil in a pre-existing failure plane that has experienced significant displacement (Stark et al. 2005).

The fully softened strength is defined by ASTM D7608 as the maximum shear resistance of the reconstituted ring shear specimen. Skempton (1970) defines the fully softened strength as the peak drained shear strength of a clay soil under normally consolidated conditions. Stark et al. (2005) also describe the fully softened strength as the peak strength of normally consolidated clays, but Skempton (1977) states that this does not represent the in-situ peak strength of intact overconsolidated clays. Xuan et al (2021) summarize conclusions from landslide case history studies performed by others that suggest that that first time drained failures in clay slopes typically controlled by the fully softened strength. The fully softened strength is therefore used to investigate first time failure of the landslide described in Chapter 4.

1.3 ANALYSIS OF LANDSLIDES INVOLVING SENSITIVE CLAY

Slope stability analyses are typically performed using Limit Equilibrium Methods (LEM) or Strength Reduction Methods (SRM) for cases involving static loading of slopes. LEM typically uses the method of slices to solve for a factor of safety (FS) and a search algorithm to find the critical failure surface. Assumptions regarding the location and shape of the slip surface as well as the interaction of interslice forces are required for LEM. SRM does not require a search algorithm to find the critical failure surface and slices are not utilized so assumptions regarding interslice forces are not needed. The critical failure surface in SRM is determined through calculation of element stresses in the numerical model. Slope stability analyses involving dynamic loading can be analyzed using LEM or SRM, but the use of nonlinear deformation analyses (NDAs) is needed to estimate displacements. The full equations of motion are solved in NDAs in order to estimate deformation patterns and magnitudes. Advanced constitutive models may also be utilized in NDAs to represent element level soil behavior that is important to the problem being analyzed. This study utilizes LEM and SRM to analyze stability of a shallow slope failure along an embankment under static loading. NDAs are used to estimate deformation patterns and magnitudes in field-scale simulations of the Fourth Avenue landslide.

1.3.1 Limit Equilibrium Method (LEM)

LEM analyses may be used to determine the FS of a slope. Traditional LEM typically utilize a method of slices which divide the slope into a number of vertical slices (Duncan et al. 2014). The vertical slices are then used to compare driving stresses to shear resistance at different points on a given failure plane which are used to determine equilibrium of the slope. An iterative procedure is then implemented which analyzes various possible slip surfaces to determine a critical failure surface, which is commonly the surface with the minimum value of FS (Duncan 1996).

Various procedures are available for performing the method of slices calculations and each makes assumptions regarding the shape of the failure surface and interslice forces acting between each slice. A few of these methods are discussed below but many more are procedures exist and are readily available for use in common slope stability programs (e.g., Rocscience 2021). The Ordinary Method of Slices assumes a circular failure surface, neglects interslice forces, and satisfies only moment equilibrium about the center of the circle (Duncan et al. 2014). The simplified Bishop's method assumes a circular failure surface, assumes interslice forces act horizontally, and satisfies moment equilibrium about the center of the circle as a well as vertical force equilibrium for each slice (Duncan et al. 2014). Spencer's method can account for slip surfaces of any shape and assumes forces between each slice act parallel to each other at some unknown inclination (Duncan 1996). The inclination of the interslice forces is determined through solution of equilibrium equations (Spencer 1967). Spencer's method satisfies equilibrium of moments as well as equilibrium of forces in the horizontal and vertical directions (Spencer 1967).

1.3.2 Strength Reduction Method (SRM)

The strength reduction method (SRM) may be used to determine the FS of a slope (Itasca 2016). The SRM is a form of limit equilibrium analysis that is typically implemented within a finite element (FEM) or finite difference (FDM) program (Duncan et al. 2014). To perform the calculation, multiple analyses of a single slope are performed using different strength values in order to find the boundary between equilibrium and instability. This boundary is often defined using a velocity or displacement threshold or if the numerical solution fails to converge (Duncan et al. 2014). The FS of the slope may then be defined as the ratio of the actual shear resistance of the soil to the shear resistance required to produce the unstable condition (Dawson et al. 1999). SRM has several advantages over traditional limit equilibrium based on the methods of slices. No slices are utilized so assumptions regarding interslice forces are not required (Duncan et al. 2014). SRM also does not require any assumptions or search algorithm for the critical failure surface as the location of the failure plane in FEM and FDM analyses is determined through calculation of element stresses in the numerical model (Griffiths and Lane 1999). Slope displacements and velocities can be plotted using SRM, but these values should be used to assess instability and identify failure surfaces and not to estimate actual deformation magnitudes or rates.

1.3.3 Nonlinear Deformation Analysis (NDA)

NDAs typically utilize FEM or FDM that differ from the methods discussed above in that they solve the full equations of motion to estimate deformation patterns and magnitudes (e.g., Beaty and Dickenson 2015, Boulanger and Montgomery 2016, Mohammadi and Taiebat 2016, Zabolotnii et al. 2021). NDAs require a numerical solver (e.g., FEM or FDM) and a constitutive model to represent the material behavior. Constitutive models have been developed that can simulate complex soil behaviors such as liquefaction (e.g., Dafalias and Manzari 2004, Beaty and

Byrne 2011, Boulanger and Ziotopoulou 2017) and strain-softening of clays (e.g., Thakur 2007, Beaty and Dickenson 2015, Zabolotnii et al. 2021). NDAs can also handle dynamic loading (e.g., Beaty and Dickenson 2015, Montgomery 2015) as well as interaction between the soil and reinforcing elements (e.g., Yu et al. 2015, Chaudhary et al. 2016), deep foundations (e.g., Chen and Martin 2002, Ghorbani et al. 2019) or surface structures (e.g., Reza Tabatabaiefar et al. 2013, Pinzón et al. 2020).

All NDAs in this study utilize the commercial 2D FDM software Fast Lagrangian Analysis of Continua (FLAC V8.0) (Itasca 2016). FLAC implements an explicit time-stepping solution scheme to solve algebraic equations as opposed to implicit matrix-based techniques typically utilized with FEM. This results in an uncoupled solution at each timestep but coupling between mechanical and hydraulic forces and interactions between zones can occur over multiple timesteps. Timesteps are calculated within FLAC to be smaller than physical wave speeds so that information cannot pass between zones over the duration of the timestep allowing fully coupled processes to be simulated. The finite difference mesh in FLAC is composed of quadrilateral zones that are dived into two sets of constant strain triangular elements that are overlain within each quadrilateral zone. Once material properties and boundary conditions are assigned, FLAC solves dynamic equations of motion to determine nodal displacements and velocities that are used to determine stresses or forces throughout the model based on constitutive stress-strain relationships. The explicit solution scheme makes FLAC more computationally efficient for nonlinear problems involving large deformations, but less efficient for small strain problems, compared to implicit methods. More detailed information regarding the formulation and implementation of FLAC is provided in Itasca (2016).

1.4 BRIEF INTRODUCTION OF SELECTED CONSTITUTIVE MODELS

Selection of appropriate constitutive models that accurately represent key aspects of soil behavior for a given modeling scenario are important for any NDA regardless of the software or solution scheme used. The sections below describe the two primary constitutive models utilized for NDAs performed in FLAC as part of this study. The first is an advanced effective stress-based model named PM4Silt. The second is a simple total stress-based Mohr-Coulomb model (RSSMC) that can represent strain-softening and implements a regularization technique to reduce mesh dependency of the solution.

1.4.1 PM4Silt

PM4Silt is an effective stress-based, critical state compatible, bounding surface plasticity model developed by Boulanger and Ziotopoulou (2018) to simulate the dynamic response of low plasticity silts and clays. The yield surface is defined as a cone in principal stress space. PM4Silt defines the critical state line in void ratio (e) versus the natural logarithm of mean effective stress [ln(p')] space (Figure 1-1a) by a reference intercept (Γ) at p'=1kPa, slope (λ), and current mean effective stress (p'). The slope (λ) is related to slope the virgin compression line obtained from consolidation tests and intercept (Γ) is related to the undrained shear strength at critical state ($S_{u,cs}$). The critical state line for PM4Silt is also defined to pass through the origin in deviatoric stress (q) versus p' space (Figure 1-1b) with a slope (M) that is related to the critical state friction angle (ϕ'_{cv}). PM4Silt utilizes a bounding surface (Figure 1-1b) which allows the peak strength to exceed the critical state strength. The bounding surface is defined to pass through the origin in q versus p' space with a slope related to the state parameter (ξ) and a user defined PM4Silt input parameter $n^{b,wet}$. The bounding surface then collapses to the critical state surface as the state parameter approaches zero. A summary of PM4Silt input parameters used in this study and are outlined in

Table 1-1 and further details on these input parameters can be found in Boulanger and Ziotopoulou (2018).

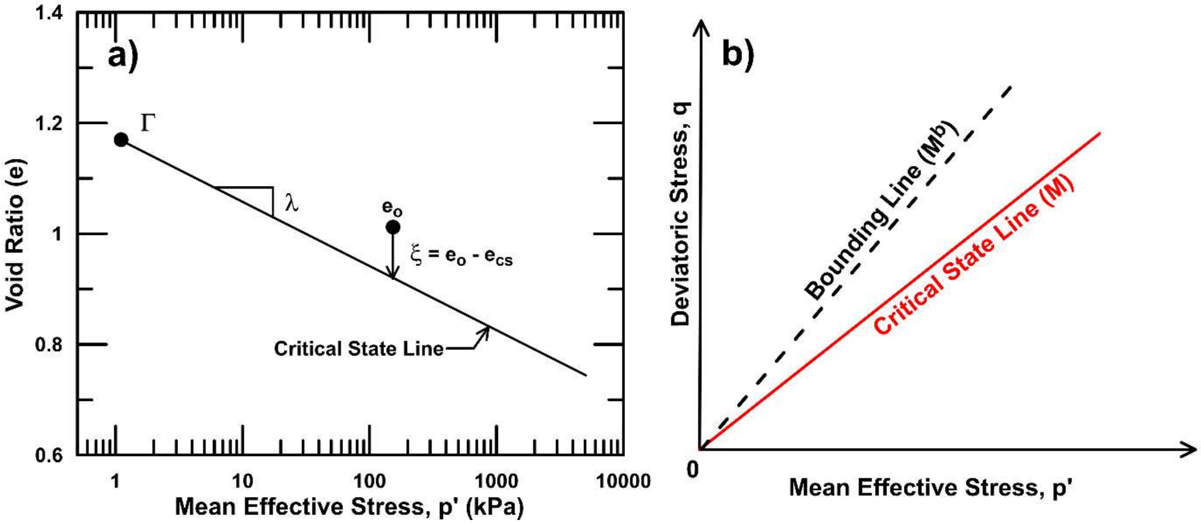

Figure 1- 1: Example critical state and bounding lines for PM4Silt in (a) e-log(*p'*) and (b) *q-p'* space (After Boulanger and Ziotopoulou 2018)

PM4Silt does not incorporate a cap on the yield surface and is therefore not capable of modelling phenomena related to consolidation processes. This constitutive model is not designed to represent strength anisotropy and currently only formulated for plane strain applications. PM4Silt is an effective stress-based model, but does not implement any additional regularization techniques to address mesh dependency. Oathes and Boulanger (2020) incorporated rate dependence into PM4Silt but found that that mesh dependence is only reduced prior to the onset of softening. Further details on the PM4Silt constitutive model can be found in Boulanger and Ziotopoulou (2018).

Table 1- 1: Description of PM4Silt input parameters utilized in this dissertation (after Boulanger and Ziotopoulou 2018)

Input Parameter [FLAC Designation]	Description
$S_{u,cs,eq}/\sigma'_v$ [Su_Rat]	Required parameter that is used to position the critical state line (i.e., sets Γ) to obtain the specified undrained shear strength at critical state for the current void ratio ($S_{u,cs,eq}/\sigma'_v$). This parameter is used to set the residual drained strength ratio in the current study.
h_{po} [h_po]	Required contraction rate parameter that adjusts contraction rates and can be adjusted to obtain target cyclic resistance ratios. This parameter is used to calibrate to desired softening rate in the current study
G_o [G_o]	Required primary variable controlling small strain shear modulus G_{max}. G_o should be chosen to match estimated shear wave velocities according to $G_{max} = \rho V_s^2$
h_o [h_o]	Variable that adjusts ratio of plastic modulus to elastic modulus. This variable can be adjusted to improve G/G_{max} and damping behavior for model calibrations
e_o [e_o]	Initial void ratio primarily affects how volumetric strains translate to changes in the state parameter. Changing value does not affect undrained shear strength as the critical state line is positioned relative to e_o based on the specified undrained shear strength
λ [lambda]	The slope of the critical state line in e-ln(p) space. Default value is 0.060. Changing λ influences how the state parameter (ξ) varies with changing p, but the influence on model response is not strong because most behaviors depend on ξ/λ.
$n^{b,wet}$ [n_bwet]	Specifies the degree to which the peak $S_{u,pk}$ may exceed the critical state $S_{u,cs}$ increases with decreasing $n^{b,wet}$. This parameter is used to calibrate to peak undrained shear strength in the current study

1.4.2 Regularized Strain-Softening Mohr-Coulomb (RSSMC) Constitutive Model

The RSSMC model is a total stress-based Mohr-Coulomb model which has the ability to model strength loss during shearing and utilizes a regularization technique to reduce dependency on mesh size. The RSSMC model is formulated as a user defined model (UDM) and is compiled as a dynamic link library (DLL) file for use in the commercial finite difference software FLAC version 8.0 (Itasca 2016). The basic formulation of RSSMC is a modified version of the Mohr-Coulomb based strain hardening/softening implemented in FLAC V8.0. Details regarding the formulation and implementation of the Mohr-Coulomb and strain hardening/softening constitutive models is presented in Itasca (2016). Mohr-Coulomb based strain-softening models have been used by Anastasopoulos et al. (2007) to model fault rupture propagation through sand and Potts et al. (1990) to study progressive failure in dam involving a strain-softening clay foundation layer. Further details of the formulation and implementation of the Mohr-Coulomb and strain hardening/ softening constitutive models are discussed in Itasca (2016).

The version of the model (RSSMC) used in this study consider only reductions of the Mohr-Coulomb cohesion intercept with increasing plastic deviatoric shear strain. The friction angle is set to zero. The cohesion is initially set to the peak undrained shear strength ($S_{u,pk}$) and softens to the residual strength ($S_{u,res}$). The amount of softening is specified by the sensitivity (S_t) which is equal to the ratio of $S_{u,pk}$ to $S_{u,res}$. The amount plastic shear strain required to fully soften the material is specified by the remolding strain (γ_{rem}). Further details regarding the representation of strain-softening in RSSMC can be found in Kiernan (2019).

The RSSMC model utilizes a regularization technique to reduce mesh dependency of the numerical solution based on the softening-scaling approach proposed by Pietruszczak and Mráz (1981). This technique scales the softening rate based on the element size to maintain a constant ratio of softening rate to element size. The approach used in the study linearly scales the element level plastic deviatoric strain (γ_{elem}) to estimate the strain magnitude that would occur in a shear band with thickness h_{sb} for the same magnitude of shear displacement. The softening in each element is dependent on the strain scaled to the shear band thickness and the cohesion is reduced according to the specified S_t value. Further details regarding the implementation of the softening-scaling approach in RSSMC can be found in Kiernan (2019).

Previous researchers have successfully used similar softening-scaling approaches to reduce mesh dependency of solutions involving localization of sands (e.g., Anastasopoulos et al. 2007) and clays (e.g., Brinkgreve 1994, Andresen and Jostad 1998). A major challenge with this approach is that the remolding strain (γ_{elem}) and the shear band thickness (h_{sb}) must be defined by the user. These parameters are difficult to quantify from standard laboratory tests, but reasonable values can be assumed from previous research (e.g., Stark and Contreras 1998, Thakur 2007, Gylland et. al. 2014).

1.4.3 Modified Hoek-Brown (MHB)

Soil shear strength is numerical analyses is often modeled using a linear strength envelope, but soils are known to display nonlinear strength envelopes over a large range of stresses (VandenBerge and McGuire 2019). The Modified Hoek-Brown (MHB) model provides an option for representing a nonlinear strength envelope, but is formulated for use with rocks. VandenBerge et al. (2018) studied the use of MHB to represent drained strength envelopes of different soils and found that MHB can reasonably represent nonlinear strength envelopes, but the input parameters cannot be estimated from correlations described in the model formulation (Hoek et al. 2002) which are specific to rocks. This study will examine the ability of MHB to represent nonlinear strength envelopes of clay in SRM analyses. The MHB failure criterion is represented by Equation 1-1. The MHB model is calibrated to ring shear data to represent observed nonlinear failures envelopes. Further details on the formulation and implementation of MHB can be found in Itasca (2016).

$$\sigma_1 = \sigma_3 + \sigma_{ci} \left[m_b \left(\frac{\sigma_3}{\sigma_{ci}} \right) + s \right]^a \quad (1\text{-}1)$$

Where:

σ_1 and σ_3 are principal stresses

σ_{ci} is the unconfined compressive strength

m_b, a, and s are material constants used in calibration

This dissertation utilizes MHB in FLAC simulations using SRM where the strength of the soil is changed until the slope becomes unstable. The nonlinear MHB failure criteria in FLAC is represented in SRM analyses by the Mohr-Coulomb equation using estimates of the local cohesion intercept (c_c) and friction coefficient ($tan(\phi_c)$) to produce linear envelopes that are tangent to the MHB failure envelopes for each individual zone. The values of c_c and $tan(\phi_c)$ are then divided by a common reduction factor until instability occurs and this reduction factor is defined to be equal to FS. Strengths throughout the model are still assigned according to the nonlinear MHB strength envelope but the reduction factor used in SRM is not directly applied to the calibrated MHB parameters. Further details on the implementation of SRM using MHB in FLAC can be found in Itasca (2016).

1.5 MOTIVATIONS AND GOALS

The potential for strength loss in fine grained soils poses a significant hazard for many geotechnical projects. Damage to infrastructure attributed to strain-softening of clayey soils has been documented in many case histories involving both static and cyclic loading. For critical infrastructure projects, potential deformations due to cyclic loading are increasingly being analyzed using numerical modeling approaches, such as nonlinear deformation analyses (NDAs) for dynamic problems or strength reduction method (SRM) analyses for static problems. These analyses rely on constitutive models which can represent the aspects of soil behavior important to the problem being analyzed. Despite these known hazards to infrastructure, constitutive models to analyze deformations and stability of slopes underlain by strain-softening clays are relatively limited. Users are often forced to choose between a limited number of advanced effective stress-based models and more simplified total stress-based models. However, choosing the appropriate model type for a given site is not always straightforward. Understanding the effects of the chosen mesh size on the numerical solution is also important to interpretation of numerical results. Another limitation of slope stability analyses is the ability to accurately characterize a landslide site to build site models for use in analyses. Traditional geotechnical explorations provide data only at discrete point forcing engineers to interpolate the information in between. Geophysical methods offer a promising option for more detailed site characterization when combined with traditional geotechnical explorations.

The primary motivation of this study is to advance methods to characterize and analyze slopes underlain by strain-softening clays. The first goal is to examine the ability of the recently published PM4Silt constitutive model to estimate deformation magnitudes and deformations in numerical simulations of the Fourth Avenue landslide. This will provide a validation case history for PM4Silt and illustrate benefits and limitations of the model. The second goal of this study is to investigate mesh size dependency of the PM4Silt solution and propose a displacement-based calibration is proposed to reduce these effects. This will provide a simple method for reducing mesh size dependency of the PM4Silt model. The third goal of this study to provide guidance as to when it may be necessary to use a more advanced effective stress-based constitutive model versus a total stress-based model. This will assist practicing engineers in determining cases where total stress-based models are adequate and when additional time and resources should be invested into the use of advanced effective stress-based models. The fourth goal of this study is to integrate the use of geophysical methods with traditional geotechnical explorations to characterize a landslide site along a roadway embankment in Alabama. This will outline the integration of geophysics with traditional geotechnical explorations and lab testing for characterization of landslide sites underlain by strain-softening clays. The fifth goal of this study is to examine the ability of the MHB model to represent nonlinear strength envelopes of clays in SRM analyses. This will provide guidance for use of the MHB model, which is formulated for use with rocks, in slope stability analysis involving clays. The last goal of this study is to compare the results of LEM and SRM analyses for a static driven landslide. This will help determine the probable failure mechanism at the site and highlight benefits and limitations of each analysis method.

1.6 RESEARCH OBECTIVES

Primary research objectives for this dissertation are outlined by chapter below.

Chapter 2:

- Develop a procedure for calibrating the PM4Silt for strain-softening clays
- Validate the PM4Silt constitutive model against a well-documented case history of an earthquake-induced landslide in a sensitive clay deposit.

Chapter 3:

- Examine the ability of a displacement-based calibration procedure to reduce mesh dependency of the PM4Silt solution
- Identify differences in results for simulations using an advanced effective stress-based constitutive model and a total stress-based strain-softening model

Chapter 4:

- Use geophysical exploration tools to characterize a landslide in a strain-softening clay deposit
- Examine the ability of the Modified Hoek-Brown constitutive model to represent nonlinear drained strength envelopes in SRM analyses of a landslide underlain by strain-softening clay
- Compare stability analysis methods for static landslides in strain-softening clays.

1.7 DISSERTATION ORGANIZATION

This dissertation is divided into 5 chapters as follows:

- *Chapter 1 – Introduction*: This chapter provide a general background on characterization and analysis of landslides involving sensitive clays. Motivation for this research and objectives are provided. The organization of content within this dissertation is also outlined.
- *Chapter 2 – Numerical Simulations of the Fourth Avenue Landslide Considering Cyclic Softening*: This chapter provides validation for the PM4Silt constitutive model using full scale simulations of the Fourth Avenue Landslide. Simulation results using PM4Silt are compared to observed displacements and to results from previous studies using different constitutive models. The effects of different model calibrations are studied as well as the influence of input motion and mesh density.
- *Chapter 3 – Comparison of Total and Effective stress-based Constitutive Models Regarding Strain-softening of Fine Grained Soils:* This chapter compares the ability of a total stress-based strain-softening Mohr-Coulomb model and the effective stress-based

PM4Silt model to represent cyclic softening of a sensitive clay layer during earthquake loading. The ability of each constitutive model to reproduce observed earthquake deformations from the Fourth Avenue Landslide at the field scale are compared. Differences in the element level behavior between each model are also examined to understand the differences in the field scale behavior.

- *Chapter 4 – Characterization and Analyses of a Slow-moving Landslide in Strain-softening Clay*: This chapter focuses on the characterization and analysis of landslide site underlain by a strain-softening clay in which repeated failures are observed with relatively small movements. The characterization is performed by integrating results from electrical resistivity imaging (ERI) and multi-channel analysis of surface waves (MASW) with traditional geotechnical explorations to develop a representative cross-section for the landslide and ring shear results to measure the drained fully softened and residual strengths of the critical zone.
- *Chapter 5 – Summary, conclusions, and future research*: This chapter summarizes the work performed and research conclusions contained in this dissertation. Relevance of research findings to practicing engineers and potential options for research are discussed.

CHAPTER 2: NUMERICAL SIMULATIONS OF THE FOURTH AVENUE LANDSLIDE CONSIDERING CYCLIC SOFTENING

This chapter is based on a paper published by Michael Kiernan and Jack Montgomery in the *Journal of Geotechnical and Geoenvironmental Engineering.*

Kiernan, M., and Montgomery, J. (2020). "Numerical Simulations of Fourth Avenue Landslide Considering Cyclic Softening." Journal of Geotechnical and Geoenvironmental Engineering (ASCE), 146(10), 04020099.

This chapter is altered from the version submitted to the *Journal of Geotechnical and Geoenvironmental Engineering* to minimize repetition and maintain a logical organization of content. My primary contributions to the chapter included: (i) evaluation of available geotechnical testing results, selection of soil parameters and constitutive model calibrations, (ii) literature review, (iii) design and implementation of numerical model, (iv) processing, analyzing, and interpretation of the results, and (v) preparation of initial draft and most of subsequent writing.

2.1 INTRODUCTION

This chapter investigates the ability of PM4Silt to model earthquake-induced deformations caused by strain-softening of a mildly sensitive clay. It is critical to ensure that a soil constitutive model can reproduce aspects of soil behavior that are important to the scenario being modelled as well as understand the limitations of the model. The process of evaluating a constitutive model's capabilities against experiments or well-documented case histories is called validation and it is important to validate every model under a wide range of loading scenarios and input parameters. The PM4Silt model formulators (i.e., Boulanger and Ziotopoulou 2018) have validated that the model can represent aspects of cyclic behavior of low plasticity silts observed in lab testing in single element direct simple shear simulations. The focus of this chapter is to validate the ability of PM4Silt to model cyclic softening at the field-scale in simulations of the Fourth Avenue landslide.

All simulations in this chapter are performed using the commercial finite difference software FLAC 8.0 (Itasca 2016). The Fourth Avenue landslide in Anchorage, which was initiated by the 1964 Great Alaska Earthquake, is used for this evaluation. PM4Silt is an effective stress-based critical state compatible bounding surface plasticity model formulated to represent the dynamic behavior of low plasticity silts and clays (Boulanger and Ziotopoulou 2018). The model calibration procedures and results are discussed. Simulation results using PM4Silt are compared to the observed displacements and to results from previous studies using different constitutive models. The effects of different model calibrations are studied as well as the influence of input motion and mesh density. The results demonstrate that PM4Silt can capture the general response of the Fourth Avenue landslide, although the results are sensitive to the input parameters and show some dependency on mesh size.

2.2 FOURTH AVENUE CASE HISTORY

The 1964 Great Alaska Earthquake is a magnitude (M_w) 9.2 event that occurred when 700 km of subduction zone interface between the Pacific and North American plates ruptured near Prince William Sound, Alaska (Ichinose et al. 2007). No ground motions recordings for this event are available, but witness accounts and damage patterns suggest that two to three minutes of strong shaking and a peak ground acceleration (PGA) of about 0.15-0.20 g in the Anchorage area

(Moriwaki et al. 1985). The earthquake led to extensive ground failures in Anchorage that was approximately 120 km from the epicenter.

Cyclic softening of a sensitive marine clay known as Bootlegger Cove Clay (BCC) presents a common link between some of the predominant ground failures such as the Fourth Avenue, L Street, and Government Hill landslides (Shannon and Wilson 1964). The Fourth Avenue slide is selected for this study because it has a well-defined failure mechanism and the site has been extensively characterized by previous researchers. A simplified cross-section of the Fourth Avenue slide showing the site stratigraphy with observed deformations is presented in Figure 1 (after Shannon and Wilson 1964).

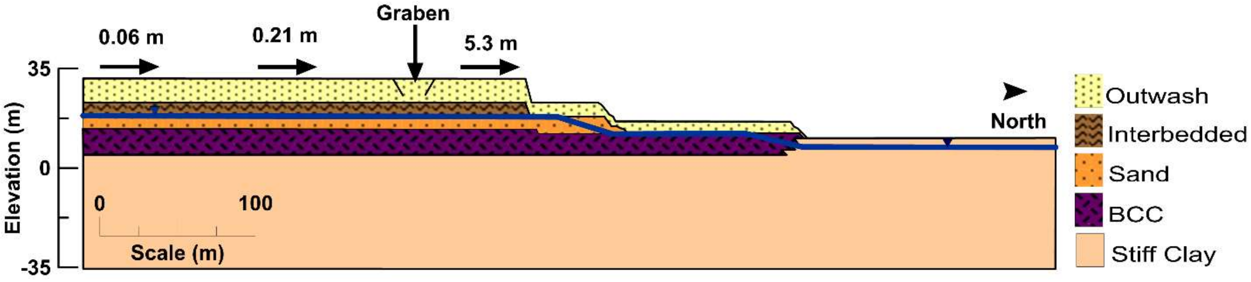

Figure 2- 1: Cross-section of the Fourth Avenue landslide showing observed deformations (after Shannon and Wilson 1964)

The general geology in the Anchorage area consists of Pleistocene deposits overlying tertiary rock (Hansen 1965). The Pleistocene deposits include moraine deposited glacial tills, estuarine-marine or lacustrine-marine deposited silty clays (including BCC), and fluvioglacial deposits consisting largely of outwash sand and gravel (Hansen 1965). The outwash layer at the surface of the Fourth Avenue site (Figure 2-1) consists primarily of very dense gravels and sands (Idriss 1985). The interbedded zone underlying the outwash consists of alternating layers of overconsolidated BCC with thin lenses of silts and fine sands (Shannon and Wilson 1964). Below the interbedded zone exists a sand layer comprised of dense fine silty sand (Shannon and Wilson

1964). Beneath the sand layer is a relatively uniform deposit of BCC which is lightly overconsolidated and classifies as a low plasticity silty clay with PI values below 20 and LL values around 35 (Shannon and Wilson 1964, Moriwaki et al. 1985). The BCC layer pinches out near the toe of the slope. This transition to zero thickness is simplified as a stepped contact in the current analyses (Figure 1; note the exaggerated vertical scale) due to the size of the quadrilateral elements used in the simulations. The lower stiff clay is a silty clay with coarse sand (Shannon and Wilson 1964), that underlies the BCC and crops out north of the slope.

The original investigations performed by Shannon and Wilson (1964) indicated that the failure plane likely existed near the boundary between the sand layer and underlying BCC and could not determine whether the failure was caused by softening of the BCC or liquefaction of the sand layer. Further investigations and analyses of the Fourth avenue slide (Woodward-Clyde 1982, Idriss 1985) found liquefaction of the sand layer to be unlikely given the high blow counts in this layer and concluded that undrained strength loss in the BCC caused the failure. Failure of the BCC was also found to be responsible for the Turnagain (Updike 1984) and L-Street (Moriwaki et al. 1985) landslides which both occurred during the Great Alaska Earthquake.

2.3 FOURTH AVENUE SOIL PROPERTIES

Site investigations for the Fourth Avenue site consist primarily of standard penetration tests (SPTs), cone penetration tests (CPTs), field vane tests and index tests performed by Shannon and Wilson (1964) and Woodward-Clyde (1982). Shear wave velocities for the site are estimated using results from downhole tests performed nearby (Nath et al. 1997). The selected shear wave velocity profile for this study (Figure 2-2) is consistent with the profile developed by Beaty and Dickenson (2015) based on the Nath et al. (1997) downhole tests.

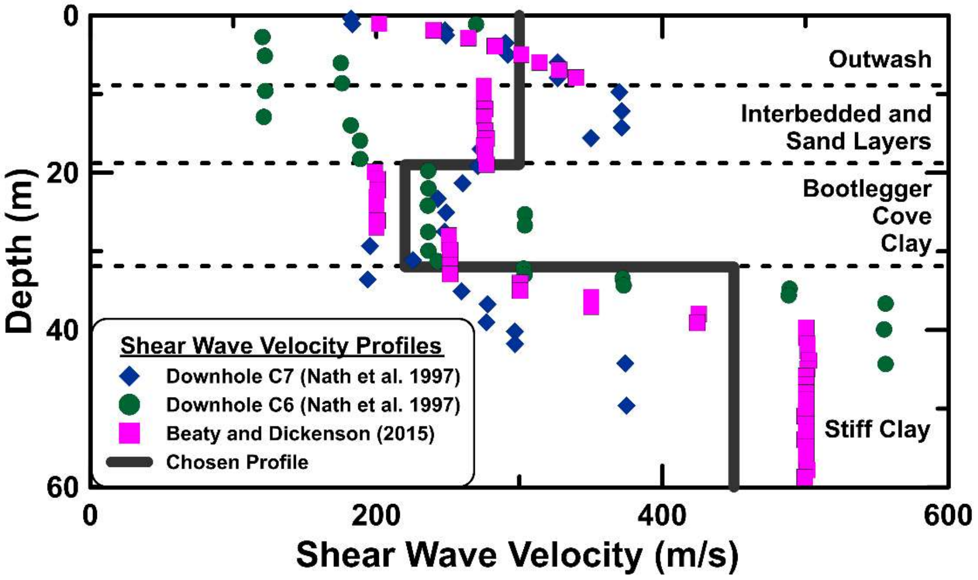

Figure 2- 2: Selected shear wave velocity profile beneath ground surface for Fourth Avenue site

Most of the previous characterizations (Woodward-Clyde 1982, Idriss 1985, Stark and Contreras 1998) have focused on identifying the strength characteristics of the BCC as it is considered the critical layer at the site. Figure 2-3 shows a plot of BCC peak and residual undrained shear strength versus effective stress for different tests. The values reported by the original authors have been plotted here without additional corrections. Stark and Contreras (1998) note that the peak strengths from the field vane tests should likely be reduced by a factor of 0.83-0.71, which would bring these strengths within the range of the other tests. The value of the peak undrained shear strength ratio ($S_{u,pk}/\sigma'_v$) ranges from about 0.18 to 0.30 based on the direct simple shear (DSS) and constant volume ring shear data. Woodward-Clyde (1982) developed an undrained strength envelope for the BCC using (DSS) tests (Equation 2-1).

$$\frac{S_{u,pk}}{\sigma'_v} = 0.185(OCR)^{0.78} \qquad (2\text{-}1)$$

They estimated the overconsolidation ratio (OCR) of the BCC ranged from 1.2-1.5 with an average value of 1.3. This would imply a $S_{u,pk}/\sigma'_v$ value of 0.23, which is consistent with the average of the data. The scatter in the $S_{u,pk}/\sigma'_v$ values in Figure 2-3 is likely due to spatial variability, differences in overconsolidation, disturbance, differences in loading conditions, and differences in loading rates between the different tests. The test methods shown in Figure 2-3 (DSS, ring shear and field vane) are considered appropriate for estimating shear strengths for cases where the failure plane is primarily horizontal (Duncan et al. 2014), but do not account for possible anisotropy of the strength under different loading conditions. The failure mechanism at the Fourth Avenue landslide is primarily horizontal translation within the BCC (Idriss 1985) and so the effects of strength anisotropy are assumed to be small for this case history.

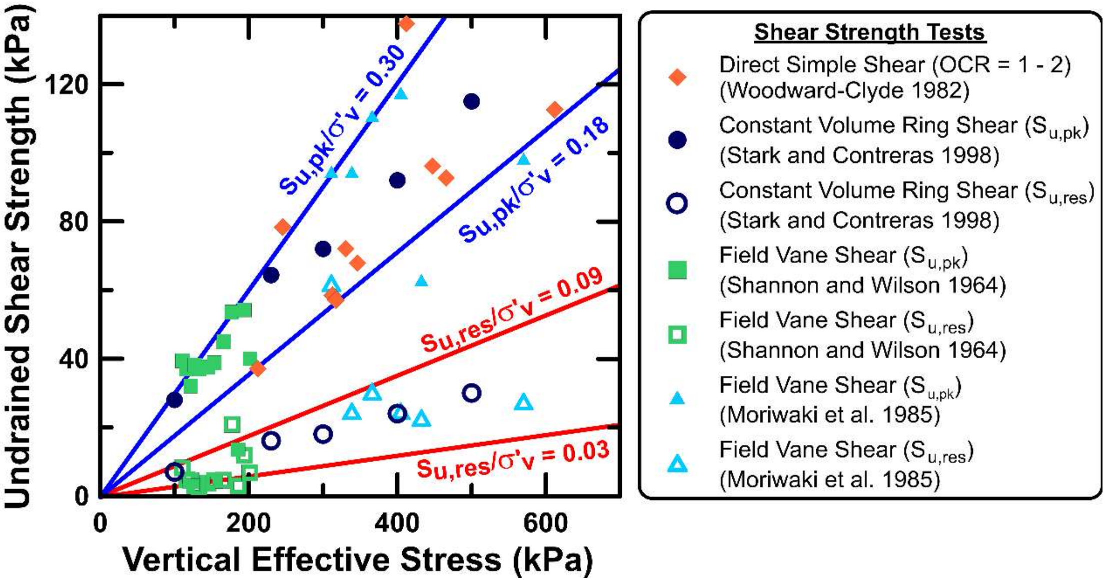

Figure 2- 3: Peak and residual undrained shear strength versus vertical effective stress for different testing methods performed at or near Fourth Avenue site

Residual undrained shear strengths reported by different authors are also shown in Figure 2-3. The residual strength ratio ($S_{u,res}/\sigma'_v$) is shown to vary from about 0.03 to 0.09, with an average of 0.06. The amount of strength loss in strain-softening soils is often described by sensitivity (S_t) which is the ratio of the peak undrained shear strength to residual undrained shear strength. Idriss

(1985) reported S_t for the BCC ranged from 2 to 11 with a mean value of 3. This range of values is consistent with the data in Figure 2-3 for a $S_{u,pk}/\sigma'_v$ value of 0.23.

The test results shown in Figure 2-3 are static tests and used strain rates that are significantly lower than observed during earthquakes. As previously discussed, the peak undrained strength of clays tends to increase with increasing strain rate (e.g., Lefebvre and LeBoeuf 1987, Lefebvre and Pfendler 1996, Boulanger et al. 1998, Diaz-Rodriguez et al. 2009), while the residual strength is relatively independent of loading rate (e.g., Biscontin and Pestana 2001, Scaringi and Di Maio 2016). When using rate independent constitutive models, like PM4Silt, this increase in peak strength is often accounted for using a strain rate factor. Values of this strain rate factor typically range from 1.2 - 1.4 (e.g., Idriss and Boulanger 2008, Beaty and Dickenson 2015).

There is considerable scatter in the strength values shown in Figure 2-3 and uncertainty in selecting a strain rate factor further increases this scatter for the peak strength. Recognizing this range of data, the current study uses peak undrained shear strength ratio for earthquake loading ($S_{u,pk,eq}/\sigma'_v$) of 0.23, 0.26 and 0.30. This range represents the lower half of the data shown in Figure 2-3 but is more consistent with the strength envelope developed by Woodward-Clyde (1982). The lower peak strengths are expected to result in higher displacements and are used for the baseline analyses to see if the model could reproduce large displacements when using a reasonable, but conservative strength estimate. The higher peak strengths are considered in the sensitivity analyses. Residual undrained shear strength ratios of 0.075 and 0.045 are considered in the baseline analyses to represent the middle of the range of $S_{u,res}/\sigma'_v$ values shown in Figure 2-3.

Selection of the softening rate, or the interval of strain over which the material softens, is an important part of calibrating the model, but selecting this value involves considerable uncertainty. Beaty and Dickenson (2015) investigated softening rates ranging from 10% to 240%, but found that displacements consistent with site observations were only obtained when strength loss occurred abruptly using faster softening rates near 10%. Idriss (1985) suggested that the residual strength is mobilized at a displacement of 15 cm, but it is uncertain how this displacement would relate to shear strain within the BCC. Stark and Contreras (1998) found that peak strengths were reached at shear displacements ranging from 1.1 mm to 1.8 mm in constant volume ring shear tests, while residual strengths were reached at shear displacements ranging from 55 mm to 130 mm. They note that these displacements are likely smaller than would be required to mobilize these strengths in the field. Based on these data, this study investigates softening rates that fully soften the BCC in 10% and 20% total strain. These softening rates mean that residual strengths would be reached after about 13 cm (fast softening) and 26 cm (slow softening) of element level shear displacement for the average BCC element heights of about 1.3m used in the baseline mesh.

Less characterization data is available for the other zones at the Fourth Avenue site. The interbedded zone (Figure 2-1) contains layers of stiff BCC, sandy silts and silty clays. The BCC layers in this zone are estimated to have OCRs between 3 and 4 (Idriss 1985). No OCR data is available for the deeper stiff clay layer. CPT results in the stiff clay (Woodward-Clyde 1982) indicate $S_{u,pk}/\sigma'_v$ ranges from 0.10 to 0.60 using the average empirical cone factor (N_{kt})value of 14 (Robertson 2009). Considering both of these results, a $S_{u,pk}/\sigma'_v$ of 0.35 is selected for the interbedded zone and stiff clay layer.

The strength characteristics of the outwash and sand layers are estimated based on $(N_1)_{60}$ values calculated from SPTs performed by Shannon and Wilson (1964). Average $(N_1)_{60}$ values of about 45 and 50 are observed in the outwash and sand layers. This indicates these layers are dense and not likely susceptible to liquefaction, as previously discussed by Idriss (1985). These values are used later to calibrate the PM4Sand constitutive model (Boulanger and Ziotopoulou 2017) that is used to model these layers in the numerical simulations.

2.4 NUMERICAL SIMULATIONS

The simulations in this study are performed using the two-dimensional (2D) commercial finite difference software Fast Lagrangian Analysis of Continua (FLAC 8.0, Itasca 2016). All simulations are performed using plane strain conditions. The mesh used in the baseline analyses consists of 14,602 elements with an average height of 1.3 m in the BCC layer. The extents for each soil layer used in the simulations can be seen in Figure 2-1. The simulations are performed in stages. In the first stage, the model is brought to static equilibrium by building each row of elements, assuming dry conditions. A Mohr-Coulomb elastic-plastic constitutive model is used throughout the model to establish static equilibrium using an identical drained friction angle and small-strain shear modulus to those used in the dynamic simulations. The water table is then slowly raised to the desired height by applying a constant head boundary condition to each side of the model. This procedure results in a normally consolidated stress profile, which is not likely to be consistent with the lateral stress conditions at the site. To account for this, coefficient of lateral earth pressures (K_o) values for the BCC, interbedded, and stiff clay are estimated according to equation 2-2 (Meyerhof 1976), assuming $K_{0,NC}$ = 0.45, the OCR = 1.3 for the BCC and OCR = 3.5 for the interbedded and stiff clay layers.

$$K_{0,OC} = K_{0,NC}(OCR)^{0.5} \tag{2-2}$$

The K_o values of the sand and outwash layer are assumed to be 0.5. Poisson's Ratio (v) values are then adjusted in each layer to achieve the desired K_0 values during static stress initialization. During these initial simulation phases, the base of the model is fixed and roller boundaries restricting horizontal movement are applied at the sides.

After the model reached static equilibrium, the constitutive model is changed to either PM4Silt or PM4Sand, depending on the layer, and the earthquake shaking is applied. The Poisson's ratio is returned to 0.3 during the dynamic phase. During dynamic loading, pore water is allowed to flow and the bulk modulus of the pore fluid is set to be equal to the bulk modulus of water ($2.0*10^9$ Pa). In the dynamic phase, free-field boundary conditions are applied to the sides of the model and quiet boundaries in both the vertical and horizontal directions are applied along the base of the model to minimize the effects of reflected waves (Itasca 2016). The vertical and horizontal input motions are applied as stress time histories along the base of the model. Details on the formulation and implementation of these boundary conditions are provided in Itasca (2016).

2.4.1 Earthquake Input Motions

No ground motion recordings exist from the Great Alaska Earthquake, so recordings from other large magnitude subduction zone quakes are used in this study. All recordings are downloaded from the Center for Engineering Strong Motion Data database (CESMD 2017). Pre-processed recordings from four stations are selected from the 2010 M8.8 Chile earthquake. Raw recordings from two stations are selected from the 2011 M9.0 Tohoku earthquake in Japan and processed according to the guidelines provided by Ancheta et al. (2013). The two horizontal components from each station are considered independently for a total of 12 ground motion records. Selected properties of each motion are shown in Table 2-1.

Table 2- 1: Summary of earthquake recordings used

Earthquake Name	Station ID	CH	Mw	Epicentral Distance (km)	Scale Factor	PGA of Scaled Motion (g)	Arias Intensity (m/s)	V_{S30} (m/s)
Japan 3/11/2011	FKS 015	NS	9.0	227	1.25	0.35	2.5	696
		EW			1.0	0.22	1.4	
	TCG 001	NS	9.0	253	0.70	0.22	1.2	580
		EW			0.70	0.29	1.8	
Chile 2/27/2010	CUR	NS	8.8	171	0.60	0.28	3.8	525
		EW			0.55	0.23	3.3	
	HUA	L	8.8	136	0.43	0.16	1.4	530
		T			0.43	0.19	1.6	
	LLO	L	8.8	274	0.50	0.22	1.2	370
		T			0.40	0.16	1.6	
	TAL	L	8.8	113	0.70	0.33	5.6	550
		T			0.60	0.25	3.9	

A target spectrum for the Fourth Avenue site was previously developed by Beaty and Dickenson (2015) using ground motion prediction equations for subduction zone events (Figure 2-4). The horizontal components of ground motions are linearly scaled to match this target spectrum between periods of 0.6 to 1.0 seconds, which roughly encompasses the low strain period of the site (Beaty and Dickenson 2015). Vertical and horizontal components of each motion are used with the same scaling factor applied to each. The spectral accelerations at short periods are higher in the scaled motions than the target spectra (Figure 4), but the range of acceleration values from the scaled records is consistent with results from regional ground motion simulations of this event performed by Mavroeidis et al. (2008). The range of PGAs for the scaled records varies between 0.16g to 0.35g which is consistent with the estimates of Moriwaki et al. (1985) and the simulations performed by Mavroeidis et al. (2008).

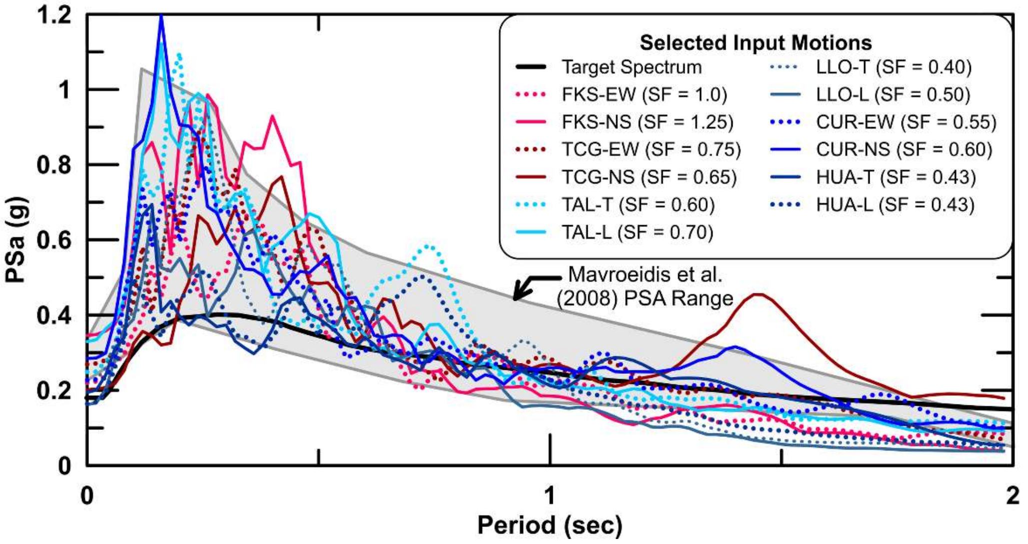

Figure 2- 4: Pseudo-spectral acceleration (PSa) response spectra for scaled motions compared to Fourth Avenue landslide target spectrum developed by Beaty and Dickenson (2015) and PSa range estimated by Mavroeidis et al. (2008)

2.5 CONSTITUTIVE MODEL CALIBRATION

The two main constitutive models used in this study are the bounding surface plasticity models, PM4Silt (Boulanger and Ziotopoulou 2018) and PM4Sand (Boulanger and Ziotopoulou 2017). PM4Silt is used to simulate the dynamic response of the BCC, the stiff clay and the interbedded zone. PM4Sand is used to simulate the dynamic response of the sand and outwash layers. Descriptions of the constitutive models can be found in Chapter 1.4 and the calibration processes for each of the layers are described in the following sections. Pre-earthquake stresses are initialized using the elastic-plastic Mohr-Coulomb constitutive model with an identical drained friction angle and small-strain shear modulus to those used in the dynamic simulations. The coefficient of permeability for the BCC layer is estimated from consolidation tests performed by Woodward-Clyde (1982). Coefficient of permeability values for the other strata are estimated based on the USCS classification using the correlations presented by Holtz and Kovacs (1981). These values are included in Tables 2 and 3.

2.5.1 Calibration of PM4Silt

PM4Silt is an effective stress-based bounding surface plasticity model formulated to model the dynamic behavior of low plasticity silts and clays (Boulanger and Ziotopoulou 2018). The model utilizes the same general framework as the PM4Sand constitutive model, but the formulation is modified to better represent undrained behavior of silts and clays instead of cohesionless granular soils. The model is limited to plane strain applications and cannot represent strength anisotropy. PM4Silt is not recommended for applications involving consolidation processes as the model does not include a cap on the yield surface. More detailed information on the model formulation and implementation is available in Boulanger and Ziotopoulou (2018).

Calibration of the PM4Silt constitutive model is performed using the single element DSS drivers as recommended by Boulanger and Ziotopoulou (2018). Strain controlled undrained monotonic DSS drivers are used to calibrate peak and residual strengths and softening rates for the BCC. Strain controlled undrained cyclic DSS drivers are used to calibrate for shear modulus reduction and equivalent damping ratio behavior using the relationships presented by Vucetic and Dobry (1991). Stress ratio (shear stress normalized by vertical effective stress) controlled undrained cyclic DSS drivers are used to calibrate the stiff clay and interbedded layers to target cyclic stress ratios required to cause 3% strain in 30 uniform loading cycles, as recommended by Boulanger and Ziotopoulou (2018).

Calibration of the model is performed individually for the BCC, the stiff clay and the interbedded layers. Five input parameters are modified during the calibration process: undrained shear strength ratio at critical state ($S_{u,cs,eq}/\sigma'_v$), shear modulus coefficient (G_o), contraction rate parameter (h_{po}), and the internal parameters h_o and $n^{b,wet}$. The first two parameters are set based on the soil properties summarized in the previous section, while the last three parameters are calibrated using the single element DSS drivers. Further details regarding the PM4Silt input parameters used in this study are outlined in Boulanger and Ziotopoulou (2018). The values of these parameters for the three fine grained layers are summarized in Table 2-2 and the calibration process for the individual layers is described in the following paragraphs.

Table 2- 2: Selected PM4Silt input parameters for the Bootlegger Cove Clay (BCC), interbedded and stiff clay layers

	Softening Rate	$S_{u,pk}/\sigma'v$	$(S_{u,cs,eq}/\sigma'_v)$	h_{po}	$n^{b,wet}$	h_o	G_o	k (cm/s)
BCC	Fast	0.23	0.045	15	0.225	0.3	420	3.0E-08
	Fast	0.26	0.045	15	0.165	0.3	420	3.0E-08
	Fast	0.30	0.045	15	0.050	0.3	420	3.0E-08
	Slow	0.23	0.045	45	0.231	0.3	420	3.0E-08
	Fast	0.23	0.075	15	0.305	0.3	420	3.0E-08
Interbedded	N/A	0.35	0.34	2	0.8	1.7	1303	1.0E-06
Stiff Clay	N/A	0.35	0.34	2.5	0.8	1.6	1211	5.0E-08

The calibration for the BCC is performed for two values of $S_{u,res}/\sigma'_v$ (0.075 and 0.045) and two rates of softening (slow and fast). These different calibrations are used to examine the effects of variations in model parameters on the simulation results. G_o is set to achieve the desired shear wave velocity (220 m/s) at a depth of 25m using the mean stress from the static equilibrium phase of the numerical simulations at this depth away from the slope (approximately zero shear stress) to be consistent with the location where the measurements were taken (Nath et al. 1997). The desired $S_{u,res}/\sigma'_v$ is specified using the parameter $S_{u,cs,eq}/\sigma'_v$ and the peak strength is set by iteratively adjusting the $n^{b,wet}$ parameter until the desired peak strength is achieved in a strain controlled undrained monotonic DSS driver. The parameter h_{po} is adjusted to modify the rate of softening. Calibrations are performed, such that the shear strength ratio (shear stress normalized by vertical effective stress) in the undrained monotonic DSS driver converges to the residual value in approximately 10% (fast) and 20% (slow) total shear strain (Figure 2-5). The parameter h_o is set to produce shear modulus reduction and equivalent damping ratio curves that are consistent with those suggested by Vucetic and Dobry (1991) for clays with a plasticity index (PI) near 15 which is roughly the average PI for the BCC (Shannon and Wilson 1964) in a strain controlled undrained cyclic DSS driver. A stress ratio controlled undrained DSS driver is then used to check the cyclic stress ratio required to cause 3% strain in the BCC in 30 cycles. Example results from the monotonic undrained DSS simulations are shown in Figure 2-5 and results from stress ratio controlled undrained cyclic DSS simulation are shown in Figure 2-6. These results are consistent with those observed from cyclic tests on clayey soils (e.g., Boulanger and Idriss 2007, Price et al. 2015).

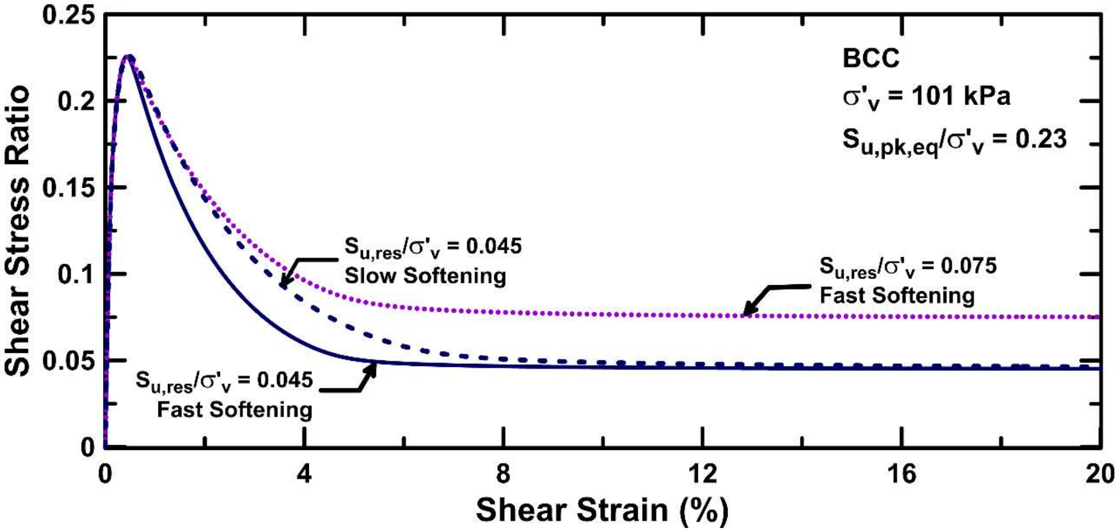

Figure 2- 5: Strain controlled undrained monotonic direct simple shear (DSS) simulations using PM4Silt and different residual strength ratios ($S_{u,res}/\sigma'_v$) and softening rates

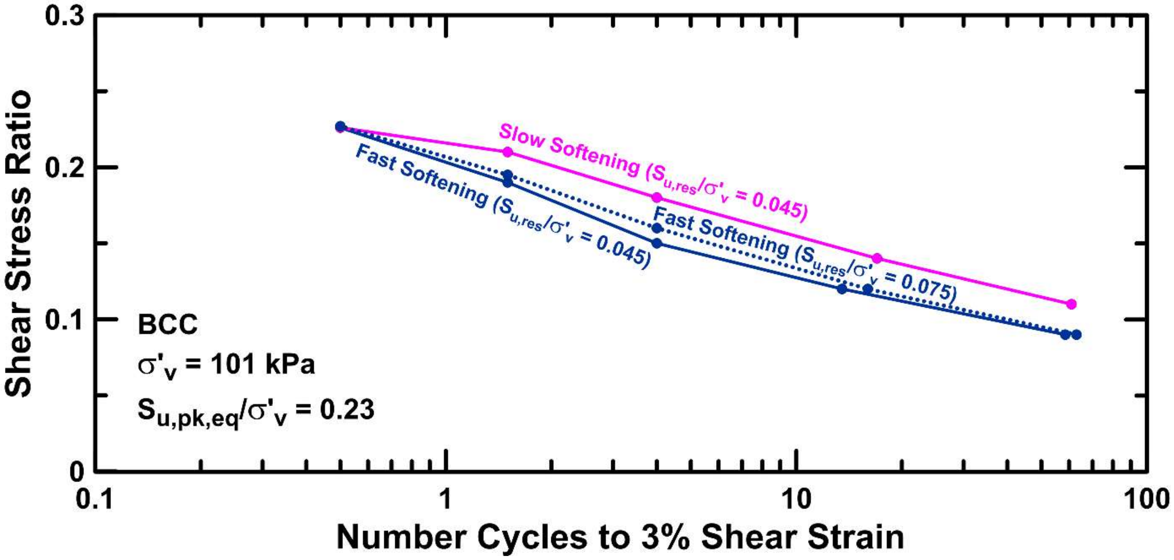

Figure 2- 6: Stress ratio controlled undrained cyclic direct simple shear simulation results using PM4Silt and different residual strength ratios ($S_{u,res}/\sigma'_v$) and softening rates

The calibration of the softening behavior in PM4Silt is independent of the size of the mesh when considered in terms of strain, but the mesh size does become important when estimating the amount of displacement needed to reach this level of strain. Lateral ground displacements at Fourth Avenue were typically observed to be less than 15 cm or greater than 3 m (Woodward-Clyde 1982). This observation has led previous researchers to use 15 cm of lateral displacement as a threshold for the occurrence of strength loss in the BCC (e.g., Woodward-Clyde 1982, Idriss 1985). This value is slightly larger than the upper end of the constant volume ring shear data presented by Stark and Contreras (1998), but they note that 15 cm would be a reasonable value to use for design. The baseline simulations use BCC elements that are approximately 1.3 m tall, so the fast softening rate would be expected to cause full softening after 13 cm of lateral displacement in a simple shear mode of deformation. Simulations using the slower softening rate would require approximately 26 cm of lateral displacement to fully soften for the same size mesh of 1.3 m. Simulations using a coarser mesh with 2.6 m tall BCC elements would also require 26 cm of lateral displacement to fully soften using the fast softening rate. This is one way that strain-softening can lead to a mesh dependent solution unless a regularization scheme is implemented into the constitutive model. This form of mesh dependency can be reduced by introducing a length scale into the calibration approach, so that the calibrations give consistent results in terms of displacements for different mesh sizes. This approach will be discussed later.

Calibration of the stiff clay layer and the interbedded zone are performed in a similar manner to the BCC layer, except $n^{b,wet}$ is assigned a value of 0.8 for both layers, as recommended by Boulanger and Ziotopoulou (2018) for their default calibration. G_o is set to achieve the desired shear wave velocity (300 m/s for the interbedded zone and 450 m/s for the stiff clay) at the appropriate depths for each layer. This is done using the mean stress from the static equilibrium phase of the numerical simulations at the corresponding depth away from the slope (approximately zero shear stress) to be consistent with the location where the measurements were taken (Nath et al. 1997). Undrained shear strength ratios are specified using the parameter $S_{u,cs,eq}/\sigma'_v$ and these layers are assumed not to have any significant sensitivity. The parameter h_{po} is then calibrated using stress ratio controlled undrained cyclic DSS simulations, so that the cyclic stress ratio required to cause 3% strain in 30 uniform loading cycles is about 60% of $S_{u,cs,eq}/\sigma'_v$ based on the recommendations of Boulanger and Ziotopoulou (2018). The parameter h_o is set to produce shear modulus reduction and equivalent damping ratio curves using undrained strain controlled cyclic DSS drivers that are consistent with those suggested by Vucetic and Dobry (1991) for clays with a PI near 15, which is roughly the average PI for these layers (Shannon and Wilson 1964). All other model parameters are assigned default values (Boulanger and Ziotopoulou 2018).

2.5.2 Calibration of PM4Sand

PM4Sand is an effective stress-based, bounding surface plasticity model often used to simulate cyclic liquefaction in granular soils. The model follows the basic framework of the stress-ratio controlled, critical state compatible, bounding surface plasticity model for sand originally described by Manzari and Dafalias (1997) and Dafalias and Manzari (2004). The model is modified and calibrated to approximate engineering design relationship used for evaluating liquefaction of sandy soils. More detailed information on the formulation and implementation of PM4Sand can be found in Boulanger and Ziotopoulou (2017).

The outwash and sand layers are modeled using PM4Sand version 3.1 (Boulanger and Ziotopoulou 2017). The model requires three main input parameters: relative density (D_R), G_o and h_{po}. The last two parameters have the same definition as given above for PM4Silt. G_o is set to achieve the desired shear wave velocity for these layers (300 m/s). Average $(N_1)_{60}$ values of about 45 and 50 are selected for the outwash and sand layers based on the SPT tests performed by Shannon and Wilson (1964). Relative densities are then estimated for use in the PM4Sand model according to Equation 2-3.

$$D_R = \sqrt{\frac{(N_1)_{60}}{46}} \tag{2-3}$$

The parameter h_{po} is set using an undrained cyclic DSS driver and adjusting the value of h_{po} to achieve the desired cyclic resistance ratio (CRR). For this study, the CRR to cause 3% shear strain in 15 loading cycles is set at 0.8. This CRR value is selected in order to give these layers a high cyclic strength which is consistent with the high $(N_1)_{60}$ values and lack of surface manifestations of liquefaction at this site. The input parameters for these layers are shown in Table

2-3. All other input parameters are assumed to be equal to the default values for the model (Boulanger and Ziotopoulou 2017).

Table 2-1: Selected PM4Sand input parameters for Outwash and Sand Layers

	Outwash	Sand
$(N_1)_{60}$	45	50
h_{po}	0.012	0.034
G_o	2000	1177
k (cm/s)	1.0E-03	1.0E-03

2.6 SIMULATION RESULTS

The simulation approach described above is used to analyze the response of the Fourth Avenue site. A baseline analysis is performed first, followed by a limited sensitivity study to examine the effects of the BCC properties and the input motion on the results. The initial (pre-shaking) vertical effective stress distribution within the model and the static shear stress ratio distribution are shown in Figure 2-7 (compressive stresses are negative). The initial static shear ratios are about 0.10-0.20 beneath the slopes and are close to zero outside of the slide mass. Boulanger and Idriss (2004) report static shear stress ratios of 0.10 beneath the slopes and 0.01 outside the slide mass, which is consistent with the simulation results. The static stress distribution is identical for all of the simulations.

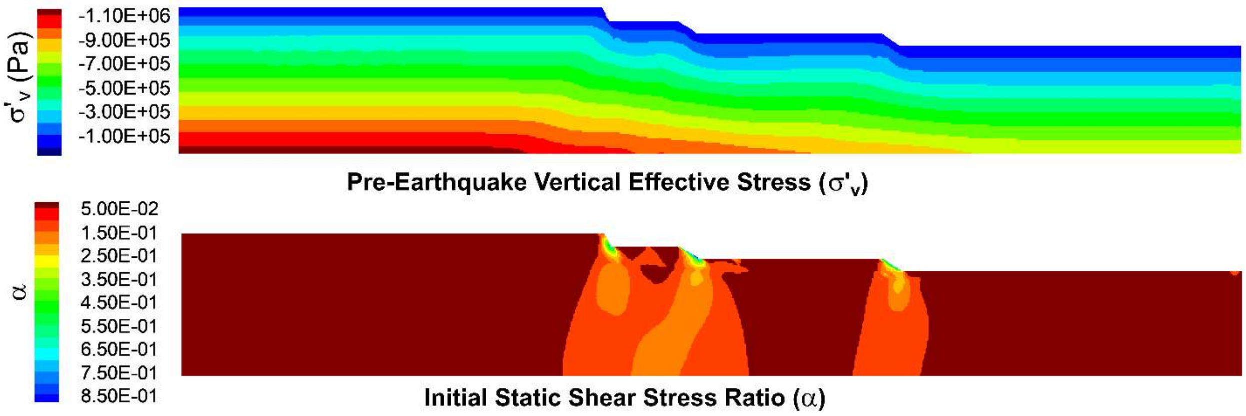

Figure 2- 7: Initial (pre-earthquake) vertical effective stress (top) and initial (pre-earthquake) static shear stress ratio (bottom) profiles for the Fourth Avenue landslide

2.6.1 Baseline Analysis

The baseline analyses are performed using the HUA-T input motion (Table 1), the faster softening rate (Figure 2-5) and the two $S_{u,res}/\sigma'_v$ values. Figure 2-8 shows contours of lateral displacement for both $S_{u,res}/\sigma'_v$ values with the BCC layer outlined in light grey. Both simulations show a predominantly translational failure mechanism occurs within the slope. This is consistent with the deformation patterns observed at the site except that no clear graben is observed in the simulations. Deformations are concentrated in the BCC layer beneath the lower slopes and propagate up to the bluff behind the upper crest of the slope. The lower $S_{u,res}/\sigma'_v$ value results in an upper crest displacement of about 1.0 meters, which is much smaller than is observed in the field. For the higher sensitivity, the upper crest displacements reach approximately 4.7 meters before the simulation is halted due to excessive mesh distortion.

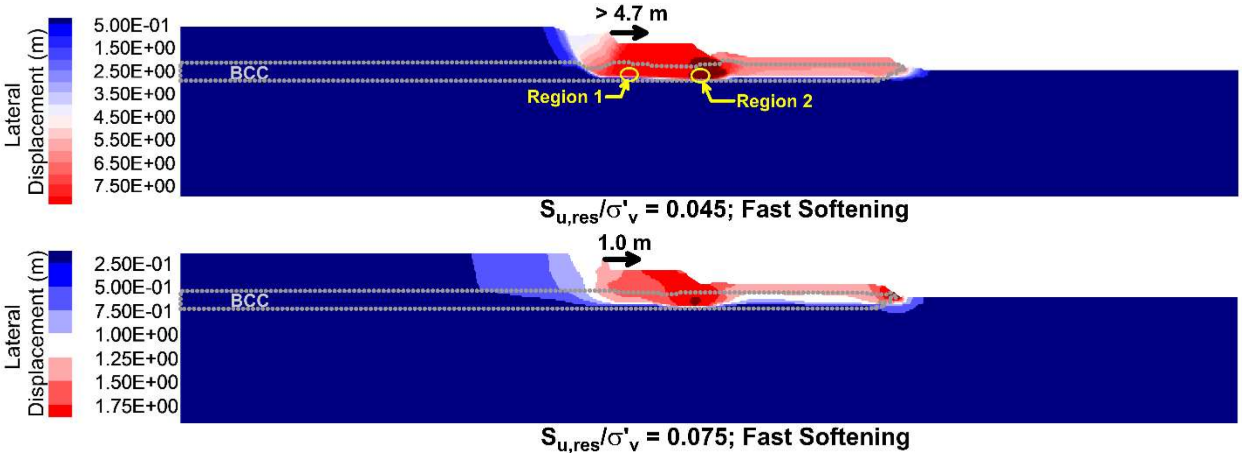

Figure 2- 8: Contours of horizontal displacements (m) for simulations using a residual strength ratio ($S_{u,res}/\sigma'_v$) of 0.045 (top) and 0.075 (bottom) with BCC layer outlined in light grey

Time histories of lateral crest displacement for both $S_{u,res}/\sigma'_v$ values are shown in Figure 2-9a. Figure 2-9b shows excess pore pressure ratio time histories for two regions with different initial stress states (labeled Region 1 and Region 2 in Figure 2-8) along the horizontal portion of the failure plane. Time histories of excess pore pressure ratio are recorded for elements both inside and outside the failure plane in each region. Figure 2-9c shows the input acceleration for the baseline motion. Significant movement begins approximately at the onset of strong shaking at which point the BCC begins to soften, as indicated by the increase in excess pore pressure. After about 15 seconds of strong shaking, the residual shear strength along the failure plane is reached and deformation magnitudes begin increasing more rapidly. For the higher $S_{u,res}/\sigma'_v$, the deformations build at a gradual rate before stabilizing near the end of strong shaking. For the lower $S_{u,res}/\sigma'_v$, the deformations increase significantly after softening begins and the displacements are still slightly increasing when the simulation is stopped due to excessive mesh distortion. Figure 2-9b shows significant pore pressure generation for elements inside the failure plane and comparatively little pore pressure generation for elements outside the failure plane. Gylland et al. (2014) suggest that strain-softening in sensitive clays is primarily a result of pore pressure generation due to contractive behavior at failure. Viggiani et al. (1994) observed that strain localization caused significant pore pressure generation near observed shear bands with pore pressure generation decreasing with distance away from the shear band in globally undrained plane strain compression tests on a stiff clay. These previous findings are consistent with the results of the current simulations.

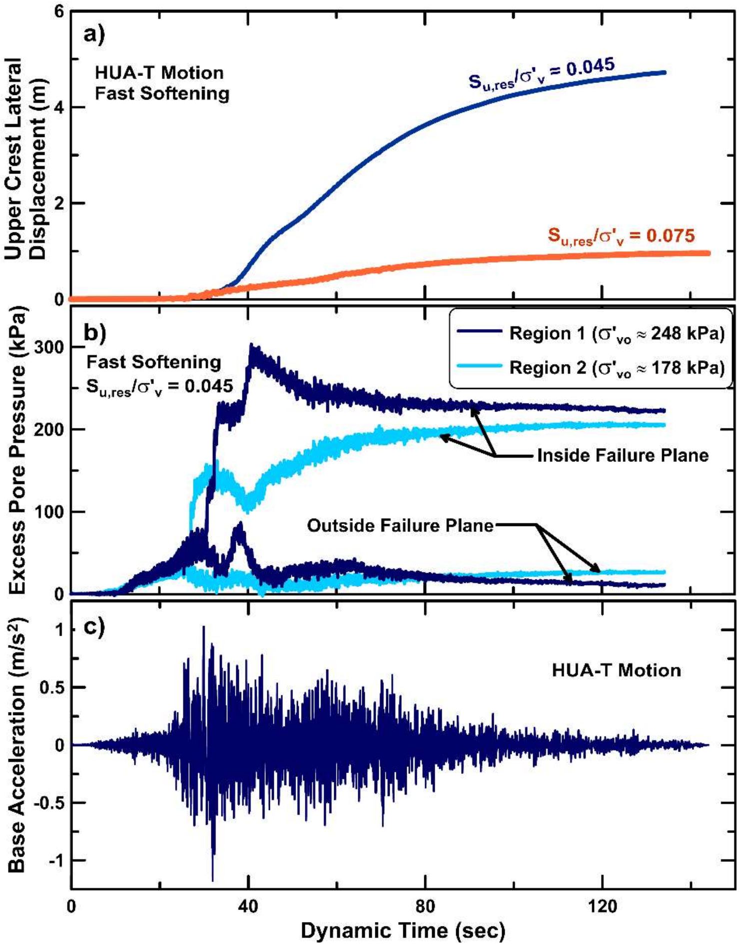

Figure 2- 9: Time histories of (a) upper crest lateral displacement for residual strength ratios ($S_{u,res}/\sigma'_v$) of 0.045 and 0.075 using the HUA-T input motion, (b) excess pore pressure ratio in Regions 1 and 2 (see Figure 3-5) for HUA-T input motion with $S_{u,res}/\sigma'_v = 0.045$ and fast softening and (c) base (input) accelerations for HUA-T input motion

Figure 2-10 shows the stress paths and shear stress versus strain plots for elements inside the failure plane in Regions 1 and 2 (Figure 2-8) for the baseline motion with the lower $S_{u,res}/\sigma'_v$

and fast softening. Figure 2-10a shows that elements in Regions 1 and 2 have similar initial horizontal shear stresses but the element in Region 1 has a higher initial vertical effective stress. This higher initial vertical effective stress leads to higher peak and residual strengths (Figure 2-10b). Residual strengths in both elements are achieved by about 10% shear strain, which is consistent with the calibration (Figure 2-5).

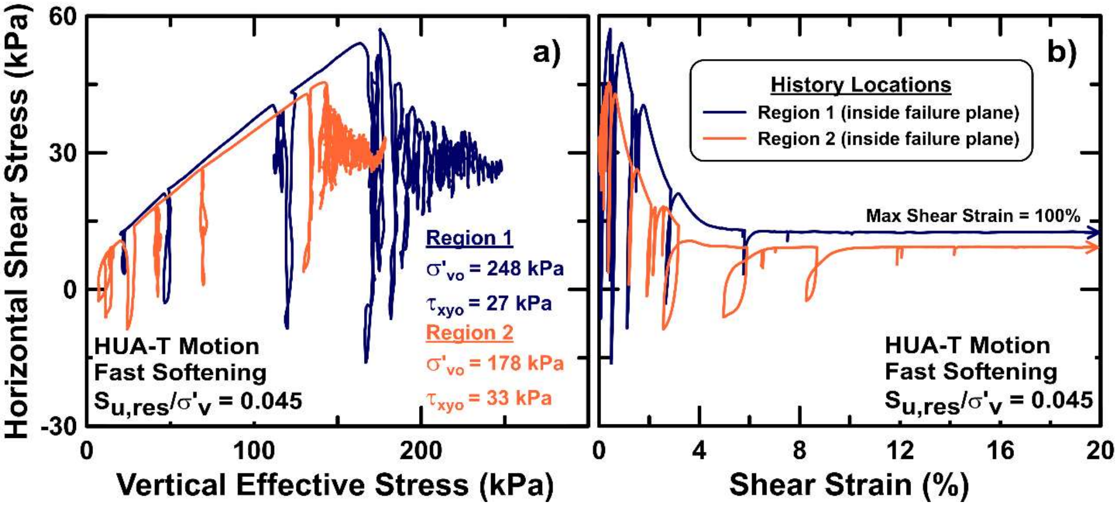

Figure 2- 10: Responses of two elements located on horizontal portion of failure plane with different initial static vertical effective (σ'_{vo}) and horizontal shear stresses (τ_{xyo}): (a) horizontal shear stress versus vertical effective stress; (b) horizontal shear stress versus shear strain

The simulation results show that most of the deformation occurs after the BCC has fully softened. This would imply that the residual strength is a more important factor than the small-strain behavior of the model for this case history, assuming the loading is large enough to fully soften the soil. Some insight into the role of small strain behavior can be found by comparing the baseline simulation results to those from Kiernan (2019) and Beaty and Dickenson (2015). Kiernan (2019) analyzed the Fourth Avenue slide using a strain-softening Mohr-Coulomb model with 1.8 m tall BCC elements and found that a BCC sensitivity of 7 (for $S_{u,pk}/\sigma'_v = 0.23$) softening in 7% element strain (12.6 cm displacement to fully soften) is required to produce displacements consistent with site observations. Beaty and Dickenson (2015) used a hysteretic model called Hyper-U, which is a nonlinear stress strain model that simulates the effects of pore pressure generation, softening due to reduction in effective stress, and strength loss with accumulated strain. Their simulations are able to produce results consistent with the observations when using element heights of 0.66 m, a BCC sensitivity of 4 and full softening in 10% strain (6.6 cm displacement to fully soften). These results are consistent with the simulations from this study. The current study and Beaty and Dickenson (2015) both used models that are able to reasonably approximate cyclic degradation of the BCC before full softening, while the Mohr-Coulomb model used by Kiernan (2019) was linear elastic before yielding. The Mohr-Coulomb model would have significantly dampened the propagating seismic waves after yielding, which likely reduced the loading on the slope. Thus, higher sensitivities are required to achieve the same final displacement. Additional studies are needed to directly compare the results using different constitutive models and identify the effects of differences in the constitutive behaviors on the final displacement and other response measures, such as surface accelerations and pore pressure generation. This is an important area for future research and is explored in the next chapter.

2.6.2 Effect of Input Motion

The effect of ground motion variability is investigated by running each of the simulations described above with the suite of selected input motions (Table 2-1). Time histories of lateral crest displacement for each of the input motions are shown in Figure 2-11a for a $S_{u,res}/\sigma'_v$ value of 0.045 and Figure 2-11b for a $S_{u,res}/\sigma'_v$ value of 0.075. For each individual motion, displacement magnitudes increase with decreasing $S_{u,res}/\sigma'_v$, as expected. For a given a $S_{u,res}/\sigma'_v$, the motions producing the largest displacements also have the largest Arias Intensities (Table 2-1). This is consistent with the observations of Travasarou et al. (2003) that seismic slope displacements are better correlated with Arias Intensity than amplitude-based parameters, such as peak ground acceleration or peak ground velocity, as it combines both the effects of duration and amplitude. Eleven of the twelve input motions result in displacements greater than 3 meters when a $S_{u,res}/\sigma'_v$ value of 0.045 is used. Displacements for these eleven simulations are also still increasing (Figure 2-11a) when the simulations are halted due to excessive mesh distortion.

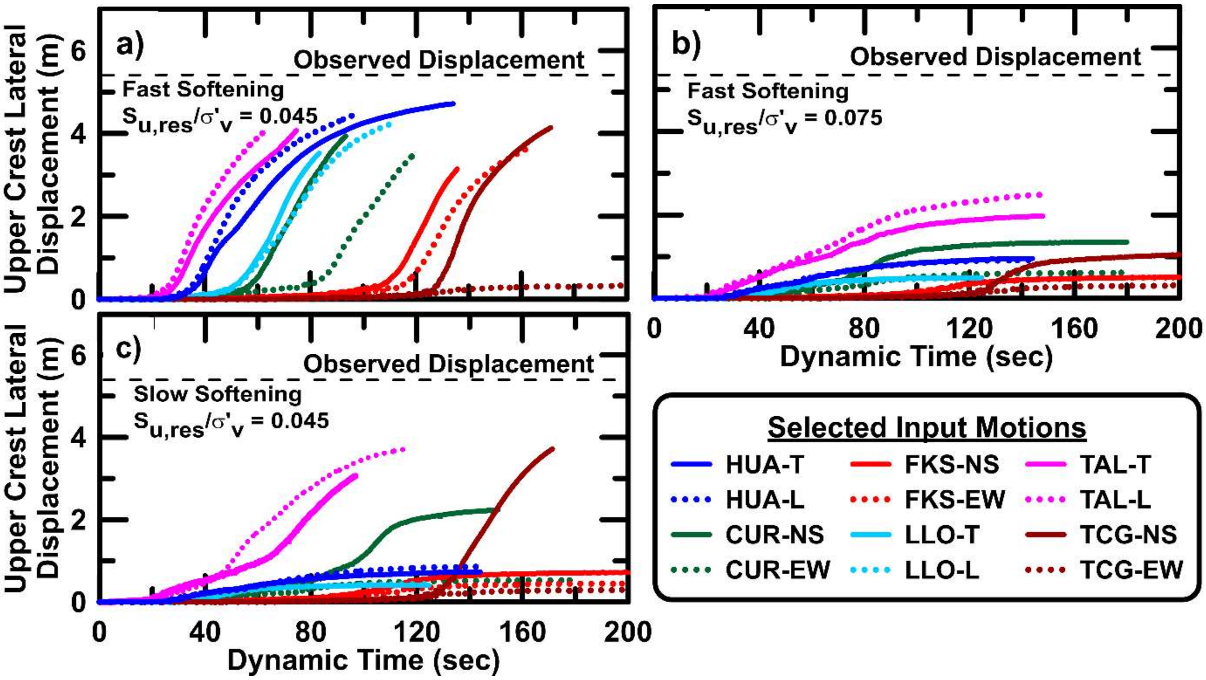

Figure 2- 11: Time histories of upper crest lateral displacement for fast softening with residual strength ratio ($S_{u,res}/\sigma'_v$) of (a) 0.045, (b) 0.075, and (c) slow softening with a $S_{u,res}/\sigma'_v$ of 0.045

For the higher $S_{u,res}/\sigma'_v$, all of the simulations are stable by the end of shaking and no simulations are halted due to mesh distortion (Figure 11b). The most intense motion in terms of Arias Intensity (TAL-L), results in the largest observed displacement (2.5 meters), but most of the motions produce displacements closer to 1 meter. The lateral displacements for simulations using both $S_{u,res}/\sigma'_v$ values begin to increase at approximately the same time for the respective input motions (comparing Figure 11a and 11b), which is expected as all analyses utilize the same BCC peak strength. After softening begins, results from the $S_{u,res}/\sigma'_v$ values begin to diverge as the lower residual strength in the simulations results in much larger displacements.

2.6.3 Effect of BCC Softening Rate

The effect of BCC softening rate is analyzed by repeating the simulations described above with the properties for the slow rate of softening and a $S_{u,res}/\sigma'_v$ value of 0.045 (Table 2-2). The effect of reducing the BCC softening rate can be seen by comparing Figures 2-11a and 2-11c. The simulations with the slower softening rate show larger displacement rates beginning later in the simulation, which is expected since more displacement is necessary to fully soften the BCC layer with the slower softening rate. For approximately half of the motions, the BCC layer does not reach the residual strength with the slower softening rate resulting in relatively small final displacements. The faster softening rate is more consistent with the analyses performed by Idriss (1985) and Beaty and Dickenson (2015), but there is considerable uncertainty in how to select this value. These results demonstrate the solution is sensitive to the selected softening rate. Future analyses using this modeling approach should carefully consider how this value is selected and perform sensitivity analyses to understand how the results may depend on variations in the selected value.

2.6.4 Effect of BCC Peak Undrained Shear Strength

The peak undrained shear strength of the BCC may be affected by variations in OCR or strain rate effects during earthquake loading, as previously discussed. The effects of the peak undrained shear strength in the BCC are investigated by repeating the baseline simulations with $S_{u,pk,eq}/\sigma'_v$ values of 0.26 and 0.30, which correspond to increases over the baseline value of about 115% and 130%, respectively. All of the simulations used the same residual strength ($S_{u,res}/\sigma'_v$ =

0.045). Time histories of upper crest lateral displacement for the different $S_{u,pk,eq}/\sigma'_v$ values are shown Figure 2-12. The simulations with the larger peak strength show larger displacement rates beginning later in the simulation, as it takes slightly more displacement to reach the peak strength and initiate softening. The behavior is similar in all three simulations once larger displacement rates begin, although the final displacement value decreases with increasing peak strength.

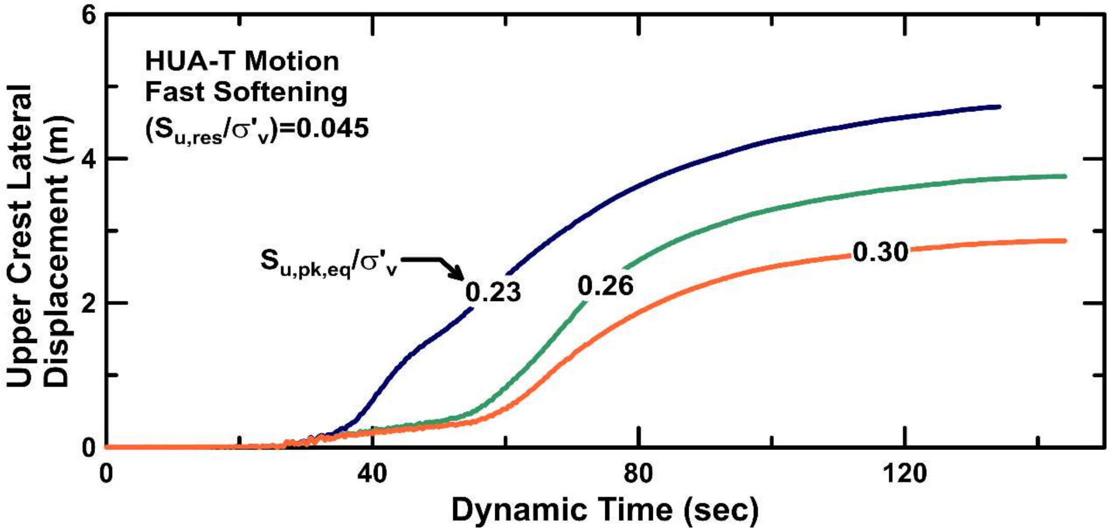

Figure 2- 12: Time histories of upper crest lateral displacement with varying values of peak undrained shear strength ratio and a $S_{u,res}/\sigma'_v$ of 0.045

These results show that although the final value of displacement is sensitive to the peak strength, the development of large deformations occurred in each simulation. This is expected because all simulations used the same residual strength. Uncertainty in the true peak strength comes from the scatter in the laboratory data (Figure 2-3) and selection of an appropriate factor to account for strain rate effects. The three values considered here are meant to represent a reasonable range for both factors. The baseline simulations use a peak strength which is likely on the lower side of the reasonable range, but the results in Figure 2-12 show that the overall conclusions would likely be similar had a higher peak strength been selected. This provides further evidence that the residual strength and the softening rate are the two controlling parameters for these simulations.

Additional work is needed to examine the possible effects of spatial variability in the undrained shear strength on the results.

2.6.5 Effect of Mesh Density

The effects of mesh density are examined by repeating the baseline simulations using a finer and a coarser mesh. This is done to examine whether the solution shows any dependency on the mesh size. For the baseline simulations, the mesh uses 14,602 elements with an average height of 1.3 m in the BCC layer. The calibration is also performed for 1.3 m elements to ensure consistent results between the calibration and simulation. For the coarse mesh, the number of elements is decreased by 50%, resulting in an average element height in the BCC of 1.8 m. For the fine mesh, the number of elements is increased by 50% relative to the baseline and the average element height in the BCC is 0.9 m. The softening rate is initially kept the same for all three simulations to examine the effects of using a different mesh size for simulations than is used for model calibration.

Relatively little mesh dependency is observed for the simulations with the higher $S_{u,res}/\sigma'_v$ value (Figure 2-13a). For each of the mesh sizes, displacements begin at approximately the same time and increase at similar rates. The fine mesh shows the largest displacements due to shear strains accumulating more rapidly in the smaller elements. This occurs because deformations tend to localize in a single row of elements and for a given amount of lateral displacement, the shear strain at the element level will become larger as the size of the elements decrease. Larger shear strains will lead to faster softening and larger displacements. This pattern is also observed for the lower $S_{u,res}/\sigma'_v$ value (Figure 2-13b), but the differences between the simulations are more significant. For the lower $S_{u,res}/\sigma'_v$, the coarse mesh stabilizes at a final displacement of approximately 3.6 m, while the other two simulations are halted due to excessive mesh distortion.

Despite these simulations being halted, it is clear that the final displacements would have been much larger than observed for the coarse mesh.

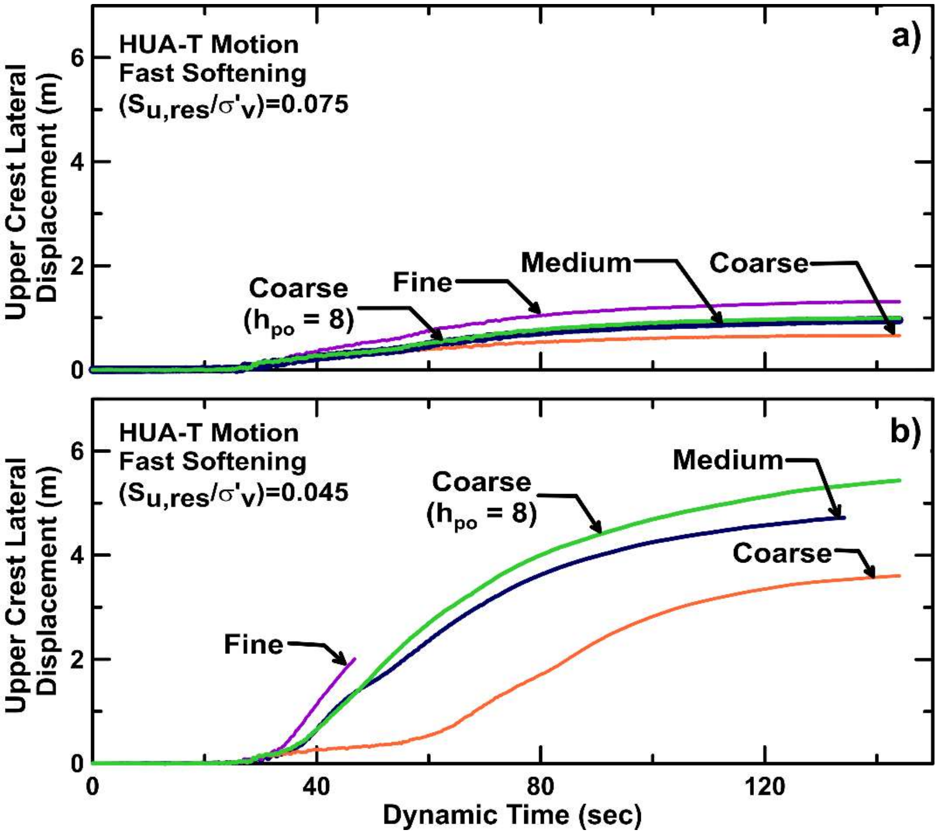

Figure 2- 13: Time histories of upper crest lateral displacement for varying mesh densities and residual strength ratios ($S_{u,res}/\sigma'_v$) of (a) 0.045 and (b) 0.075. The results for the recalibrated coarse mesh are shown for comparison

Mesh dependence is just one important factor that may affect numerical solutions, but it is one factor that is often ignored in studies using NDAs. Previous studies have found that including pore fluid coupling can reduce mesh dependence when elements are used that are similar in size to the thickness of the shear band (e.g., Thakur 2006, Gylland et al. 2014). This regularization of the solution occurs because incorporating fluid coupling (and corresponding flow) introduces a length scale into the problem through the gradient term in Darcy's Law (Thakur 2006). The elements inside the shear band will generate large excess pore pressures, while the elements outside will not, which creates a large gradient over the thickness of the shear band, which is on the order of millimeters. In the current simulations, pore fluid coupling has been included (e.g., Figures 2-9b and 2-10), but the solution still demonstrates mesh dependency. This is because the elements in the current simulation are too large to capture the high gradients within a small shear band that would be needed to regularize the solution.

A length scale can be introduced into the current model by considering the combined effects of mesh size and softening rate, as both affect the amount of softening that will occur within a given element. For example, increasing the mesh size results in smaller strains at the element level for a given amount of displacement. This leads to slower rates of softening in the model, which may be sufficient to prevent large displacements from occurring depending on the magnitude of the loading (e.g., Figure 2-13b). To test this, the model is recalibrated to increase the rate of softening in the coarse mesh by adjusting the h_{po} parameter to 8.0. This causes the single element simulations to reach the residual strength in approximately 7% shear strain, as opposed to 10% shear strain for the original calibration. Using the coarse mesh size (1.8 m), 7% shear strain would be reached after 13 cm of lateral displacement, which is the same displacement needed to fully soften the medium mesh (1.3 m elements) using the fast softening rate (10% strain). The results from the coarse mesh with the recalibrated softening rate are also shown in Figure 2-13. The recalibrated coarse mesh simulations show significantly more displacement than the original coarse mesh simulation for the lower $S_{u,res}/\sigma'_v$ (Figure 2-13b) and similar displacements for the higher $S_{u,res}/\sigma'_v$ (Figure 2-13a). The results using the recalibrated coarse mesh are similar to those using the medium mesh with the original calibration, as both of these simulations soften in approximately the same displacement at the element level.

Revising the calibration procedure to ensure a consistent level of displacement to cause softening allows simulations with different mesh sizes to produce similar displacement results, but does not fully address the issue of mesh dependency. For this case history, the displacement to cause softening (~15 cm) had been estimated by Idriss (1985) based on regional displacement measurements and by Stark and Contreras (1998) using ring shear data, but reliable methods to select this value for forward analyses still need to be developed. This approach would also require the user to perform a separate calibration for each mesh size, which may not be possible for irregular meshes. Implementation of a regularization scheme into PM4Silt would allow the dependency of the solution on mesh size to be reduced without this additional calibration step and this remains an important task for future researchers (e.g., Oathes and Boulanger 2020). The goal of the current analyses is to make future users aware of this potential mesh dependency and highlight the importance of considering this source of uncertainty in their analyses. It is important to emphasize that mesh dependence is just one source of uncertainty in these analyses and the magnitude of this uncertainty for the current study is less than the uncertainty due to the residual strength, softening rate, or input motion.

2.7 DISCUSSION

The simulation results show that PM4Silt is able to produce deformations consistent with those observed at the Fourth Avenue site when using a $S_{u,res}/\sigma'_v$ value of 0.045 and the faster rate of softening. These values are consistent with previous studies (e.g., Beaty and Dickenson 2015, Kiernan 2019). With this combination of parameters, almost all of the selected input motions produced large displacements with the simulations halting after about 3 to 5 meters of upper crest translation due to excessive mesh distortion. Displacements are still increasing at this point and would likely have reached final values that would have been consistent with the observed displacements. Increasing the $S_{u,res}/\sigma'_v$ or decreasing the rate of softening reduces the displacements significantly for most of the input motions, although the deformation patterns within the slope are similar. The peak strength also influenced the final displacement values. This demonstrates the importance in carefully selecting material properties and performing sensitivity studies to understand how the results may change given reasonable ranges in critical parameters.

One of the critical parameters in the current simulations is the softening rate. For the current study, the softening rate is calibrated to be consistent with previous authors' estimates for this case history (Idriss 1985, Stark and Contreras 1998, Beaty and Dickenson 2015). In practice, selecting the rate of softening for a given soil can be difficult. Laboratory tests, such as ring shear or triaxial tests, can be used to examine strain-softening behavior, but these results may not accurately represent the post-peak softening behavior of the soil at the field scale (Potts et al. 1990, Andresen and Jostad 1998). Additional work is needed to more accurately define the relationship between laboratory- and field-scale softening behavior and provide guidance for selecting parameters to describe softening rate for future studies. It should also be noted that the procedure recommended herein produces a relatively brittle stress-strain curve with peak strengths being reached after 0.5-1.0% strain. This calibration procedure may not be appropriate for soils with more ductile stress-strain responses.

A limited sensitivity study is performed to examine the effects of softening rate, peak strength, residual strength, input motion and mesh size on the simulation results. These are not the only simulation parameters that are likely to influence the results and additional sensitivity studies are warranted to better understand how each of the model parameters affects the final solution. Additional items that could be investigated in future studies include strength anisotropy, spatial variability in properties, changes in stratigraphy, uncertainty in the properties of the non-BCC layers, changes in the elastic properties and modulus degradation relationships, and the use of alternative constitutive models and/or numerical formulations.

The mesh sensitivity study shows that the final displacement values are affected by changes in the size of the mesh. The simulations with different mesh sizes begin to diverge after softening occurs and deformations begin to localize into a single row of elements. Larger elements will experience less strain for a given magnitude of displacement and therefore softening occurs more slowly in simulations using larger mesh sizes. The effect is most pronounced for simulations with higher sensitivities. Mesh dependent solutions are a common limitation of strain-softening models (Brinkgreve 1994) and many regularization schemes have been developed (Pietruszczak and Mróz 1981, Brinkgreve 1994, Jostad and Andersen 2004, Thakur et al. 2005, Park 2011) to address this dependency. Previous research has suggested that pore fluid coupling may help to reduce mesh dependency, but the current simulations still exhibited some mesh dependency despite including fluid-mechanical coupling. Thakur et al. (2006) suggest that rate dependence incorporated together with pore fluid coupling may be required to reduce mesh dependency. Jostad et al. (2006) found rate dependence together with pore fluid coupling to be successful at reducing mesh dependency, but only when elements sizes smaller than the shear band thickness are used. The use of such small elements is impractical for use in full-scale models as they increase computational time and are prone to geometry errors during large deformations, which halt simulations early producing incomplete results.

The simulations presented in this chapter have utilized a continuum, finite difference program with a Lagrangian formulation, which is commonly used in geotechnical practice, but is limited in its ability to simulate large deformations. Recently, alternative simulation techniques have been used in analyses of landslides to overcome some of these limitations. These techniques include mixed Langrangian-Eulerian approaches (e.g., Moug et al. 2019), interface elements (e.g., Jostad and Andersen 2004) and material point methods (e.g., Soga et al. 2016). A detailed description of each of these techniques, including advantages and disadvantages, is provided by Soga et al. (2016). These techniques would be able to overcome the problems of excessive mesh distortion, which may cause a simulation to halt before the loading is complete. Previous studies using these alternative methods have primarily focused on static problems and/or relatively simple elastoplastic constitutive models. Additional work is needed to develop and validate these approaches for simulations involving fluid coupling and seismic loading. The results in this study can serve as a comparison for these future studies.

2.8 CONCLUSIONS

The response of the Fourth Avenue landslide is investigated using the PM4Silt constitutive model (Boulanger and Ziotopoulou 2018). The model is calibrated to represent the mildly sensitive BCC layer using two residual strength ratios and two rates of softening. The simulation results are generally consistent with the observed deformations when using peak and residual strengths that are slightly below the average values from laboratory tests (Figure 2-3), but well within the scatter of the data. These results provide additional confidence to future users that the PM4Silt model can represent the cyclic softening behavior of mildly sensitive clays, although additional validation studies are needed to confirm this for a wider range of problem geometries, soil properties and ground motions.

A limited sensitivity study is performed to investigate the effects of changing the strength of the BCC, the rate of softening, the input motion and the mesh size on the final displacements. The results follow expected trends, with higher displacements occurring for lower peak and residual strengths, faster softening rates, and more intense ground motions. The solution is observed to be mesh dependent with finer meshes tending to show larger displacements. Differences in displacements from simulations using different mesh sizes can be reduced by ensuring the calibrations are performed with the same size elements as will be used in the simulations. This may not be practical in all circumstances (i.e., irregular meshes) and so future users must be aware of the effects of mesh dependence if their simulation has significant softening. Implementation of a regularization technique into PM4Silt would help eliminate this dependence and this remains an important topic for future research (e.g., Oathes and Boulanger 2020). The sensitivity results indicate the importance of careful calibration protocols and proper documentation to ensure future users understand the choices made during calibration and how they may affect the simulation results.

The findings presented herein are limited to the range of properties and loading conditions examined in the simulations. PM4Silt is shown to be able to capture the cyclic softening of the BCC, but it should be noted that the model is limited to plane strain applications and cannot represent strength anisotropy. The user must therefore select appropriate strength values for calibration. The model also does not have a cap on the yield surface and so is unable to model consolidation, including any post-earthquake reconsolidation that may have occurred at this site. Other factors that may warrant further examination in the future are variability in properties, potential for softening in the non-BCC layers, three-dimensional effects, and loading rate effects.

CHAPTER 3: COMPARISON OF TOTAL AND EFFECTIVE STRESS-BASED CONSTITUTIVE MODELS REGARDING STRAIN-SOFTENING OF FINE GRAINED SOILS

This chapter is based on a paper that is planned to be submitted by Michael Kiernan and Jack Montgomery to the journal *Landslides.*

Kiernan, M. and Mongomery, J. (2021). “Comparison of Total and Effective Stress-based Constitutive Models Regarding Strain-softening of Fine Grained Soils.” Manuscript under preparation.

This chapter is altered from the version to be submitted to the *Landslides* to minimize repetition and maintain a logical organization of content. My primary contributions to the chapter included: (i) evaluation of available geotechnical testing results, selection of soil parameters and constitutive model calibrations, (ii) literature review, (iii) design and implementation of numerical model, (iv) processing, analyzing, and interpretation of the results, and (v) preparation of initial draft and most of subsequent writing.

3.1 INTRODUCTION

Strain-softening materials are characterized by a post-peak reduction in undrained shear strength which converges toward a residual strength value at large strains. The residual undrained shear strength may be significantly lower than the peak strength and the ratio of the peak to residual undrained shear strength is defined as the sensitivity (S_t). Cyclic softening of fine grained soils due to ground shaking has led to large deformations during previous earthquakes (e.g., Aylsworth and Lawrence 2003) in some cases resulting in substantial infrastructure damage (e.g., Shannon and

Wilson 1964, Fine et al. 2005, Wakai et al. 2014, Tiwari et al. 2018). These failures have illustrated the need to understand the mechanisms governing strain-softening and localization (e.g., Gylland et al. 2014, Park 2011, Thakur et al. 2017), to develop constitutive models to represent this behavior (e.g., Andersen and Jostad 2005, Boulanger and Ziotopoulou 2018), and to develop reliable approaches to estimate earthquake induced ground deformations associated with strength loss in fine grained layers (e.g., Stark et al. 2012, Beaty and Dickenson 2015).

Constitutive models are key to numerical analyses of geomechanical problems as they provide a mathematical representation of material response. The goal of any constitutive model is to represent key aspects of material behavior which are vital to the scenario being modeled (Wood 2014). Key behaviors for modeling cyclic softening of clays include the ability to represent strength loss, volumetric response (i.e., dilatancy), modulus reduction and damping behavior, and the ability to provide a solution that is independent of the chosen element sizes. Constitutive models used to represent strain-softening of fine grained soils typically fall into two categories: total stress-based models (e.g., Stark et al. 2012, Beaty and Dickenson 2015, Kiernan and Montgomery 2018) and effective stress-based models (e.g., Park 2011, Seidalinov and Taiebat 2014, Boulanger and Ziotopoulou 2018). Calibration of total stress-based models is typically straightforward, but these models are often formulated in terms of a simplified stress-strain response (Taiebat et al. 2011) and treat the pore fluid and soil as a single material (Lim et al. 2010). Effective stress-based models are often formulated based on soil mechanics principles (e.g., critical state soil mechanics) that allow for coupling between the pore fluid and solid phases (e.g., Boulanger and Ziotopolou 2018). Critical state models allow the current strength of a soil at given moment to be dependent on the volumetric response. Critical state models are thus constantly chasing a current strength value until ultimately converging towards the critical state strength at very large strain values (Wood 1990). Advanced effective stress-based models can include a relatively large number of input parameters that can be challenging to calibrate using standard lab tests (Lim et al. 2010).

The ability to address strain localization is a limitation common to both total and effective stress-based constitutive models. As the magnitude of shear deformation in a sensitive clay increases, strains will concentrate into thin shear bands accelerating the rate of softening within the localized failure plane (e.g., Park 2011). The formation of shear bands in sensitive clays has been observed in the field (Henkel and Skempton 1955) and in the lab (Gylland et al. 2014). Shear banding has also been observed in centrifuge tests on clay embankments (Kutter and James 1989) and artificially sensitive clay slopes (Park 2011) under static and dynamic loading. The centrifuge tests under static loading generally resulted in the formation of a single critical slip surface, while more diffuse failures were observed in the centrifuge tests under dynamic loading. Even under dynamic loading, the majority of strains ultimately localize on a single critical shear surface as larger deformations occur (Park 2011). The different failure mechanisms observed between static and dynamic loading may be attributed to the counteracting influences of strain rate, which tends to increase the strength of clays, versus strain-softening (Kutter and James 1989, Park 2011). As previously discussed, strains to tend to localize into thin shear bands once softening occurs with thicknesses on the order of micrometers to a few centimeters (Thakur et al. 2006, Gylland et al. 2014, Zabolotnii et al. 2021). However, the peak undrained shear strength of clays increases at faster strain rates (e.g., Lefebvre and LeBoeuf 1987, Lefebvre and Pfendler 1996, Boulanger et al. 1998, Diaz-Rodriguez et al. 2009) which may delay the onset of localization (Park 2011). Multiple shear surfaces may then develop under high dynamic loading rates as the failure surface repeatedly shifts towards weaker planes. The residual undrained shear strength of clays is relatively independent of strain rate (e.g., Biscontin and Pestana 2001, Scaringi and Di Maio 2016) so the majority of shear strain ultimately localizes around one critical failure plane.

In numerical analyses, the minimum thickness of localized failure planes is restricted by the element size. The numerical solution may then be dependent on the chosen element size since larger elements will experience less shear strain compared to smaller elements for a given magnitude of shear displacement. Numerical solutions tend to converge towards a single solution as element sizes are reduced toward the shear band thickness (e.g., Thakur et al. 2006), but the use of such small elements (on the order of a few millimeters) may not be attainable in many field-scale simulations. This is because the use of such small elements in field-scale simulations exponentially increases computation time (Zabolotnii et al. 2021) and makes the simulation prone to geometry errors at small deformations leading to incomplete results (Chapter 2). Various regularization techniques have been developed that introduce some form of a length scale to minimize mesh dependence without discretizing the mesh to the order of the shear band thickness. Regularization techniques that have been used for problems involving strain-softening clays include pore fluid coupling (e.g., Thakur et al. 2006), rate dependent models (e.g., Park 2011, Oathes and Boulanger 2020), extended finite elements (e.g., Septanika et al. 2007), interface elements (e.g., Jostad and Andersen 2004), non-local constitutive models (e.g., Brinkgreve 1994), and softening-scaling (e.g., Pietruszczak and Mróz 1981, Kiernan and Montgomery 2018, Zabolotnii et al. 2021). Thakur et al. (2006) found that pore-fluid coupling alone did not sufficiently reduce mesh dependency and suggested that strain rate dependence may be incorporated into effective stress-based models may better address mesh dependency. Oathes and Boulanger (2020) incorporated rate dependence into the effective stress-based model PM4Silt to delay the onset of localization, but a regularized solution is only observed before significant strength loss occurred.

Kiernan and Montgomery (2018) implemented a softening-scaling approach with a total stress-based strain-softening model in dynamic Fourth Avenue landslide simulations and found that mesh dependency is reduced, but a low peak and residual strength values and fast softening rates are required to produce deformations consistent with site observations. Zabolotnii et al. (2021) investigate mesh dependency of a total stress-based model in numerical simulations of the Mount Polley Tailings Dam failure that occurred under static loading. Zabolotnii et al. (2021) modified the softening-scaling approach used by Kiernan and Montgomery (2018) to consider a lower limit state which assumes a shear band of zero thickness and instant strength loss occurs once plastic shear strain becomes greater than zero. They also considered an upper limit state which assumes an infinitely thick shear band and no strength loss occurs as plastic shear strain accumulates. Zabolotnii et al. (2021) suggested that mesh refinement below the actual shear band thickness may be required to eliminate mesh dependence even using the lower limit state.

Regularization techniques may reduce mesh dependency, but they still must be calibrated to an appropriate softening rate (i.e., the interval of strain over which softening occurs) to provide realistic results. Determining an appropriate softening rate for sensitive clays involves significant uncertainty due to difficulties in estimating the thickness of the shear band. Strains from lab tests on strain-softening clays are typically calculated using displacement measurements on the overall sample and do not measure the larger strains concentrated within the shear band. Previous researchers have recognized this uncertainty in reporting strain values for lab tests involving strain-softening clays and have opted to instead report results in terms of shear displacement (e.g., Stark and Contreras 1998).

This manuscript provides guidance regarding constitutive model calibration procedures based on shear displacement to overcome some uncertainty in estimating appropriate shear strain magnitudes. The results from Chapter 2 suggest that displacement-based calibrations may reduce mesh size dependence in simulations using PM4Silt. Displacement-based calibrations work in a similar fashion to softening-scaling based regularization techniques as remolding strains are essentially scaled based on element height and shear displacement. Idriss (1985) related Fourth Avenue landslide displacements at the ground surface to the undrained shear strength of the BCC but displacement-based calibrations to reduce mesh size dependence in NDAs have not been studied for this case history.

The goal of this study is to compare the ability of a total stress-based constitutive model (RSSMC) versus an effective stress-based model (PM4Silt) to model cyclic softening of the sensitive Bootlegger Cove Clay (BCC) at the Fourth Avenue landslide. Field-scale simulations of the Fourth Avenue Landslide show that both models can reasonably replicate upper crest displacements observed at the Fourth avenue site, but PM4Silt better captures the observed deformation patterns. Another objective of this work is to provide insight as to when it may be necessary to use a more advanced effective stress-based constitutive model and when a total stress-based model may serve as a reasonable approximation for numerical analyses involving strain-softening clays. Effective stress-based models are shown to be necessary in cases where an understanding of element level response is important or deformations outside of the major failure mass need to be estimated. Guidance is also provided regarding the use of displacement-based calibrations to reduce mesh size dependence in NDAs involving strain-softening clays. Displacement-based calibrations are shown to reduce the effect of the chosen mesh size on upper crest displacement magnitudes, but additional aspects of mesh size dependence are still present.

3.2 CASE HISTORY AND SELECTED SOIL PROPERTIES

The case history used for analyses in this chapter is the Fourth Avenue Landslide. A detailed description of the Fourth Avenue Landslide and available site explorations are presented in Chapter 2. Selected soil properties from Chapter 2 are presented in Table 2-2. Specific soil properties selected for analyses in this chapter are discussed in this section. Chapter 2 presents a plot residual undrained shear ratios ($S_{u,res}/\sigma'_v$) as reported by previous researchers. The $S_{u,res}/\sigma'_v$ values range from about 0.03-0.09 with an average value of 0.06. The ratio of the peak and residual undrained shear strengths is defined as the soil sensitivity (S_t); which describes the amount of strength loss that will occur during softening. Residual undrained shear strength of clays has been shown to be relatively independent of shearing rate (e.g., Biscontin and Pestana 2001, Scaringi and Di Maio 2016). However, peak undrained shear strength of clays has been shown to increase as shearing rate is increased (e.g., Lefebvre and LeBoeuf 1987, Lefebvre and Pfendler 1996, Boulanger et al. 1998, Diaz-Rodriguez et al. 2009). This rate dependent increase in shear strength is often accounted for by applying a strain rate factor that typically ranges from 1.2-1.4 (e.g., Idriss and Boulanger 2008, Beaty and Dickenson 2015) when using rate independent models such as PM4Silt or RSSMC.

The uncertainty in selecting an appropriate strain rate factor further increases the uncertainty in selecting appropriate $S_{u,pk}/\sigma'_v$ values for use in the numerical simulations. This study uses peak undrained shear strength ratios for earthquake loading ($S_{u,pk,eq}/\sigma'_v$) of 0.26 and 0.29 to account for the scatter in the test data and loading rate effects. A peak strength ratio of 0.29 is used for the baseline analyses to examine if the model could reproduce the deformation magnitudes observed at the Fourth Avenue site using a higher peak strength to account for strain rate effects due to earthquake loading. The average residual strength ratio of 0.06 is used in the baseline analyses and a residual strength ratio of 0.045 is also considered in the sensitivity analyses.

The softening rate, or strain interval over which softening occurs, is an important parameter to define for model calibration. There is significant uncertainty in defining the softening rate once localization initiates because it is difficult to estimate the shear band thickness where strength loss occurs (Jostad et. al. 2006). Test results from strain-softening clays may be expressed in terms of shear displacement, rather than strain, if the shear band thickness can't be determined (e.g., Stark and Contreras 1996, 1998). BCC peak strengths from CVRS tests (Stark and Contreras 1998) were reached in about 1.1 mm to 1.8 mm of shear displacement and residual strengths were achieved at shear displacements of 6 cm to 13 cm. Idriss (1985) proposed that residual strengths at the Fourth Avenue site were likely mobilized at ground surface displacements of about 15 cm, but ground displacements are not easily translated to shear strain in the BCC. Beaty and Dickenson (2015) examined softening rates corresponding to full strength loss after shear strains of 10% to 240% in numerical analyses using a hysteretic constitutive model, but found that ground displacements consistent with site observations were only produced when strength loss occurred after 10% shear strain. This study assumes the BCC fully softens in 15 cm of shear displacement ($\delta_{rem} = 15\ cm$) which equates to about 12% shear strain in the 1.3 m tall BCC elements used in the simulations.

The other strata existing at the Fourth Avenue site are not as well characterized as the critical BCC layer. The interbedded zone contains alternating layers of silty clays, sandy silts and overconsolidated BCC with an OCR ranging from 3 to 4 (Idriss 1985). No OCR data could be found for the deeper stiff clay, but CPT data collected by Woodward-Clyde (1982) indicated $S_{u,pk}/\sigma'_v$ ranges from 0.10 to 0.60 applying the average empirical cone factor (N_{kt}) of 14 (Robertson (2009). A $S_{u,pk}/\sigma'_v$ value of 0.35 is chosen for the interbedded and stiff clay layers considering the results of both tests. SPT data collected by Shannon and Wilson (1964) is used to estimate strength characteristics of the sand and outwash layers. The average $(N_1)_{60}$ value for the sand layer is calculated to be 50 and the outwash layers had an $(N_1)_{60}$ value of 45. Idriss (1985) discusses that these high blow counts indicate dense soils that are probably not vulnerable to liquefaction. The $(N_1)_{60}$ values for these layers are used to calibrate PM4Sand which is the constitutive model used for these layers in the full scale simulations.

3.3 NUMERICAL SIMULATION PROCEDURE AND CALIBRATIONS

The simulations presented in this study are performed using the two-dimensional finite difference software Fast Lagrangian Analysis of Continua (FLAC 8.0, Itasca 2016). Single element DSS drivers as well as field-scale simulations of the Fourth Avenue landslide are utilized. The single element DSS drivers are used for calibration and to examine the single element model behaviors under controlled loading conditions. The field-scale simulations are used to investigate the ability of each model to reproduce the deformation patterns observed at the Fourth Avenue site and to compare the corresponding element level behavior of BCC zones in the field-scale model.

Prior to calibration, soil stiffness is set to the desired value using a shear wave velocity of 220 m/s at a depth of 25m as measured by Nath et. al. (1997). For PM4Silt this is done by setting the shear modulus coefficient (G_o) to achieve the desired shear wave velocity of 220 m/s using the mean stress from the static equilibrium stage of the field-scale simulations at 25m depth to the left of the slope (Figure 2-1) where approximately zero shear stress exists to be consistent with where the shear wave velocity was measured. For RSSMC, the shear modulus is set using a shear wave velocity of 220 m/s and the BCC density. The RSSMC bulk modulus is then set using the calculated BCC shear modulus and Poisson's Ratio (υ) required to produce reasonable coefficient of lateral earth pressure conditions as discussed in the *Field-scale Simulations* section below.

3.3.1 Single element Calibration Procedure and Comparison

This section will present results from single element DSS drivers used for calibration and comparison of single element response for each selected constitutive model under controlled loading conditions. Calibration is an iterative process where input variables for each model are adjusted to obtain a desired model behavior in terms of peak and residual strength, softening rate, and modulus reduction and damping response. The following sections discuss calibration of the PM4Silt and RSSMC models for the BCC layers. The non-BCC PM4Silt layers and the PM4Sand layers are calibrated in a similar fashion as discussed below. Further details on the calibration of these layers can be found in Chapter 2.

The calibrations shown below are for the baseline mesh that uses 1.3 m tall BCC elements and are based on shear displacement rather than shear strain. Determining an appropriate softening rate for sensitive clays involves significant uncertainty due to difficulty estimating the thickness of the shear band where the majority of the strains are concentrated. Strains from lab tests on strain-softening clays are typically reported based on the specimen height and do not consider the larger strains concentrated within the shear band. The uncertainty in estimating strain magnitudes has led the author to develop a calibration procedure based on shear displacement rather than shear strain. BCC elements heights used in the calibration drivers are set equal to the element heights used the field-scale simulations. The constitutive models are then calibrated to a peak strength and to achieve residual strength in a specified magnitude of shear displacement. Additional calibrations should be performed anytime the element height is changed. For example, when investigating the effects of mesh density, PM4Silt should be calibrated to achieve full softening in the same magnitude of shear displacement for each mesh size. Chapter 2 showed that mesh size dependence of the PM4Silt model is reduced when a coarser mesh is calibrated to match a finer mesh in terms of shear displacement to fully remold the BCC. Displacement-based calibrations do not require the user to assume a shear band thickness but instead assume that the majority of shear displacement occurs within the shear band so that the element level shear displacement is not significantly larger than would occur within the shear band. The assumption that the shear displacement is not significantly different at the shear band and element levels is also used in the softening-scaling approach as it is the constant used to convert element level strains to those in the shear band.

3.3.2 Strain Controlled Undrained Monotonic DSS

The strain controlled undrained monotonic driver is used primarily to calibrate the models in terms of peak strength, residual strength, and softening rate as shown in Figure 3-1. The residual strength ratio ($S_{u,res}/\sigma'_v$) of PM4Silt is set using the $S_{u,cs,eq}/\sigma'_v$ input parameter. The $n^{b,wet}$ parameter is then iteratively adjusted to achieve the desired PM4Silt peak strength ratio ($S_{u,pk}/\sigma'_v$). The desired softening rate is achieved by adjusting the contraction rate parameter (h_{po}). The PM4Silt calibration shown in Figure 3-1 corresponds to $S_{u,res}/\sigma'_v$ value of 0.06, a $S_{u,pk}/\sigma'_v$ value of 0.29, and a softening rate which converges to residual strength in about 15 cm of element level shear displacement (12% element level shear strain). The remolding displacement for the BCC is therefore estimated to be 15cm based on field observations. The results of constant volume ring shear (CVRS) tests on BCC performed by Stark and Contreras (1998) are also shown in Figure 3-1 for a vertical consolidation stress of 100 kPa to be consistent with the DSS driver. The BCC from the CVRS shows a very stiff initial response reaching the peak strength at significantly less shear displacement than the PM4Silt calibration. The initial softening curve from the CVRS results is initially much steeper than the PM4Silt calibration but the two curves match fairly well at shear displacements greater than 6 cm suggesting the residual strength is reached at similar levels of shear displacement.

For the RSSMC model, the desired $S_{u,pk}/\sigma'_v$ is specified by the user. The BCC sensitivity ($S_t = S_{u,pk}/ S_{u,res}$) value is then specified to achieve the desired $S_{u,res}/\sigma'_v$ value. The RSSMC calibrations shown in Figure 3-1 correspond to $S_{u,res}/\sigma'_v$ value of 0.06, a $S_{u,pk}/\sigma'_v$ value of 0.29, and δ_{rem} values which respectively achieve residual strength in about 8 cm and 15cm of element level shear displacement. Shear displacement levels of 8 cm and 15 cm equate to about 6% and 12% of element level shear strain in the 1.3m tall BCC elements used in the baseline simulations in this study. The term RSSMC-RH is used to designate RSSMC simulations utilizing Rayleigh damping and hysteretic damping. Selection of damping parameters will be discussed in the next section.

Figure 3-1 illustrates some key differences between each constitutive model under undrained monotonic loading. PM4Silt begins to exhibit some nonlinear behavior on the initial portion of the curve at a shear stress ratio of about 0.10 while the RSSMC models don't appear to exhibit any nonlinear response until very close to the peak of the curves. This is expected as the RSSMC is elastic until yielding. The PM4Silt calibration is shown to fully reach the peak strength while the RSSMC models begin softening at lower horizontal shear stress values. This difference in peak horizontal stress ratio occurs because the Mohr-Coulomb yield surface is formulated in principal stress space so the shear stress on the horizontal plane is less than the maximum shear stress within the element. The author has confirmed that the peak deviatoric stress ratios (q/σ'_v) for the RSSMC elements correspond to the desired $S_{u,pk}/\sigma'_v$ values, but have decided to present the results in terms of horizontal shear stress ratio for simplicity. It should also be noted that the q/σ'_v

values for the PM4Silt calibrations are consistent with the peak horizontal shear stress values corresponding to $S_{u,pk}/\sigma'_v$.

PM4Silt also exhibits nonlinearity in the softening portion of the curve causing the model to slowly converge towards the residual strength value which is consistent with the strain-softening behavior of clays observed in previous lab tests (e.g., Moriwaki et. al. 1985, Burland 1990, Stark and Contreras 1998, Gylland et. al. 2014). The RSSMC model is formulated to use linear softening and reach the residual strength values at prescribed values of shear displacement. Two softening rates (8 cm and 15 cm) are used in the simulations to account for this difference in softening behavior. RSSMC is calibrated to achieve full softening in approximately the same level of shear displacement as the PM4Silt model (15 cm) and RSSMC is also calibrated to better match the softening portion of the PM4Silt curve by allowing it to fully soften in only 8 cm shear displacement.

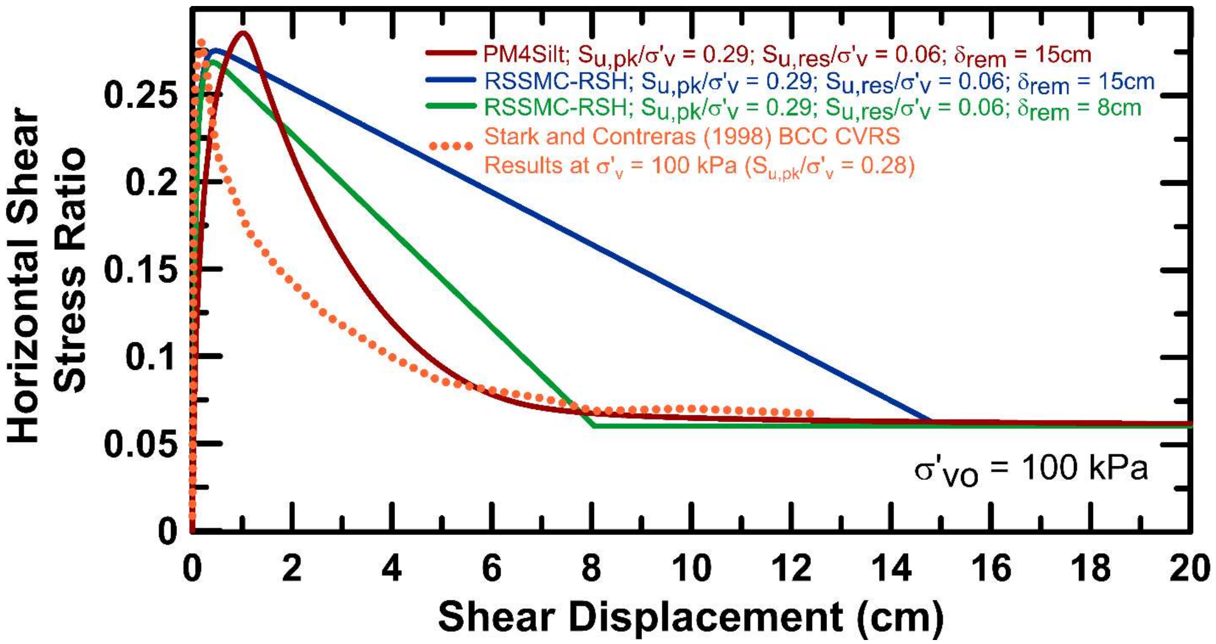

Figure 3- 1: Strain controlled undrained monotonic single element DSS calibration results for PM4Silt and RSSMC models compared to CVRS results from Stark and Contreras (1998)

3.3.3 Strain and Stress Controlled Undrained Cyclic DSS

The strain controlled undrained cyclic DSS driver is primarily used to calibrate shear modulus reduction and damping ratio behavior for the chosen constitutive models. The cyclic drivers in this study use a driving frequency of 1 Hz to match the center frequency used for models that include Rayliegh damping. The models are calibrated to approximately match the modulus reduction and damping ratio curves provided by Vucetic and Dobry (1991) for clays with a plasticity index (PI) of 15 which roughly corresponds to the average PI of the BCC (Shannon and Wilson 1964).

The PM4Silt model includes intrinsic damping and can be calibrated to match modulus reduction and damping ratio curves by adjusting the parameter h_o. Boulanger and Ziotopoulou (2018) recommend including minimal Rayleigh damping of about 0.5% to reduce numerical noise. All PM4Silt simulations utilize 0.5% Rayleigh damping at a center frequency of 1 Hertz which roughly corresponds with the predominant frequencies observed in spectral velocity plots of the input motions. The PM4Silt parameter h_o is adjusted to match the target curve. Figure 3-2a illustrates that PM4Silt produces a modulus reduction response that is in reasonable agreement with the PI =15 curve over the full range of reported strain values. Figure 3-2b shows that PM4Silt slightly underestimates the damping behavior at low strains and slightly overestimates damping behavior at higher strain values.

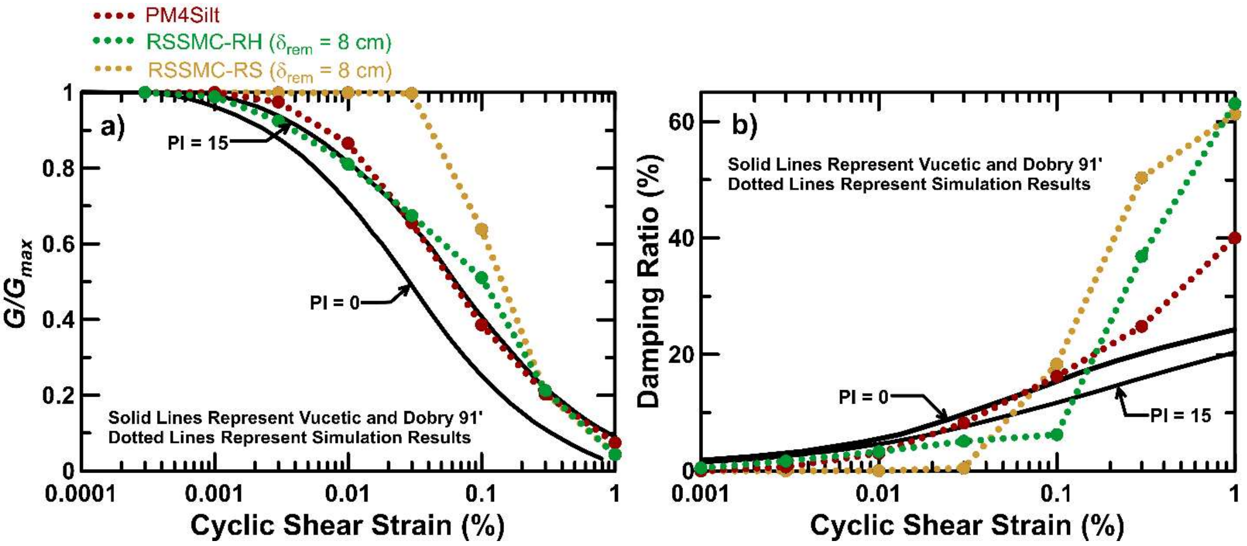

Figure 3- 2: Strain controlled undrained cyclic single element DSS calibration results for PM4Silt, RSSMC-RH and RSSMC-RS calibrations using $S_{u,pk}/\sigma'_v = 0.29$ and $S_{u,res}/\sigma'_v = 0.06$

The RSSMC model does not include any damping in the elastic region so external damping should be used to achieve appropriate modulus reduction and damping response. The RSSMC model is calibrated using two different scenarios for material damping. The first scenario uses the sigmoidal hysteretic damping as implemented in FLAC 8.0 (Itasca 2016). The three input parameters are calibrated to match the same Vucetic and Dobry (1991) curves. Rayleigh damping of 0.2% at a center frequency of 1 Hertz is also included to remove high frequency noise as recommended by Itasca (2016). The RSSMC model with hysteretic and Rayleigh damping is referred to as RSSMC-RH. Figure 3-2a shows that the modulus reduction behavior of the RSSMC-RH model is in reasonable agreement with the PI=15 curves over the full range of reported strain values. Figure 3-2b shows that the RSSMC-RH model slightly underestimates the damping behavior at strains less than 0.1% and greatly overestimates the damping behavior once 0.1% strain is surpassed. This overestimation is due to the large amount of energy that is dissipated after yielding occurs.

The RSSMC model is also calibrated to include only Rayleigh damping to investigate how hysteretic damping influences the model response. The RSSMC model that includes only Rayleigh damping is referred to as RSSMC-RS. The RSSMC-RS calibration includes 3% stiffness-proportional Rayleigh damping at a center frequency of 1 Hertz to account for the lack of hysteretic damping. The mass proportional damping Rayleigh damping term is omitted as it may inhibit yielding at high amounts of Rayleigh damping and is recommended to be excluded from regions of plastic flow (Itasca 2016). Figure 3-2a shows that the RSSMC-RS model underestimates the modulus reduction behavior at most strain levels below 0.3%. Figure 3-2b shows that the RSSMC-RS model significantly underestimates the damping behavior at small strains and greatly overestimates the damping behavior at larger strains. Field-scale simulations will be performed using each of these RSSMC calibrations to examine how these differences in modulus reduction and damping behavior affect the field-scale solution.

Figure 3-3a compares the cyclic stress paths of each model using the strain controlled undrained cyclic DSS driver. It should be noted that the stress path for RSSMC-RS lies directly on top of the stress path for the RSSMC-RH model and is excluded from Figure 3-3a. The PM4Silt stress path in Figure 3-3a is shown to be influenced by changes in effective stress due to excess pore pressure generation while the stress paths of the RSSMC models remain close to the initial vertical consolidation stress. PM4Silt exhibits a consistent decrease in effective stress until the residual strength ($S_{u,res}/\sigma'_v = 0.06$). where slight increases in effective stress are observed. The RSSMC models show only slight variations in effective stress that appear to occur during softening at shear stress ratios between the peak ($S_{u,pk}/\sigma'_v = 0.29$) and residual ($S_{u,re}/\sigma'_v = 0.06$) undrained shear strength ratios. The small variation in effective stress occurs because no dilatancy is incorporated in the RSSMC model and so no excess pore pressures are generated in these undrained simulations.

The stress ratio controlled undrained cyclic DSS driver can also be used to calibrate the contraction rate parameter (h_{po}) in PM4Silt to target stress ratios at a given number of cycles to 3% strain. The author has found that this approach is not necessarily suitable for soils that exhibit significant strain-softening and instead adjust h_{po} to achieve the desired softening rate in undrained monotonic loading as described previously. This study uses the stress ratio controlled undrained cyclic DSS driver to compare the cyclic response of the chosen models. Figure 3-3b illustrates the shear stress ratios required to produce 3% strain in a given number of uniform loading cycles for each model. PM4Silt is shown to reach 3% strain in fewer cycles than the RSSMC models for a given stress ratio value except near the peak and residual strengths, where the curves agree. The shape of the PM4Silt curve in Figure 3-3b is a smooth curve while the RSSMC model remains elastic for loading levels below the peak strength and fails in one cycle for loading levels at the peak strength. This behavior further illustrates the nonlinear stress-strain relationship of the PM4Silt model versus the stress-strain relationship of the RSSMC models that utilize a piecewise linear stress strain relationship (Figure 3-1). It should also be noted that the RSSMC ($\delta_{rem} = 8\ cm$) model with hysteretic and Rayliegh damping reaches 3% strain in about 20 less cycles than the PM4Silt model near the residual strength value of 0.06. The RSSMC ($\delta_{rem} = 8\ cm$) model is therefore expected to fully soften quicker than the PM4Silt model even though the PM4Silt model may begin generating ground displacements at lower strain values in the field-scale simulations.

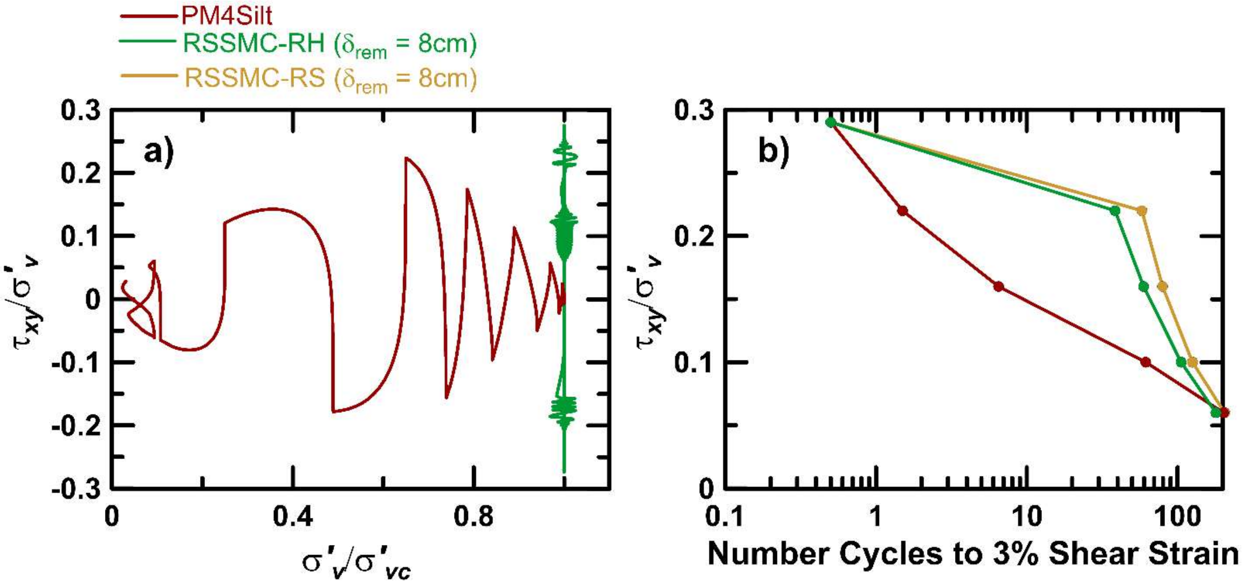

Figure 3- 3: (a) Strain and (b) stress ratio controlled undrained cyclic single element DSS calibration results for PM4Silt, RSSMC-RH and RSSMC-RS calibrations using $S_{u,pk}/\sigma'_v$ = 0.29 and $S_{u,res}/\sigma'_v$ = 0.06

3.3.4 Calibration of Unsaturated BCC Zones

Another important consideration in the field-scale simulations is that some of the BCC zones near the toe of the lower slope are above the water table and are not saturated. Modeling techniques for cyclic loading of unsaturated soils are not as well developed as those for fully saturated soils due to complications and uncertainty in modelling two-phase flow phenomena such as suction, relative permeability, and the degree of saturation of the fluid and gas phases (Oka et al. 2018). Previous studies on unsaturated clays have shown that there is an increase in peak strength, and increase in small strain shear stiffness, and a more brittle loss of strength compared to saturated soils. Cunningham et al. (2003) performed triaxial and unconfined compressions tests on saturated and unsaturated silty clay specimens and the results show that the peak deviator stress is about 40% higher for the unsaturated cases followed by a more abrupt loss of strength once the peak strength is surpassed. Oka et al. (2018) developed a constitutive model for partially saturated clays and used it to compare the behavior of saturated and partially saturated clays using plane strain compression simulations. Their studies suggest that the partially saturated soils exhibit peak strength increase of about 60%, and small strain stiffness increase of 45%.

The PM4Silt and RSSMC models are also calibrated to account for the shear modulus (G_o) and peak strength ($S_{u,pk}/\sigma'_v$) increase in the unsaturated BCC zones. The RSSMC and PM4Silt calibrations for the unsaturated BCC zones included a peak strength of about 0.34 based on this limitation of the PM4Silt model. This equates to a peak strength increase of about 15% to 24% for saturated peak strengths of 0.29 and 0.26 respectively. This lower increase is used, due to the difficultly in calibrating the PM4Silt model to peak strengths that are significantly higher than the critical state strength. The unsaturated BCC calibrations for the RSSMC and PM4Silt models also included a small strain shear stiffness (G_o) increase of 45% and δ_{rem} values that cause the BCC zones to fully soften about 33% faster than the calibrations for the saturated BCC zones.

3.4 FIELD-SCALE SIMULATION PROCEDURE

The field-scale numerical simulations are performed in a series of stages. The model is first brought to static equilibrium by building the model row by row with no water table. An elastic-plastic Mohr-Coulomb model is used for all elements in this stage. The shear modulus and friction angle for the PM4Silt simulations are set to match those used in the dynamic simulations. The water table is then raised row by row by to the desired height by applying constant head boundary conditions at the lateral model boundaries. This process yields a normally consolidated stress profile that may or may not be a reasonable representation of the lateral stress condition for the clay layers at the site. Coefficient of lateral earth pressure coefficients (K_o) values are estimated for the BCC, stiff clay and interbedded layers according to equation 3-1 (Meyerhoff 1976) to produce a more realistic stress profile prior to dynamic loading. $K_{o,NC}$ is assumed to be 0.45 for the clay layers. The OCR of the BCC layer is estimated to be 1.3 and the OCR of the stiff clay and interbedded layers are estimated to be 3.5.

$$K_{o,OC} = K_{o,NC}(OCR)^{0.5} \tag{3-1}$$

The sand and outwash layers are assumed to have K_o values of 0.5. The values of Poisson's ratio (υ) for each layer are adjusted during static initialization to achieve to achieve the desired K_o values. These parameters are returned to their original values prior to the dynamic loading stage. A fixed based boundary condition and roller boundaries to restrict horizontal movement at the lateral model extents are used during the static initialization stages.

Once the static equilibrium stages are complete, the constitutive models in each layer are updated for dynamic loading. PM4Silt is used for the stiff clay and interbedded zones and PM4Sand is used for the sand and outwash zones in all simulations. The BCC is modeled using either PM4Silt or RSSMC and the influence of the choice of model on the numerical solution is examined. Pore fluid is allowed to flow during dynamic loading. The pore fluid modulus of the BCC, stiff clay and interbedded zones are set to the bulk modulus value of water ($2.0*10^9$ Pa). The pore fluid modulus of the sand and outwash zones are set to 101 kPa to allow water to flow more easily through these dense coarse grained layers. A quiet boundary is applied to the model base where input motions are applied as stress waves. Free-field boundaries are applied at the sides of the model to further minimize reflected wave energy. Details regarding the formulation and implementation of the quiet and free-field boundaries used in this study are presented in Itasca (2016).

3.4.1 Earthquake Input Motions

Strong motion records of the Great Alaska Earthquake are not available so ground motion records from the 2010 Chile (M_w 8.8) subduction zone quake were downloaded from CESMD (2017) to simulate dynamic loading. Pre-processed recordings are available for the three stations (TAL, CUR, and HUA) selected from the 2010 Chile earthquake. The horizontal component from each station with the higher Arias intensity (TAL-L, CUR-NS, and HUA-T) are utilized in the field-scale simulations.

Beaty and Dickenson (2015) developed a target response spectrum for the Fourth Avenue site using ground motion prediction equations for subduction zone earthquakes. Each of the 3 input motions are linearly scaled to approximately match this target spectrum over a period range of 0.6 to 1.0 seconds. Beaty and Dickenson (2015) suggest the small strain period at the south end of the site (Figure 2-4) is about 0.6 seconds. The spectral accelerations of the scaled motions exceed the target spectrum at low periods, but the range of spectral accelerations from the scaled motion agree with the range of spectral accelerations from regional ground motion simulations of the Great Alaska Earthquake performed by Mavroeidis et. al. (2008). PGAs of the scaled records range from 0.16g to 0.35g which is also consistent with the simulations performed by Mavroeidis et. al. (2008) and the PGA range reported by Moriwaki et. al. (2008). Properties of each of the selected input motions, the applied scaling factors, and the pseudo spectral response spectra in comparison to the target spectrum are reported in Kiernan and Montgomery (2019) and Chapter 2.

3.5 FIELD-SCALE COMPARISONS

This section describes the results of the field scale simulations performed for the Fourth Avenue landslide case history using the PM4Silt and RSSMC constitutive models. Baseline analyses are presented first, and results are compared to field observations. The element level response inside the failure plane for each model is examined and compared. The effect of input motion, peak strength and residual strength on the numerical solution is analyzed for each model. Mesh dependence of the solution is examined and the ability of a displacement-based calibration procedure to reduce mesh dependence is discussed.

3.5.1 Baseline Analyses Displacements

Figure 3-4 shows upper crest displacement versus dynamic time for the PM4Silt and RSSMC model calibrations. The PM4Silt and RSSMC (δ_{rem} = *8 cm*) models both produce large upper crest displacements that are fairly consistent with site observations; while the RSSMC (δ_{rem} = *15 cm*) model produces smaller displacement magnitudes as the BCC in this simulation requires more shear displacement to fully soften. Softening of the BCC zones begins at the start of strong shaking (~20 seconds for all models as shown by the increase in upper crest displacements in Figure 3-4). Upper crest displacement in the PM4Silt model gradually increase until about 70 seconds into the input motion as BCC zones continue to soften. The velocity of the upper crest in the PM4Silt model then increases between 70 and 90 seconds as BCC zones along the failure plane begin to reach the residual strength. After 90 seconds of shaking, the majority of BCC zones along the failure plane in the PM4Silt model have fully softened and the displacement rate decreases as the upper crest displacement approaches a final magnitude of about 3.6m.

The transitions in softening behavior observed in the PM4Silt model are not as obvious in the RSSMC calibrations using hysteretic damping (RSSMC-RH in Figure 3-4). The RSSMC (δ_{rem} = *8 cm*) model achieves full softening of the BCC zones along the deeper failure plane about 35 seconds into strong shaking and reaches a final upper crest displacement of almost 4.0 m before the simulation is halted at 52 seconds due to geometry errors. The upper crest displacement in the RSSMC-RH (δ_{rem} = *15 cm*) model gradually increases to a final magnitude of about 0.9m. The failure plane in the RSSMC-RH (δ_{rem} = *15 cm*) model does not fully develop as the large majority of BCC zones do not reach the residual strength. This prevents the failure plane from reaching the ground surface behind the upper crest inhibiting large upper crest displacements

Simulations are also performed for the RSSMC (δ_{rem} = *8 cm*) model without hysteretic damping. These include simulations using only stiffness-proportional Rayleigh damping (RSSMC-RS) and using both mass- and stiffness-proportional Rayleigh damping (RSSMC-RSM). The results using only stiffness-proportional damping show a similar displacement pattern to the RSSMC model with hysteretic damping (δ_{rem} = *8 cm,* RSSMC-RH) except that full softening of the BCC zones is delayed until about 50 seconds into the motion. The model with mass- and stiffness-proportional Rayleigh damping produces smaller displacements that are more consistent with the RSSMC-RH (δ_{rem} = *15 cm*) calibration. This difference in results from this simulation is likely due to the mass-proportional Rayleigh damping inhibiting yielding as discussed by Itasca (2016). This is a numerical issue and not a true representation of the material behavior and this exercise highlights the importance of examining the effects of numerical choices on the simulation results.

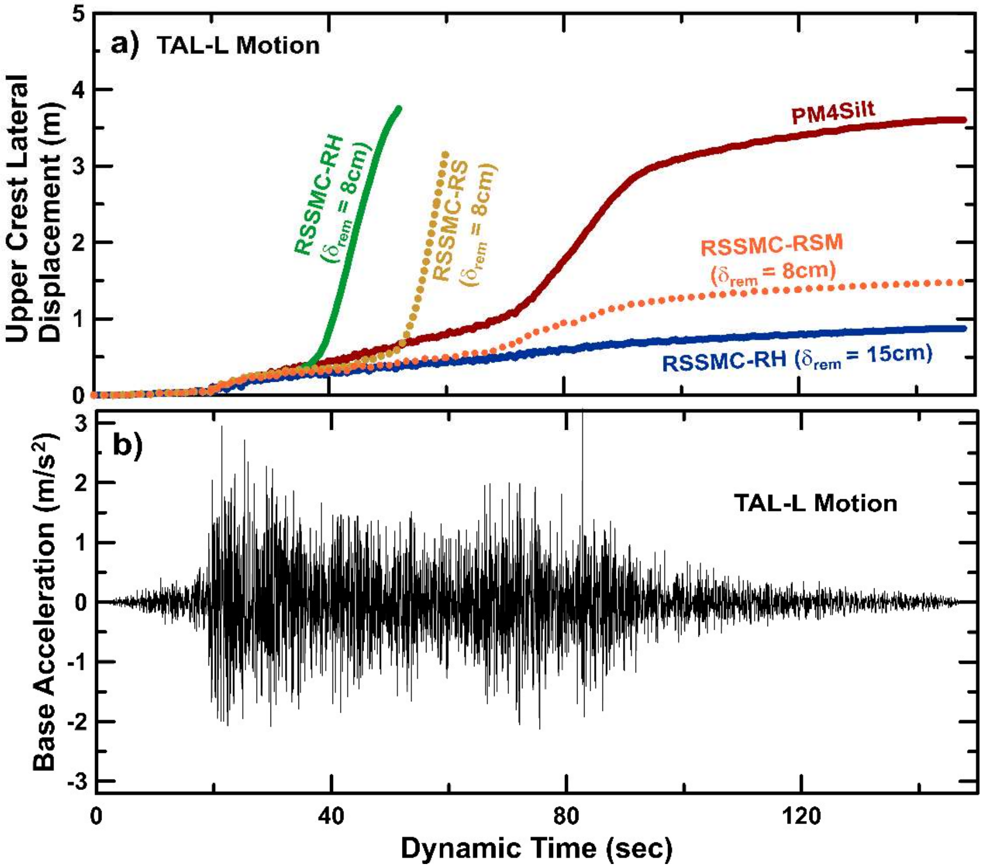

Figure 3- 4: Time histories of (a) upper crest lateral displacement using the TAL-L input motion using $S_{u,pk}/\sigma'_v = 0.29$ and $S_{u,res}/\sigma'_v = 0.06$, (b) base (input) accelerations for TAL-L input motion

Figure 3-5 shows lateral displacement contours for each of the studied models. The PM4Silt model shows a single deep failure plane that forms along the bottom of the BCC layer from the toe of the lower slope to just beneath the upper crest where it turns upward and reaches the ground surface. The displacement contours in the PM4Silt model also shows minor ground deformations outside of the major failure mass (behind the upper crest and beyond the toe of the lower slope) and vertical displacement contours (Figure 3-6) show pressure ridges near the toe of the lower slope; both of which are consistent with site observations (Chapter 2). Ground deformations in the RSSMC models are conversely limited to within the major failure mass and pressure ridges are observed near the middle slope which were not reported at the site.

The RSSMC models that do not include mass-proportional Rayleigh damping (RSSMC-RH) show two separate failure planes. A deep failure plane exists near the bottom of BCC layer beneath the upper crest that turns up toward the top of the BCC layer near the middle slope. These models also show a second shallower failure plane that forms near the top of the BCC layer extending from the middle slope towards the toe of the lower slope. The RSSMC model with mass and stiffness-proportional Rayleigh damping (RSSMC-RSM) produces a shallow failure plane that remains at the top of the BCC layer from the upper crest to the lower crest.

Figure 3-6 shows vertical displacement contours for each of the studied models. Shannon and Wilson (1964) report a zone of pressure ridges near the toe of the lower slope. The PM4Silt model shows some positive vertical displacements just past the toe of the slope consistent with the formation of pressure ridges. The RSSMC models do not show significant evidence of pressure ridges near the toe of the lower slope. The RSSMC-RS ($\delta_{rem} = 8\ cm$) and RSSMC-RH ($\delta_{rem} = 8\ cm$) simulations do show evidence of pressure ridges near the middle slope, but pressure ridges in this area were not reported by Shannon and Wilson (1964). The formation of pressure ridges near the middle slope in the RSSMC-RS ($\delta_{rem} = 8\ cm$) and RSSMC-RH ($\delta_{rem} = 8\ cm$) simulations occur near the location where the failure plane transitions from deep to shallow. The transition from a deep to a shallow failure surface creates a ramp near the middle slope that forces the zones in that area upward as they slide laterally. The failure plane existing primarily at the bottom of the BCC layer, as observed in the PM4Silt simulations, force zones upward as they slide laterally toward the stepped contact between the BCC and stiff clay layers near the toe of the slope. The lack of pressure ridge observations near the middle slope, and the lack of pressure ridges near the toe observed in the RSSMC simulations, suggest that the failure plane at the Fourth Avenue site is likely more consistent with that produced in the PM4Silt simulations. Differences in the failure plane formation and deformation patterns will be examined at the element level in later sections.

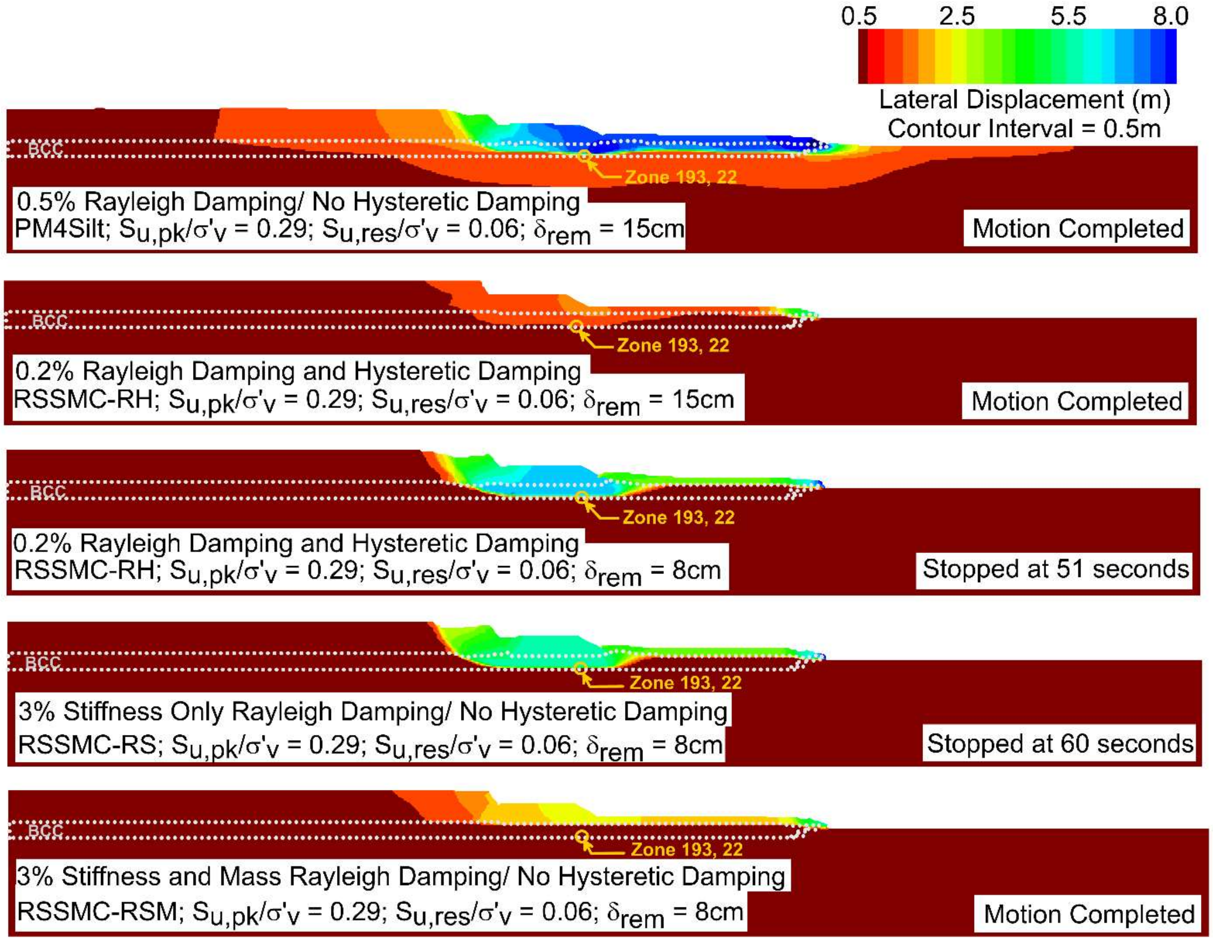

Figure 3- 5: Lateral displacement contours for baseline field-scale analyses using TAL-L input motion

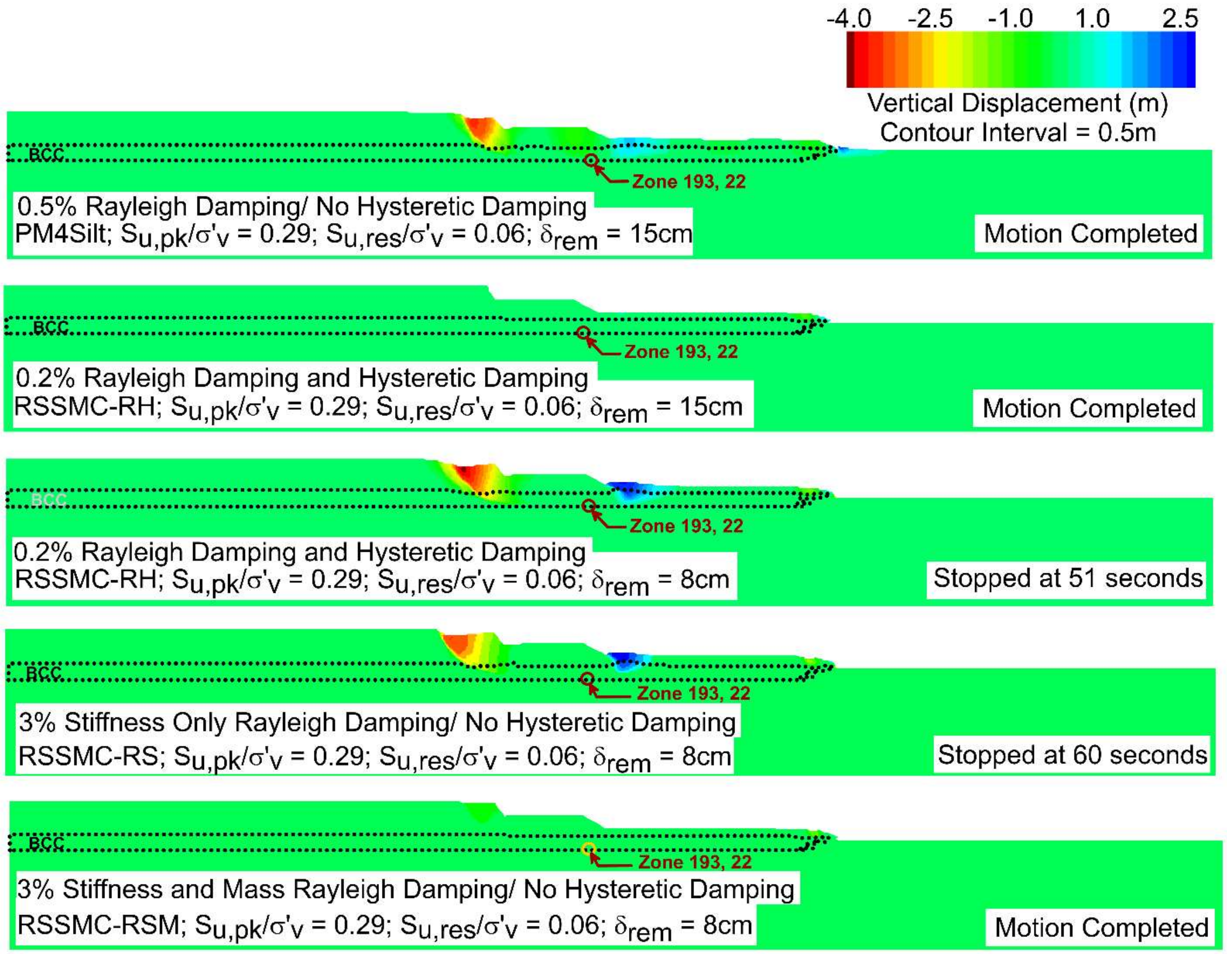

Figure 3- 6: Vertical displacement contours for baseline field-scale analyses using TAL-L input motion

3.5.2 Element Level Comparison

This section will compare element level behavior from the field-scale simulations using histories from zones within the horizontal portion of the deeper failure plane just behind the middle slope. Figure 3-7a shows histories of horizontal shear stress versus vertical effective stress the PM4Silt and RSSMC ($\delta_{rem} = 8\ cm$) simulations. Figure 3-7a shows that PM4Silt is able to account for reduction in effective stress during loading as expected in soft clays as they attempt to contract during undrained shearing. This reduction in effective stress in the PM4Silt simulation is accompanied by a decrease in resistance to horizontal shear stress which is consistent with observations of strain-softening clays by previous researchers (e.g., Hyodo et al. 1999, Gylland et al. 2014, Thakur et al. 2017). The RSSMC-RH (δ_{rem} = *8 cm*) simulation does not exhibit much decrease in effective stress due to its total stress-based formulation. Figure 3-7c shows time histories of pore pressure for each of the PM4Silt and RSSMC simulations. The PM4Silt simulation begins to generate significant pore pressure about 20 seconds into the motion which is consistent with the time that upper crest displacement begins to increase as shown in Figure 3-4. The RSSMC models conversely show very little pore pressure generation during shaking which is consistent with the lack of decrease in vertical effective observed for the RSSMC-RH (δ_{rem} = *8 cm*) simulation shown in Figure 3-7a. The differences in the effective stress and pore pressure responses between the PM4Silt and RSSMC models illustrates the ability of effective stress-based models to account for coupling between the soil and pore fluid compared to total stress-based model formulations.

Figure 3-7b shows histories of horizontal shear stress versus maximum shear strain increment (SSI) for the PM4Silt and RSSMC-RH (δ_{rem} = *8 cm*) simulations. PM4Silt is shown to have a higher peak shear stress than the RSSMC model. This difference in peak horizontal stress ratio occurs due to principal stress rotation within the RSSMC elements causing the peak deviatoric stress to occur on a plane that is not horizontal, which is consistent with the results of the strain controlled undrained monotonic DSS driver shown in the calibration section of this manuscript. The PM4Silt model in Figure 3-7b is also shown to fully soften in about 12% shear strain which is consistent with the calibration results. The RSSMC-RH (δ_{rem} = *8 cm*) model shown in Figure 3-7b is shown to fully soften in only 4% SSI which is about 33% faster than observed in the calibration results. The RSSMC-RH (δ_{rem} = *15 cm*) model also softened about 33% faster than observed in the calibration results, although these results are not plotted in Figure 3-7b because it makes the plot difficult to interpret. This may also be due to principal stress rotation and the difference in the way shear strains are calculated in the calibration driver and the field-scale simulations. The maximum shear strain increment as calculated in FLAC 8.0 considers normal strains in the vertical and horizontal directions as well as shear strains in the horizontal direction. Shear strains in the single element DSS drivers are calculated based on lateral shear displacement divided by the height of the element, which is not appropriate for calculating strains in the field-scale simulations due to the more complex deformations that may take place.

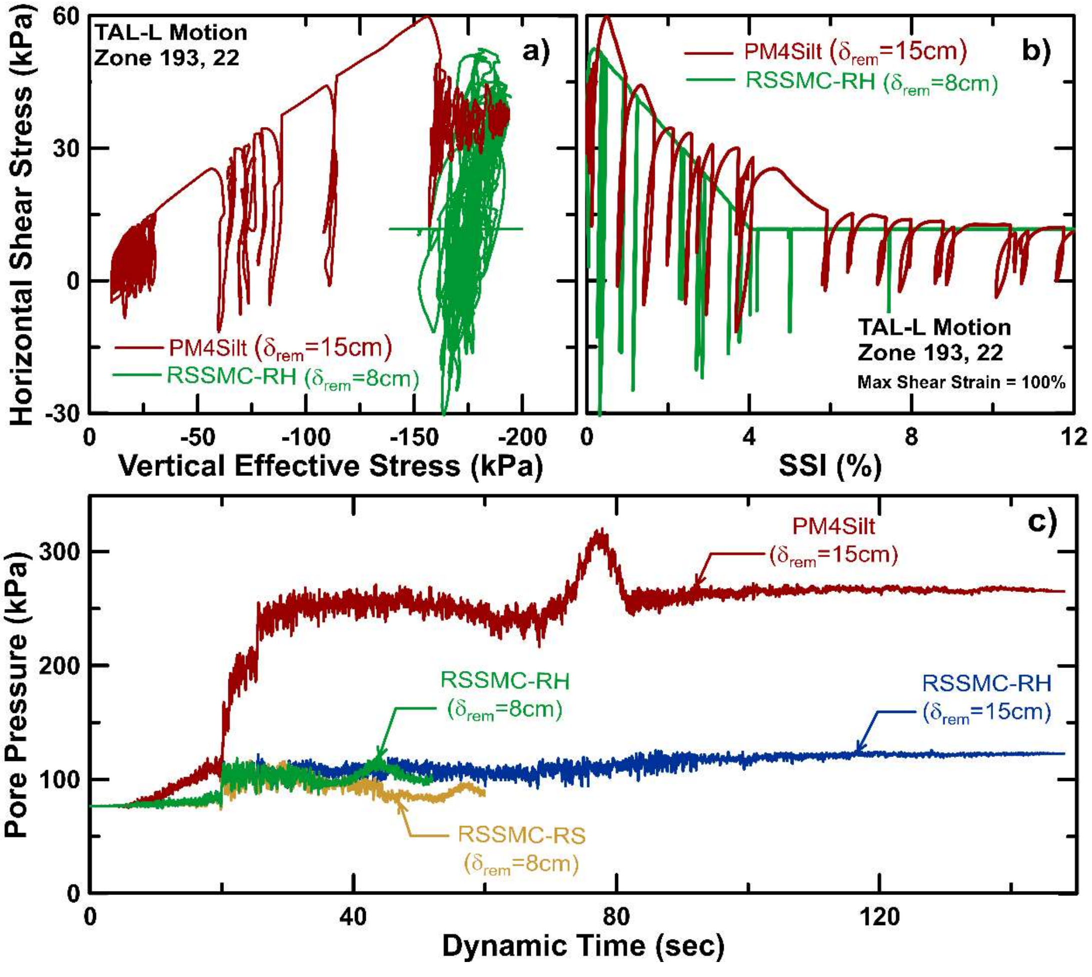

Figure 3- 7: Comparison of element level response of BCC zone (193, 22) along horizontal portion of failure plane for field-scale PM4Silt and RSSMC simulations in terms of (a) stress path, (b) stress strain, and (c) pore pressure generation

3.5.3 Pseudo-spectral Response Spectra

Figure 3-8 shows the pseudo-spectral acceleration response (PSa) at the ground surface (Figures 3-8a, 3-8b, and 3-8c) and at the top of the BCC layer (Figures 3-8d, 3-8e, and 3-8f) in the field-scale model for each model calibration. The 230m location (Figures 3-8a, 3-8d, and 3-8g) corresponds to flat ground behind the upper crest where very little deformation occurred. At 230m no significant difference in the Psa response is observed between the simulations. The 350m location (Figures 3-8b, 3-8e, and 3-8h) corresponds to soil within the major failure mass between the upper and middle slopes. The 470m location (Figures 3-8c, 3-8f, and 3-8d) corresponds to soil within the failure mass near the lower toe of the slope. The PSa response in the failure mass at 350m and 470m shows that PM4Silt provides more material damping than the RSSMC models during failure of the slope. The Psa response of the RSSMC model that only includes stiffness-proportional Rayleigh damping is also shown in Figure 3-8. This model produces larger peak pseudo-spectral accelerations than the other RSSMC models due to the exclusion of additional hysteretic damping. Hysteretic damping produces a more realistic damping response across varying strain levels in space and time compared to Rayleigh damping which only provides an average response (Itasca 2016).

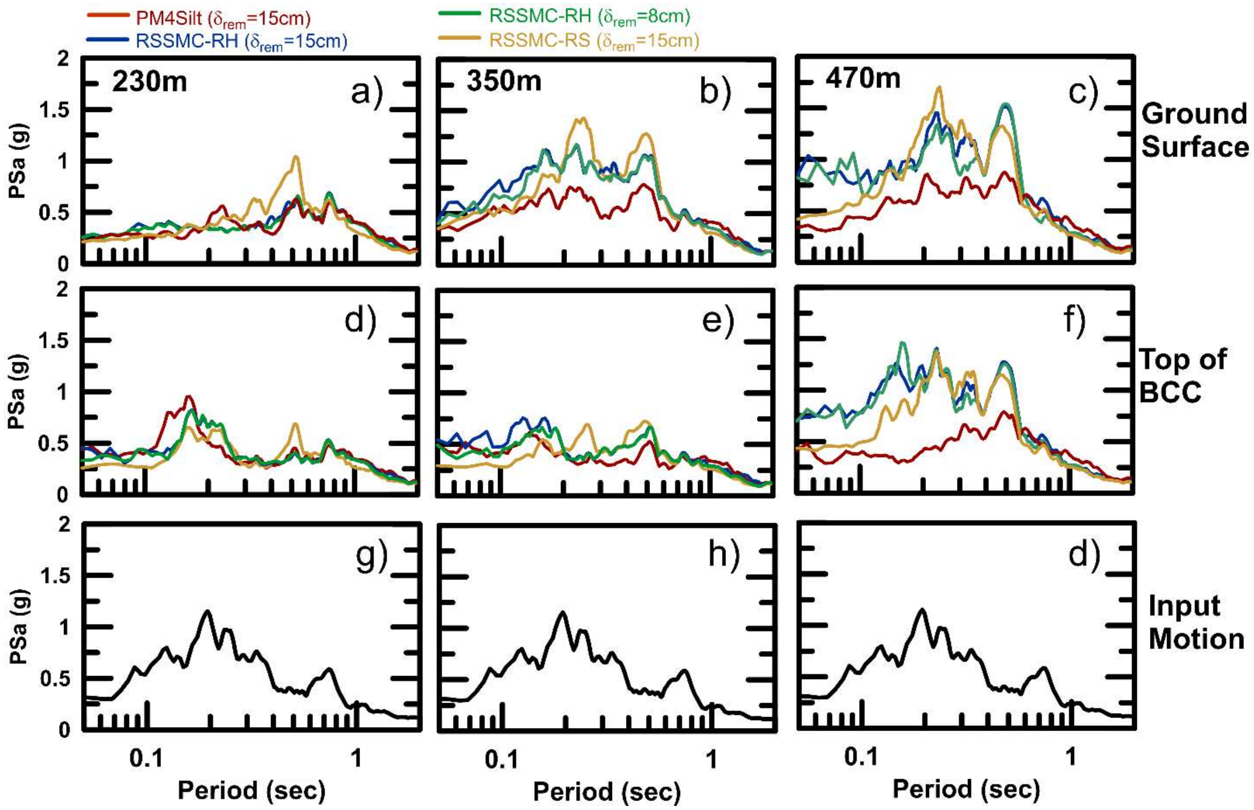

Figure 3- 8: Pseudo-spectral acceleration response spectra for baseline field-scale analysis using TAL-L input motion at three different locations corresponding to behind the crest (230 m), between the upper and middle crest (350 m), and near the toe (470 m)

3.5.4 Effect of Input Motion

Figure 3-9 shows upper crest lateral displacement time histories for different combinations of peak strength, residual strength, and input motion. The effect of input motion can be evaluated by comparing the results from the first (HUA-T), second (CUR-NS) and third (TAL-L) columns in Figure 3-9. Upper crest displacements are shown to increase with input motion intensity. The most intense motion (TAL-L) produces significant ground deformations for the PM4Silt and RSSMC models for all combinations of strength parameters used. The least intense motion (HUA-T) produces minimal upper crest displacement for both models regardless of the strength parameters used. The median intensity motion (CUR-NS) presents a borderline scenario where significant upper crest displacement is only observed for PM4Silt simulations utilizing the lower peak and residual strengths.

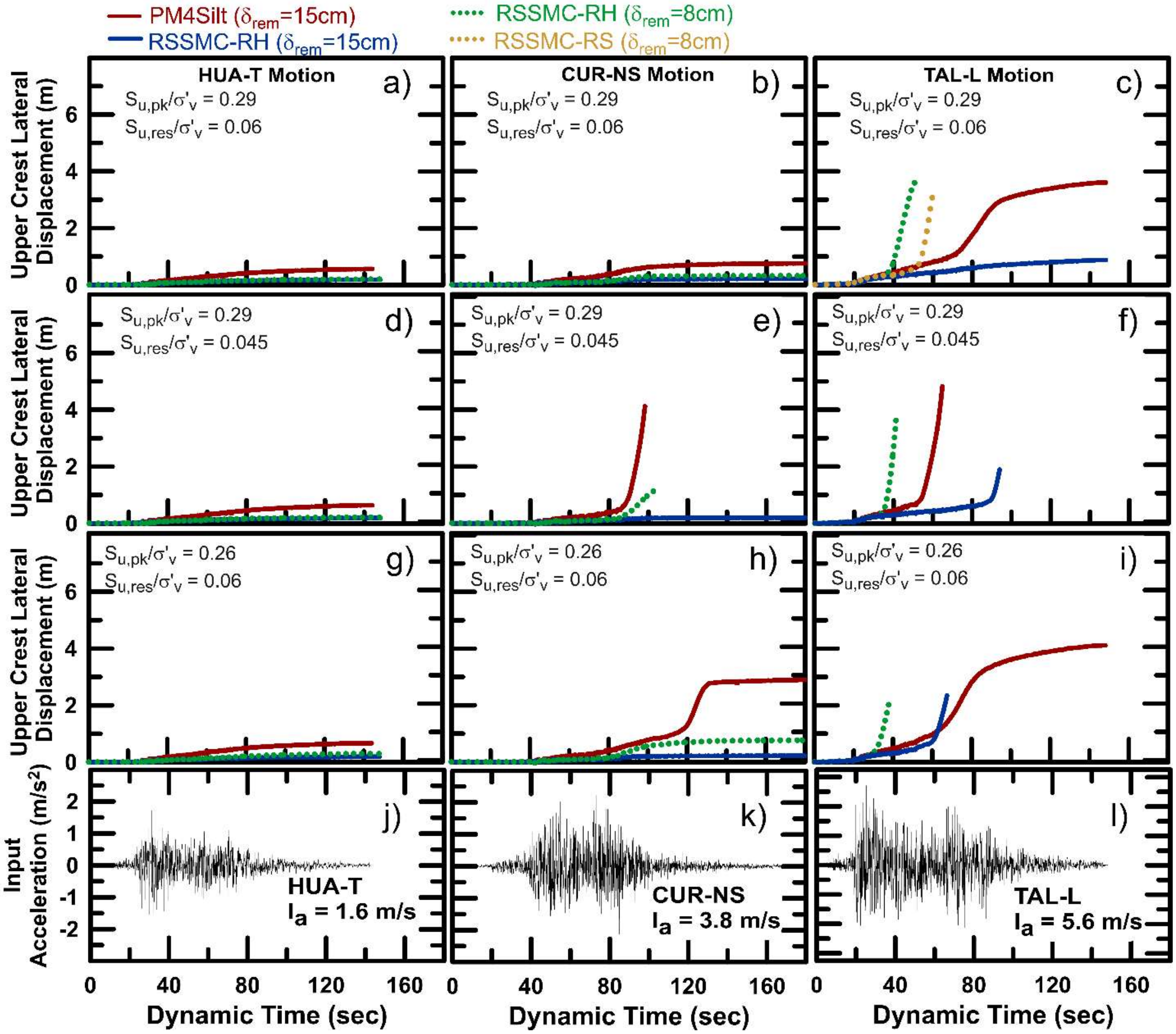

Figure 3- 9: Upper crest displacement time histories using different strength characteristics and input motions for PM4Silt and RSSMC

3.5.5 *Effect of Peak Strength*

The effect of peak strength can be studied by comparing the first row (Figure 3-9 a, b and c) and the third row (Figure 3-9 g, h, and i) in Figure 3-9. Figure 3-9c and 3-9i show that decreasing the peak strength results a small increase in upper crest displacement when the most intense input motion (TAL-L) is used. The median CUR-NS motion using a $S_{u,res}/\sigma'_v$ of 0.06 produces very different displacement magnitudes for $S_{u,pk}/\sigma'_v$ of 0.29 (Figure 3-9b) and 0.26 (Figure 3-9h). The lower peak strength in this case results in significantly larger upper crest displacements compared to the higher peak strength. In this borderline case, the higher peak strength prevented full softening of the BCC zone along the failure plane resulting in minimal ground deformation.

3.5.6 Effect of Residual Strength

The effect of residual strength can be studied by comparing the first row (Figure 3-9 a, b, and c) and third row (Figure 3-9 g, h, and i) with the second row (Figure 3-9 d, e, and f) in Figure 3-9. The final upper crest displacement appears to be more dependent on residual strength if the motion is strong enough to fully soften the BCC. This is illustrated in the TAL-L simulations as the two scenarios with $S_{u,res}/\sigma'_v$ equal to 0.06 produce similar final displacements even though they have different peak strengths while the simulation with the smaller residual strength produces larger deformations. While deformation magnitudes are shown to be more dependent on residual strength, the previous section illustrates that selection of an appropriate peak strength and input motion are also important for borderline cases. The results in Figure 3-9 illustrate that model calibration may not be critical for very weak or strong input motions, but the likelihood of failure may be dependent on these strength characteristics for borderline cases.

3.5.7 Effects of Mesh Density

The effects of mesh density are examined by repeating the baseline analyses using a coarser mesh with BCC element heights of 1.8m and a finer mesh with BCC element heights of 0.9m. The baseline (medium) mesh uses BCC element heights of 1.3m. Input motions and strength characteristics are chosen to best illustrate the effects of mesh density in borderline cases where chosen inputs are more critical to whether failure occurs. The input motions and strength characteristics used for the RSSMC and PM4Silt models are shown in Table 3-1. Field-scale simulations are performed for PM4Silt using a strain-based calibration that matches the stress-strain response for each element height in terms of shear strain in the undrained monotonic DSS calibration driver. The PM4Silt model is also calibrated using a displacement-based approach that matches the stress-displacement response for different element heights in terms of shear displacement as opposed to shear strain. The RSSMC model is calibrated only once using the baseline mesh height of 1.3m to match the steepest portion of the PM4Silt softening curve in terms of shear displacement. Field-scale simulations of the RSSMC model are then performed for each mesh size with and without the softening-scaling regularization technique activated.

Table 3- 1: Strength characteristics and input motions used for PM4Silt and RSSMC in mesh sensitivity study

	PM4Silt		RSSMC	
Input Motion	CUR-NS	TAL-L	CUR-NS	TAL-L
$S_{u,pk}/\sigma'_v$	0.26	0.29	0.26	0.29
$S_{u,res}/\sigma'_v$	0.06	0.06	0.06	0.06
δ_{rem}	15 cm	15 cm	8 cm	8 cm

The effect of mesh size dependence for the PM4Silt model is shown in Figure 3-10a and 3-10b using the strain-based calibration. Figure 3-10a shows upper crest displacements to increase with decreasing mesh size when the median (CUR-NS) motion is used. The fine and medium meshes produce upper crest displacements of 4 m and 3 m respectively, while the coarse mesh produces an upper crest displacement of 1.5m. The effect of using the displacement-based calibration with PM4Silt for the CUR-NS motion is shown in Figure 3-10e. The PM4Silt model using the displacement-based calibration produces final upper crest displacements of about 3m for both the medium and coarse mesh for the CUR-NS simulations, but the upper crest begins to move earlier in the motion for the coarse mesh. The fine mesh for PM4Silt in the CUR-NS simulations is halted early due to geometry errors but follows a similar displacement path compared to the medium mesh for the displacement-based calibration (Figure 3-10e).

Figure 3-10b shows upper crest displacements also increase with decreasing mesh size for PM4Silt when the most intense (TAL-L) motion is used. The medium and coarse meshes each produce a final upper crest displacement of about 3.5 m. The upper crest displacement for the fine mesh is at about 5.5m when the simulation is halted early due to geometry errors. The effect of using the displacement-based calibration with PM4Silt for the TAL-L motion is shown in Figure 3-10f. The displacement-based calibration causes the upper crest displacement for the fine mesh to more closely match the medium mesh. Upper crest displacements for coarse mesh are increased to 5 m when the displacement-based calibration is used, but the results for each mesh size are in better agreement compared to using the strain-based calibration.

The effect of mesh size dependence for the RSSMC model is shown in Figure 3-10c and 3-10d where the softening-scaling regularization technique is not used. Figure 3-10c shows the fine mesh to produce a slightly higher upper crest displacement (1.2 m) than the medium (0.7 m) and coarse meshes (0.6 m). The softening-scaling regularization causes the upper crest displacement of the fine mesh to better match the medium mesh, while upper crest displacements for the coarse mesh begin earlier in the motion and reach a slightly higher final displacement of 1.2 m. The effect of mesh density for the RSSMC model is better illustrated using the more intense (TAL-L) motion (Figure 3-10c). The fine and medium meshes without regularization each produce large upper crest displacement values earlier in the motion and are halted early due to geometry errors. The coarse mesh results in a final upper crest displacement of only 1.3 m as the larger element size prevents full- softening of BCC zones along the failure plane when the regularization technique is not used. The softening-scaling regularization is shown to reduce mesh size dependence for the TAL-L motion in Figure 3-10h. Upper crest displacements begin earlier in the motion for each mesh size and all three simulations are halted early due to geometry errors. Upper crest displacements are shown to begin earlier for the coarse mesh when the regularization is implemented which is consistent with the RSSMC results for the CUR-NS motion (Figure 3-10g) and the PM4Silt simulations utilizing the displacement-based calibration (Figure 3-10e and 3-10f).

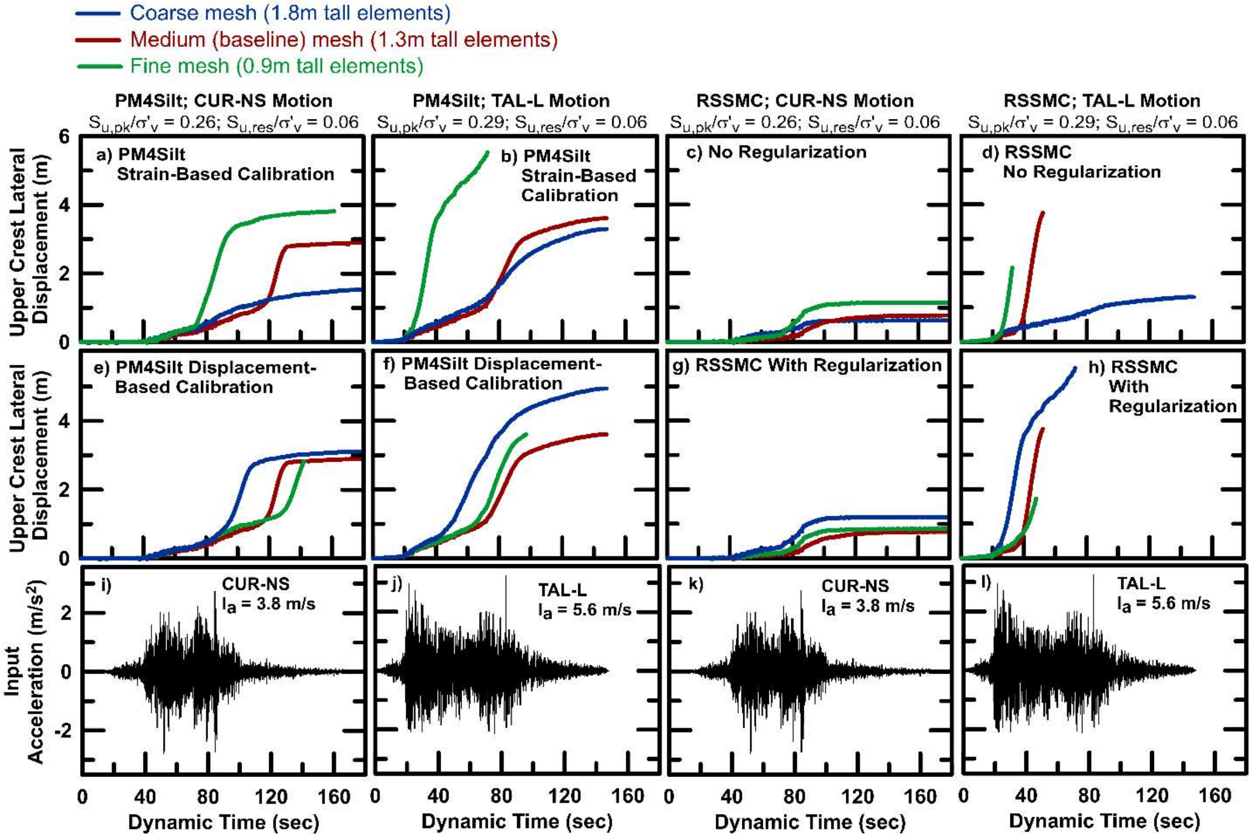

Figure 3- 10: Effects of mesh density on upper crest lateral displacement for PM4Silt and RSSMC for two sets of strength characteristics and input motions

Figure 3-11 shows PM4Silt maximum shear strain increment contours or each mesh size using the displacement-based calibration and the CUR-NS motion. The failure plane in the fine mesh remains shallow between the middle and upper crests. The failure plane in the fine mesh actually remains at the top of the saturated BCC zones and becomes deeper as the water table elevation decreases near the toe of the slope. The failure plane for the coarse and medium mesh transitions to the bottom of the BCC layer immediately after encountering unsaturated BCC zones where the water table elevation begins to decrease. The failure plane in the medium mesh is more well defined than the coarse mesh but is quickly forced to the bottom of the BCC layer.

Figure 3-12 shows RSSMC maximum shear strain increment contours or each mesh size using the TAL-L motion and the softening-scaling regularization technique. The failure plane in the fine mesh remains deep except for near the toe of the slope. The failure pane in the coarse mesh becomes shallow just past the middle crest and quickly becomes deep again as it encounters the unsaturated BCC zones. The failure plane in the medium mesh is more well-defined than the coarse mesh but becomes shallow past the middle crest and remains shallow towards the toe of the slope.

It is apparent from Figures 3-11 and 3-12 that the regularization techniques for the RSSMC and PM4Silt models do not eliminate mesh dependence even though the upper crest displacement paths are in better agreement for each mesh size. Each of the PM4Silt (Figure 3-11) and regularized RSSMC (Figure 3-12) simulations in the mesh density study produced a deep failure plane beneath the upper crest, which turned upward near the middle crest. The chosen mesh size appears to have an influence on how the deeper failure mass beneath the upper crest interacts with the shallow failure mass beyond the middle crest.

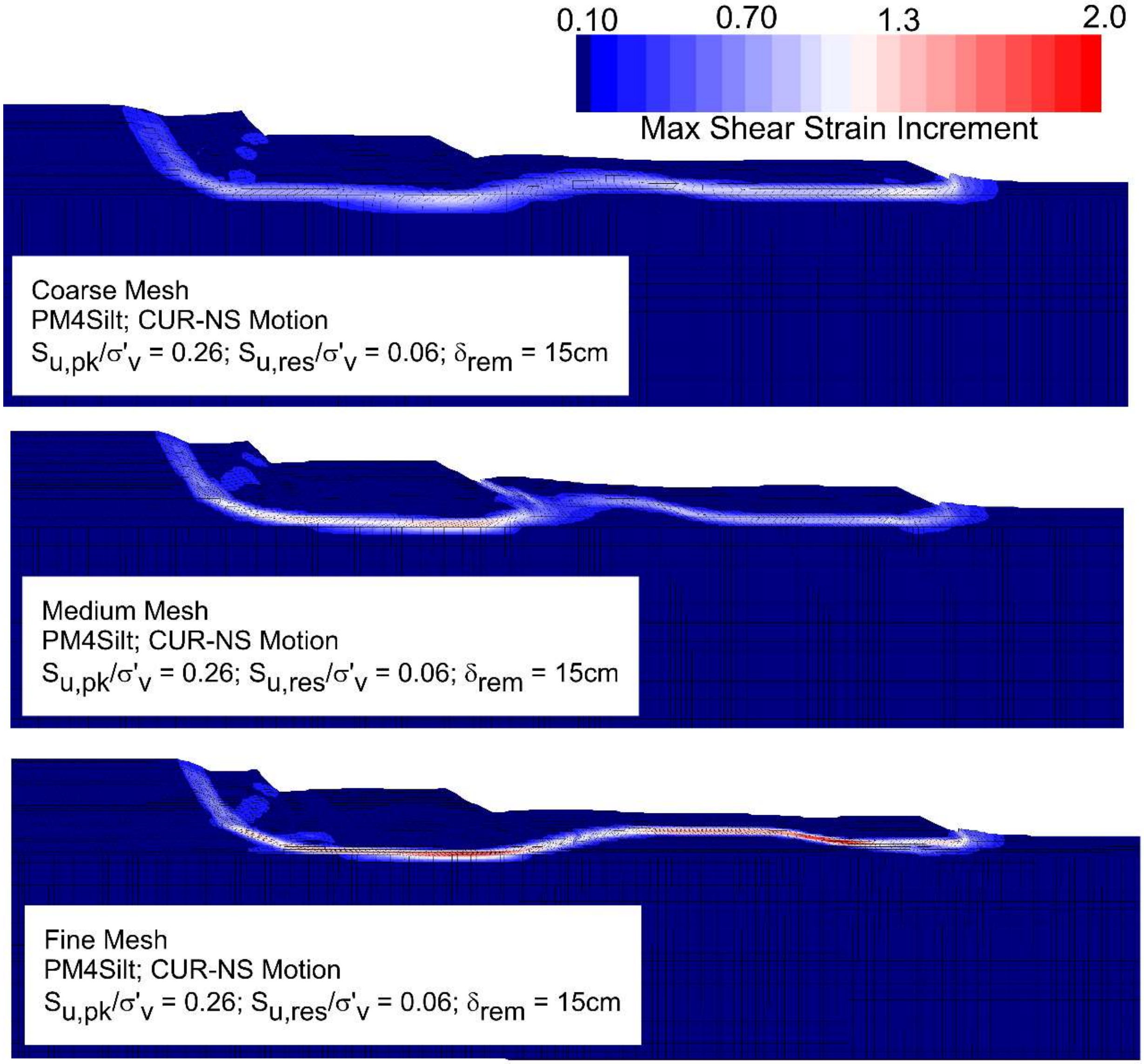

Figure 3- 11: Maximum shear strain increment for coarse (upper), medium (middle) and fine (lower) mesh using PM4Silt with the displacement-based calibration procedure and CUR-NS motion

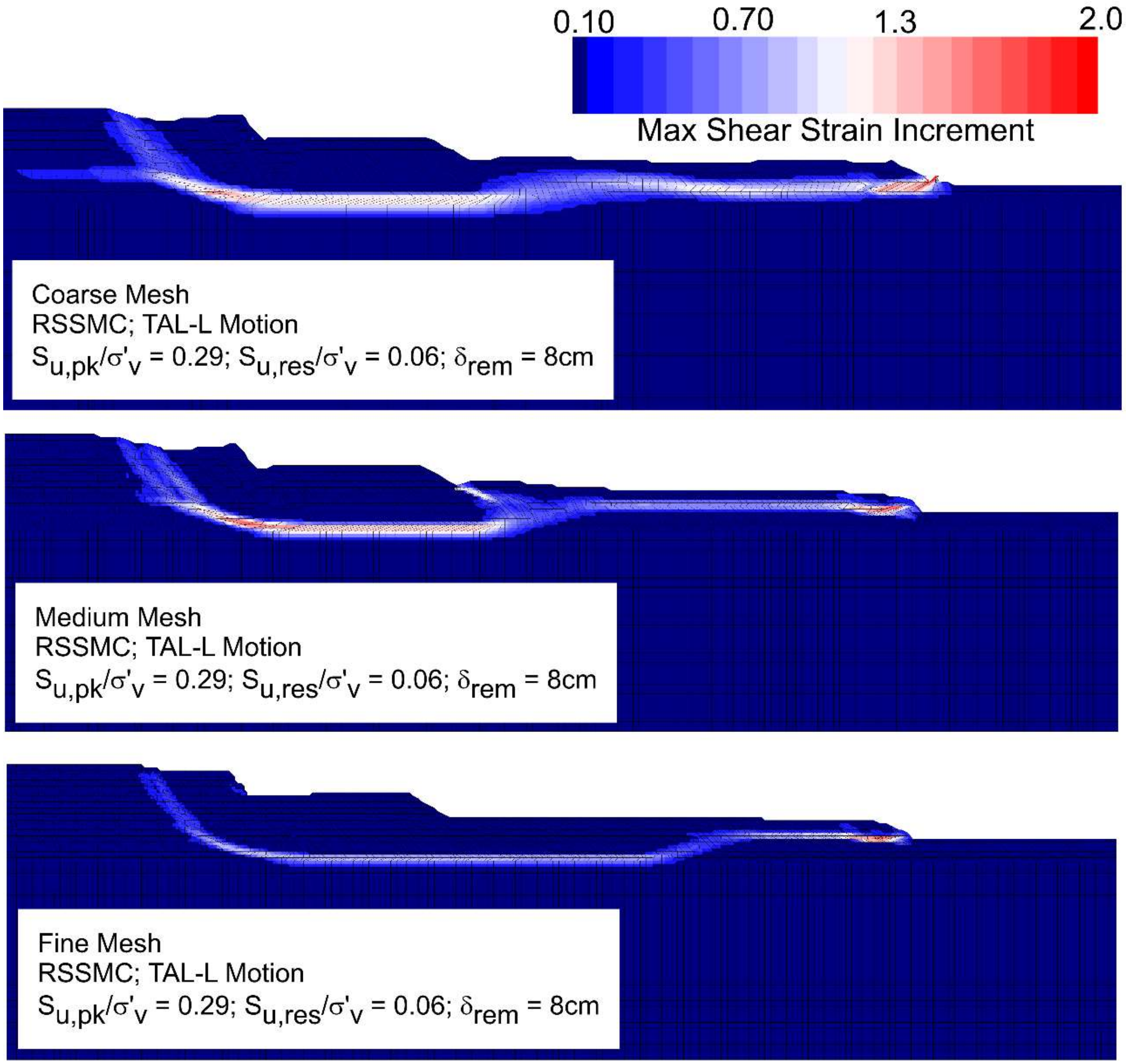

Figure 3- 12: Maximum shear strain increment for coarse (upper), medium (middle) and fine (lower) mesh using RSSMC model with the softening-scaling regularization technique and the TAL-L motion

Figure 3-13 shows crest displacement time histories at different locations for each mesh size using PM4Silt with the displacement-based calibration and RSSMC for the CUR-NS motion. The borderline scenario for PM4Silt that best illustrates the effect of mesh size is shown in Figures 3-13a-c for the CUR-NS motion. Figure 3-13a and 3-13c show similar behavior with displacments beginning at the lower crest, followed by the middle crest and then the upper crest for the coarse and fine meshes, respectively. Failure in the medium mesh with PM4Silt begins in a similar fashion except displacement of the lower crest proceeds slower allowing larger displacement from the middle crest (Figure 3-13b). At about 120 seconds, displacement from the middle crest exceeds that of the lower crest. At this time, the deeper failure mass slides into the shallow failure mass resulting in a spike in pore pressure in the failure zone for the medium mesh. Progression of the PM4Silt failure using the more intense TAL-L motion (Figure 3-14a-c) is more consistent for each mesh size with the largest displacements occuring at the lower crest and the smallest displacements at the upper crest.

Figure 3-14 shows crest displacement time histories for each mesh size using PM4Silt with the displacement-based calibration and RSSMC for the TAL-L motion. The borderline scenario for RSSMC that best illustrates the effect of mesh size is shown in Figures 3-14g-i for the TAL-L motion. The borderline scenario for RSSMC shows differences in model behavior that are similar to the borderline scenario for PM4Silt. Figure 3-13g and 3-13i show similar behavior with displacments beginning at the lower crest, followed by the middle crest and then the upper crest for the coarse and fine mesh, respectively. Failure in the RSSMC medium mesh begins in a similar fashion except displacement of the lower crest proceeds slower (Figure 3-13h). At about 40 seconds displacement from the middle crest exceeds that of the lower crest. At this time the deeper failure mass slides into the shallow failure mass and the middle crest displcament exceeds that of the lower crest. Progression of the RSSMC failure using the median intensity CUR-NS motion (Figure 3-13g-i) is more consistent for each mesh size with the largest displacements occuring at the lower crest and the smallest displacements at the upper crest.

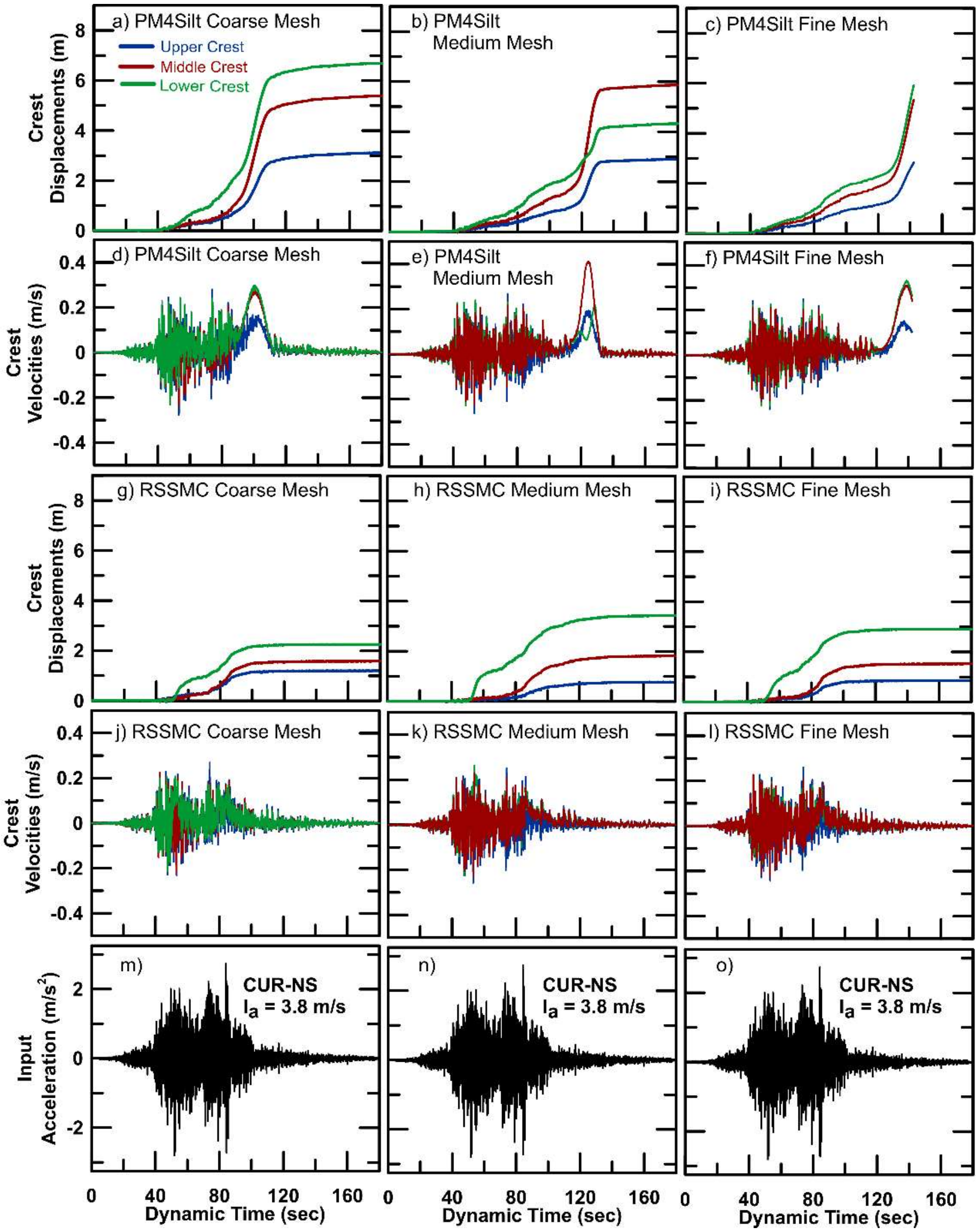

Figure 3- 13: Time histories of crest displacement and velocities for different mesh sizes using CUR-NS motion, PM4Silt with displacement-based calibration, and RSSMC with regularization

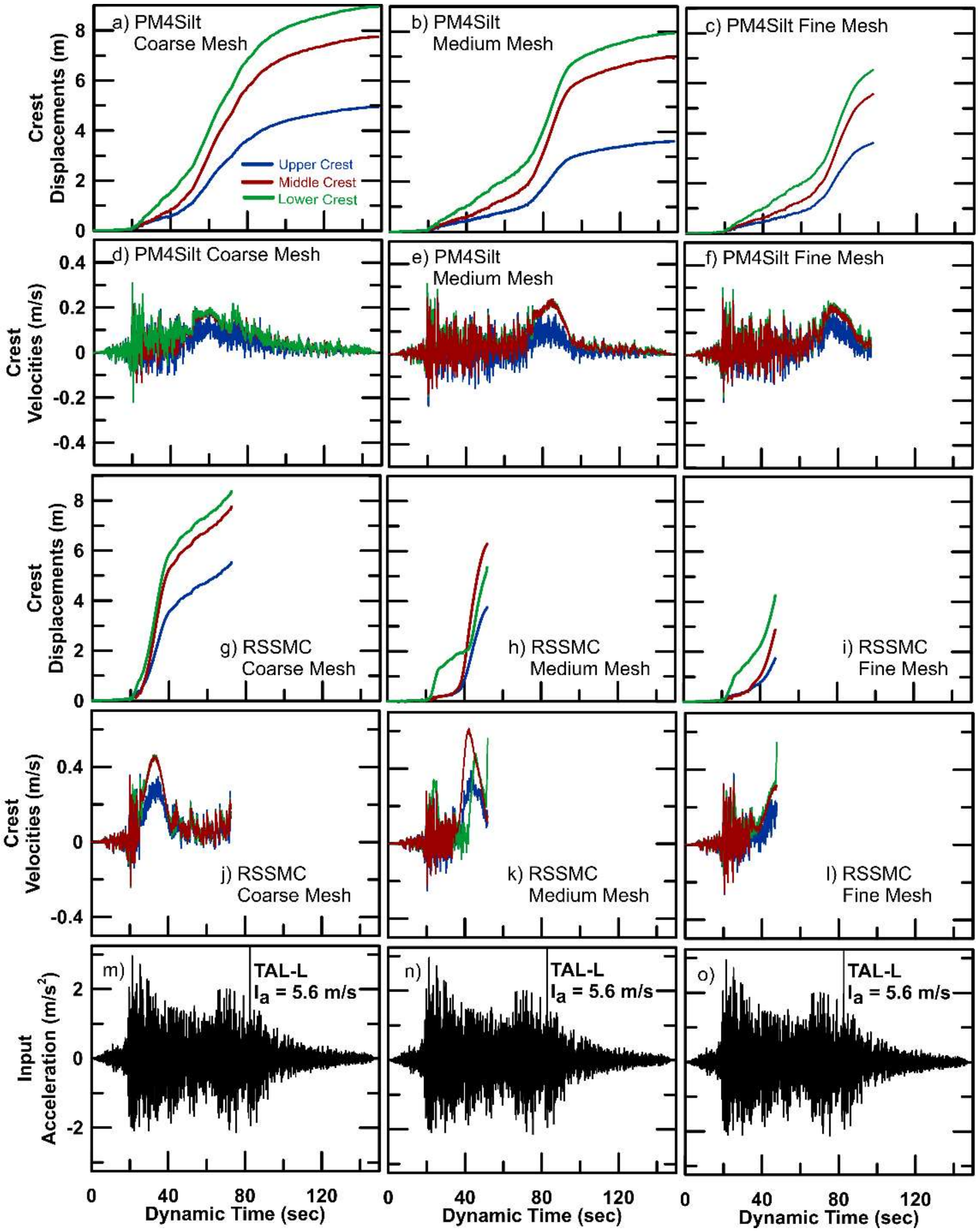

Figure 3- 14: Time histories of crest displacement and velocities for different mesh sizes using TAL-L motion, PM4Silt with displacement-based calibration, and RSSMC with regularization

The results from Figures 3-13 and 3-14 show the displacement-based calibration procedure (PM4Silt) and the softening-scaling regularization technique (RSSMC) can reduce mesh size dependence in terms of upper crest displacment. However, mesh size is still shown to influence the failure mechanism and location of the failure plane and this effect is most pronounced for the borderline scenarios. Chapter 2 has shown that residual strength is the primary factor influencing final upper crest displacement if loading is sufficient to fully soften the BCC. This means that the final upper crest displacement may be relatively independent of mesh size if full softening is achieved, but the failure patterns may be different, as shown in these results. The regularization techniques used in this study only address one aspect of mesh dependency by allowing different element sizes to fully soften under similar deformation magnitudes. These regularization techniques do not account for other aspects of mesh dependence such as resolution of the failure plane, varying strengths with zone size, the exact location of the water table, or strain dependent model behavior such as modulus reduction and material damping. These differences alone may not seem significant, but can result in mesh dependent behavior for borderline cases such as those used in the mesh sensitivity study.

3.6 DISCUSSION

The single element DSS drivers illustrate the ability of the PM4Silt and RSSMC models to reproduce important aspects of strain-softening at the element level under controlled loading conditions. PM4Silt is able to model the nonlinear stress strain behavior which converges toward the residual strength at large strain magnitudes under monotonic loading as observed in previous lab tests on strain-softening clays (e.g., Burland 1990, Stark and Contreras 1998, Gylland et al. 2014). The RSSMC models conversely show a more linear stress strain relationship that reaches the residual strength at a distinct magnitude of shear displacement (Figure 3-1). The linear stress-displacement relationships inherent in the RSSMC models can make calibrations more difficult due to the uncertainty in selecting an appropriate value of δ_{rem} even if lab data is available to help estimate the softening rate. The user is forced to decide whether to set δ_{rem} for the RSSMC models as the value where the soil fully softens in a lab test or to try to match the stress-displacement curve from the lab test that will cause the soil to fully soften at some magnitude of shear displacement between the where the peak and residual strengths are observed. This study found that matching the initial portion of the stress-strain curve for the RSSMC model is necessary to produce deformations consistent with site observations and large deformations are only observed using the most intense input motion. This limitation narrows the boundary between failure and a stable slope making sensitivity studies involving strength characteristics and input motions even more critical for RSSMC compared to PM4Silt.

Clays under dynamic loading have been observed to exhibit shear modulus reduction and an increase in material damping as cyclic shear strain magnitudes increase (e.g., Vucetic and Dobry 1987). PM4Silt includes small strain damping and can be calibrated to match modulus reduction and damping behavior by adjusting the model parameter h_0. The RSSMC model requires that additional hysteretic and Rayleigh damping to be included in order to capture damping during elastic loading. The RSSMC-RH and PM4Silt models are able to match the curves provided by Vucetic and Dobry (1987) comparatively well (Figure 3-2). Failing to include hysteretic damping with RSSMC resulted in the model being overly stiff at small strains (Figure 3-2) and slightly delayed the onset of large displacements in field-scale simulations (Figure 3-4). Failing to exclude the mass-proportional term from Rayleigh damping with RSSMC suppressed yielding in the BCC resulting in little lateral displacement in field-scale simulations (Figure 3-4). These examples illustrate the importance of calibrating constitutive models to appropriate modulus and damping response in situations involving dynamic loading of strain-softening clays. More advanced models (e.g., PM4Silt) may include model parameters for the purpose of calibrating to modulus reduction and damping response. Simpler constitutive models (e.g., RSSMC) may require additional hysteretic and stiffness-proportional Rayleigh damping to accurately represent stiffness and damping behavior under cyclic loading.

Soft, saturated clays have been observed to experience significant pore pressure generation during undrained loading resulting in a reduction in effective stress and loss of shear resistance (Gylland et al. 2014). The effective stress-based PM4silt model is able to represent the influence of changes in effective stress on material response (Figure 3-3) as observed in tests on soft clays (Hyodo et al. 1999, Gylland et al. 2014, Thakur et al. 2017). Significant pore pressure generation is observed in field-scale PM4Silt simulations for BCC zones within the failure plane resulting in a reduction in effective stress and loss of shear resistance (Figure 3-8). RSSMC does not consider volume change due to shearing resulting in minimal pore pressure generation in the failure plane. The RSSMC model is also based on a total stress analysis, so the peak strength remains at a fixed value prior to softening and the peak strength is not affected by changes in effective stress. These results show that the total stress-based RSSMC model fails to capture some important aspects of soil behavior. Effective stress-based models (e.g., PM4Silt) are therefore more appropriate for situations where a detailed understanding of element level response is important for the problem being analyzed.

Field-scale simulations of the Fourth Avenue landslide demonstrate the ability of each model to reproduce the overall deformation patterns and magnitudes given the right combination of properties and input motion. RSSMC exhibited a more brittle response with large displacements generally occurring abruptly or not at all. A more ductile response is observed for PM4Silt simulations with deformation magnitudes increasing more gradually as softening progressed.

The RSSMC model produced reasonable deformation patterns within the major failure mass but almost no deformation is observed outside of the failure mass. PM4Silt produced reasonable deformation patterns inside the failure mass as well as minor deformations outside of the failure mass which is more consistent with site observations. These more detailed deformation patterns are prevalent in simulations using the most intense input motion (TAL-L) which is thought to best represent the intensity of the long duration Great Alaska Earthquake. The results of this study indicate that advanced models (e.g., PM4Silt) are more appropriate for cases where an estimation of deformations outside of the major failure mass is important or if there is a need to understand the progression of ground displacements. Total stress-based models (e.g., RSSMC) may be adequate for scenarios where the engineer is primarily interested in whether or not failure will occur, but sensitivity studies examining the effect of input parameters is more critical as the boundary between failure and a stable slope may be narrow compared to more advanced effective stress-based models.

Field-scale simulations are also run with different element sizes to examine mesh dependence in each model and evaluate the ability of displacement-based calibrations to reduce mesh size dependence in PM4Silt. The softening-scaling regularization technique implemented with the RSSMC model is shown to reduce the effect of mesh size dependence on observed upper crest displacements compared to simulations where the regularization technique is disabled. The displacement-based calibration procedure is shown to reduce mesh dependency of the PM4Silt solution compared to a traditional strain-based calibration. The displacement-based calibration allows BCC elements of different heights to fully soften under similar displacement magnitudes, but does not eliminate other aspects of mesh size dependence. Mesh size is still shown to influence the resolution and shape of the failure surface which affected interaction between the deeper failure mass beneath the upper crest and the shallow failure mass beyond the middle crest. The critical failure surface between the middle and lower crests generally occurs at either the top or bottom zones of the BCC layer depending on the strength characteristics and input motion intensity. The failure plane beyond the middle crest for the fine mesh remained at the top of the saturated BCC zones. The failure plane beyond the middle crest in the coarse and medium mesh is forced to the bottom of the BCC layer immediately upon encountering unsaturated zones.

Mesh dependency has been shown to be reduced when element sizes approach the thickness of the localized failure plane (Thakur 2007, Zabolotnii et al. 2021). This suggests that the finer meshes may produce the most reliable results. However, shear band thickness in clays has been observed to be on the order of micrometers to a few centimeters (Thakur et al. 2006). The fine mesh in this study used BCC element heights of 0.9m which is significantly larger than the expected shear band thickness. The fine mesh is more susceptible to geometry errors at lower deformation magnitudes and the field-scale simulation took much longer to run (about 48 hours) compared to the medium (about 18 hours) and coarse (about 8 hours) compared to the other mesh sizes using an Intel® Xeon® E5-1600 CPU with eight 3.00 GHz cores and 32 GB RAM. Further reduction in element size for this case history is therefore not feasible due to incomplete results and the large increase in computation time. The regularization techniques in this chapter have focused on scaling softening response based on displacement magnitude. This research has shown that softening response is not the only factor influencing mesh dependency. Further work is required to investigate other aspects of mesh dependency so that element heights much larger than the shear band thickness may be used to accurately represent strain-softening and localization in field-scale simulations.

Alternative modeling techniques that overcome limitations regarding geometry errors under large deformation have recently been used in analyses involving landslides. These approaches include interface elements (e.g., Jostad and Andersen 2004), material point method (e.g., Soga et al. 2016) and mixed Langrangian-Eulerian approaches (e.g., Moug et al. 2019). Soga et al. (2016) provides a detailed description of each technique, including discussion of benefits and limitations. These techniques can reduce errors related to excessive mesh distortion, which may halt simulations prematurely. Previous research involving these alternative modeling techniques have mainly involved static problems and/or comparatively simple elastoplastic constitutive models. Further research is needed to advance and validate these methods for analyses concerning pore-fluid coupling and cyclic loading of strain-softening clays. The results in this study may provide a comparison for future research.

3.7 SUMMARY AND CONCLUSIONS

This chapter compares the ability of a simple total stress-based model (RSSMC) and a more advanced effective stress-based model (PM4Silt) to represent cyclic softening of clay. Single element DSS drivers are used to examine each model's response under controlled loading. Field-scale simulations are also performed to examine the ability of each model to reproduce deformation patterns and magnitudes observed at the Fourth Avenue site. The results from the field-scale simulations are compared in terms of displacements, acceleration response spectra, and element behavior in order to understand the effects of the constitutive model on the response.

PM4Silt produces a more realistic nonlinear stress-displacement curve in element-scale simulations of undrained monotonic loading. RSSMC produced a piecewise linear representation of stress and displacement which made it difficult to accurately match nonlinear stress-displacement curves observed in strain-softening clays. Calibrating RSSMC to match the steepest portion of the softening curve is required to reproduce the observed large displacements in the field-scale simulations. PM4Silt is shown to be influenced by changes in effective stress due to excess pore pressure generation in single element simulations (Figure 3-3a). Almost no variation in effective stress occurs using the RSSMC model (Figure 3-3a) in single element simulations because no dilatancy is incorporated in the RSSMC model and so no excess pore pressures are generated in these undrained simulations. Both models are able to reasonably match modulus reduction and damping ratio curves in the calibration drivers, but RSSMC required additional hysteretic damping. Failure to include appropriate damping with the RSSMC model in the field-scale simulations results in delayed softening (no hysteretic damping) or suppressed yielding of BCC in the failure zone (mass-proportional Rayleigh damping included).

The effective stress-based PM4Silt model demonstrates generation of excess pore pressure and changes in effective stress and strength in the field-scale simulations. RSSMC does not consider volume change due to shearing resulting in minimal pore pressure generation in the failure plane. The RSSMC model is also based on a total stress analysis, so the peak strength remains at a fixed value prior to softening and is not affected by changes in effective stress. PM4Silt is also shown to provide more damping in the failure mass in field-scale simulations compared to the RSSMC model. Both models produce reasonable deformation patterns and magnitudes within the Fourth Avenue failure mass, but PM4Silt produces small deformations outside of the failure mass as is observed in the field. RSSMC displays almost zero ground displacement outside of the primary failure mass.

This chapter also examines the ability of the displacement-based calibrations to reduce mesh dependency of the PM4Silt solution. The displacement-based calibration is shown to produce consistent upper crest displacement magnitudes using different mesh sizes, but previous research suggests that final displacement magnitudes are primarily dependent on residual strength (Chapter 2). The displacement-based calibration allows BCC elements of different heights to fully soften under similar displacement magnitudes, but does not eliminate other aspects of mesh density including location of the failure plane and the progression of failure. Practicing engineers may use the displacement-based calibration approach to reduce mesh dependency in simulations involving strain-softening clays, but should be aware that other aspects of mesh dependence may still exist. Additional research is needed to address additional aspects of mesh dependency and limitations involving large deformation geometry errors.

One main goal of this chapter is to provide guidance as to when it may be necessary to use more advanced effective stress-based models (e.g., PM4Silt) versus simple total stress-based models (e.g., RSSMC). The results in this study suggest that advanced effective stress-based models may be necessary if element level response or a more complete estimation of ground deformation patterns both inside and outside of the failure mass are important to the scenario being modeled. Simple total stress-based models may be adequate if the user is primarily interested in whether or not failure will occur. Total stress-based models are often described as easier to calibrate, but this study showed that calibration to modulus reduction and damping behavior to be more tedious for the RSSMC model and have a significant influence on field-scale results. The brittle failure modes observed with RSSMC shows that sensitivity studies to examine the effect of chosen strength and softening parameters are more critical for the RSSMC model.

CHAPTER 4: CHARACTERIZATION AND ANALYSIS OF A SLOW-MOVING LANDSLIDE IN STRAIN-SOFTENING CLAY

This chapter is based on a paper in preparation for submission to *Engineering Geology.*

Kiernan, M., Xuan, M., Montgomery, J., Anderson, J.B., McDonald, B. (2021). “Characterization and Analysis of a Slow-moving Landslide in Strain-softening Clay. Manuscript under preparation.

This chapter is altered from the version to be submitted to the *Engineering Geology* to minimize repetition and maintain a logical organization of content. My primary contributions to the chapter included: (i) collection and processing of electrical resistivity data (ii) evaluation of available geotechnical testing results and selection of soil parameters, (iii) literature review, (iv) design and implementation landslides analyses, (v) processing, analyzing, and interpretation of the results, and (vi) preparation of initial draft and most of subsequent writing.

4.1 INTRODUCTION

The previous chapters examined undrained cyclic loading of strain-softening clays. Slope failures on roadway embankments under static loading are also common and lead to traffic disruption and repeated repair costs (Wright et al. 2009). Detailed characterization of these landslide sites is key to building accurate site models for slope stability analyses. Traditional geotechnical explorations provide data only at discrete points, but geophysical methods offer a means to supplement geotechnical data and can provide continuous 2D profiles (e.g., electrical resistivity imaging) or 1D shear wave velocity profiles (e.g., multi-channel analysis of surface waves) to help estimate site stratigraphy and identify features associated with the failure (e.g., Jongmans and Garambois 2007, Perrone et al. 2014). Selection and representation of strength characteristics for such failures can also be difficult due to uncertainty in selecting appropriate drained (e.g., Skempton 1970, Wright et al. 2009) and undrained peak strengths and proper representation of nonlinear drained failure envelopes (e.g., Stark et al. 2005). Limit equilibrium method (LEM) analysis software typically includes a power curve option for representing nonlinear strength envelopes (e.g., Rocscience 2021) but constitutive model options for strength reduction method (SRM) analyses to represent this nonlinearity in soils are comparatively limited (VandenBerge and McGuire 2019).

The chapter focuses on the characterization and analysis of landslide site underlain by a strain-softening clay in which repeated failures are observed with relatively small movements. The characterization is performed by integrating results from electrical resistivity imaging (ERI) and multi-channel analysis of surface waves (MASW) with traditional geotechnical explorations to develop a representative cross-section for the landslide and ring shear results to measure the drained fully softened and residual strengths of the critical zone.

The failure mass at the site used in this study is expected to involve soft clayey soils suggesting that the failure mass will have a lower resistivity (e.g., Perrone et al. 2014) and shear wave velocity (e.g., Jongmans and Garambois 2007) than the surrounding soils. The results from the site characterization are used to create a site model to be used for slope stability analyses. Ring shear testing is used to estimate drained fully softened and residual shear strength envelopes. The drained shear strength envelopes from ring shear testing are found to be nonlinear. Peak undrained shear strength is estimated using values in published literature.

Extensive research has focused on methods to represent nonlinear shear strength envelopes of soils (e.g., Baker 2004, Atkinson 2007, VandenBerge et al. 2018). The nonlinear drained strength envelopes observed in ring testing are represented using a power curve in limit equilibrium method (LEM) analyses and the Modified Hoek-Brown (MHB) constitutive model in strength reduction method (SRM) analyses. Power curve relationships have been extensively used to represent nonlinear strength envelopes of clays in LEM analyses (e.g., Perry 1994, Jiang et al. 2003, Wu et al. 2021). The MHB model provides a nonlinear strength envelope, which is similar in form to the relationship presented by Jiang et al. (2003), but MHB is formulated for use with rocks. This study examines the ability of the MHB model to represent nonlinear drained strength envelopes for clay in SRM and associated FS values are compared to results from LEM analyses using power curve functions. FS values using MHB in SRM analyses are found to compare well with FS values obtained from LEM analyses using power curves. The MHB model therefore seems to be a practical tool for representing nonlinear drained strength envelopes in SRM analyses involving clays.

Limit equilibrium analyses are performed using circular and noncircular failure surfaces in SLIDE2. SRM analyses are performed using the commercial finite difference software FLAC V8.0. FS values from LEM analyses are shown to be higher when circular surfaces are used compared to noncircular surfaces. FS values from SRM analyses compare well with LEM results using noncircular surfaces. Initial failure of the slope is investigated using fully softened drained shear strength envelopes and peak undrained shear strength ratios. Continued movement on the slope is examined using the drained residual shear strength envelope. Results from each analysis method are compared. A limited sensitivity study is also performed to examine the effect chosen model parameters on slope stability.

The main objective of this chapter is to understand the failure mechanism for this landslide. Results from slope stability analyses indicate the slope would be stable using fully softened strengths, but unstable when considering undrained strengths. This indicates that initial failure of the slope likely occurred under undrained loading, possibly during initial construction of the embankment. Analyses utilizing the residual drained strength envelopes produce FS values significantly lower than 1 indicating the slope is unstable when soil on the failure plane reaches the residual state. Sensitivity studies indicates that the slope may become stable due to lowering of the water table or recovery of the strength on the failure plane. These results suggest that the intermittent nature of movements at the site is likely related to changes in the water table leading to periods of strength gain followed by reactivation when the water table rises.

4.2 SITE DESCRIPTION

This project site is located along I-65 in Conecuh County, Alabama. This section of the interstate consists of a 2 m meter thick compacted fill embankment overlying the native soils, that consist primarily of high plasticity clay. The embankment has an average slope angle of 11.7°. The slope angle near the top of the embankment is about 13.8° and the slope angle near the bottom is about 8.6°. Persistent cracking has occurred along the southbound shoulder of the roadway over a length of approximately 63 m. ALDOT personnel indicated that pavement cracking at the site has been observed as early as 2007. Google Earth images of this location show cracking as far back as 1998 and older Google Earth images make it difficult to determine the presence of cracking due to poor image resolution. It is possible that the initial failure occurred during or after the initial construction of the embankment, which was likely completed in the 1960's or early 1970's. Figure 4-1 shows a map of the site and contains locations of pavement cracking, resistivity lines, seismic line, total station, and borings.

A slow-moving landslide is located along the southbound shoulder within the roadway embankment. The initial cause of the landslide is unknown but is likely attributed to elevated water table elevations due to high intensity or long duration rain events. High intensity rainfall events of shorter duration may not raise the water table significantly if a low permeability layer exists beneath the surface (Tang et al. 2020). This occurs because the rate of water infiltration is limited by the low permeability. These cases can produce perched water tables and a loss of matric suction leading to shallow slope failures (Cho 2009). Cracks, such as those that may occur near the scarp of a landslide, may allow this perched water to more quickly reach deeper layers. Analyzing a perched water table condition requires advanced numerical techniques that can model transient seepage and two-phase flow associated with the loss of matric suction that reduces shear strength in surface soils (Collins and Znidarcic 2004). Rainfall infiltration has been shown to raise the water table to the slope surface, but this typically requires long duration rain events (Cho 2009). This chapter considers only the effect of increased water table elevations and does not analyze the rainfall conditions that may lead to this increase.

Pavement cracking due to the sliding has been observed along the southbound shoulder that likely represents the head scarp of the slide. The length of cracking along the southbound shoulder is roughly 63 m. The location of the landslide toe has not been observed but is thought to be beyond the Alabama Department of Transportation (ALDOT) right of way (ROW) that is about 25 m northwest of the guardrail along the southbound shoulder (roughly along the line connecting borings B5 to B8). Water was observed at the ground surface beyond the ALDOT right of way near a small creek that is located about 70 m northwest of the roadway.

Investigations at this site initially consisted of borings and soil index testing (i.e., Atterberg limits) performed by ALDOT. The initial location of the failure plane was estimated by ALDOT personnel based on site observations and initial LEM analysis as inclinometer data is not available at this site. Additional geophysical (e.g., ERI and MASW) and lab testing (e.g., ring shear and index testing) is performed by Auburn University researchers to supplement the ALDOT investigation for site characterization purposes.

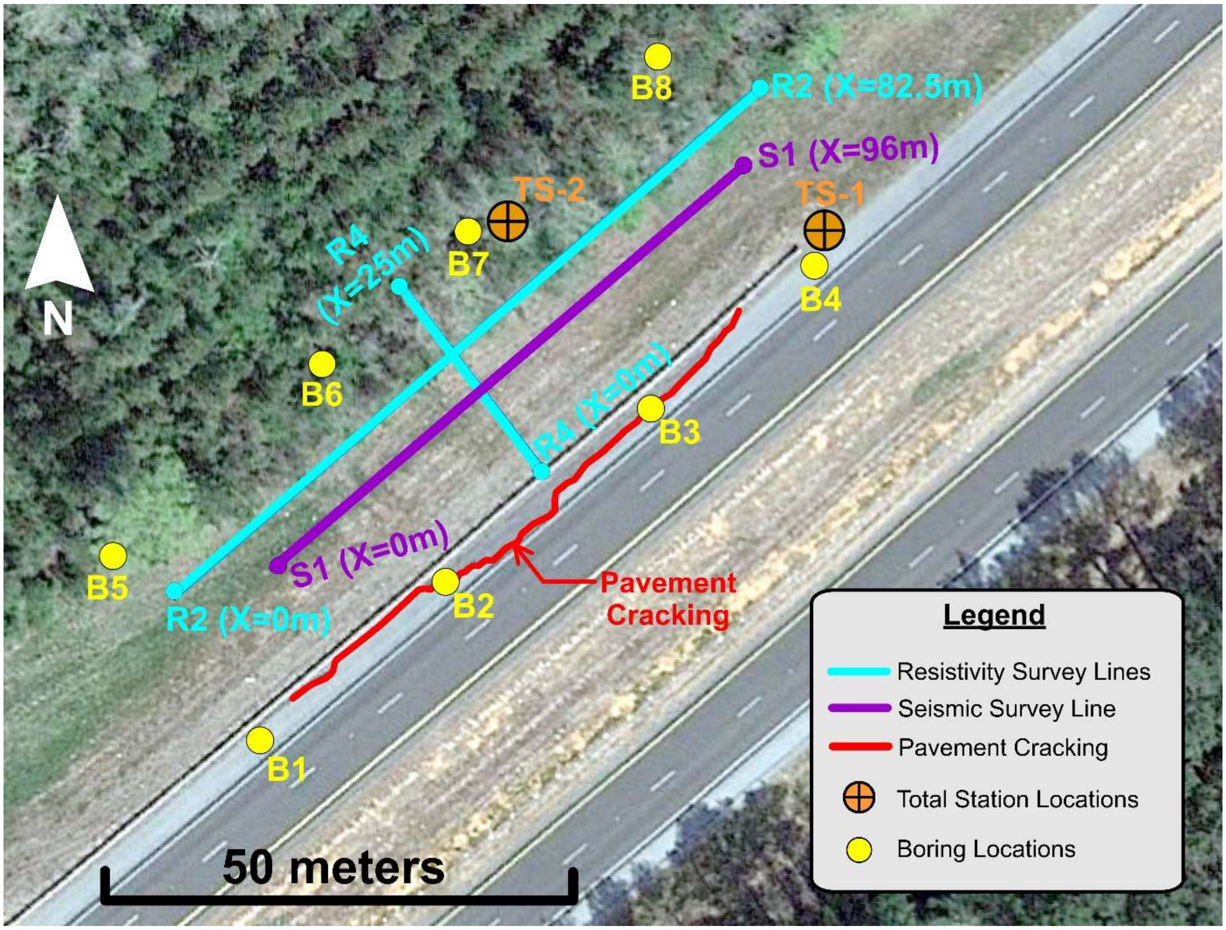

Figure 4- 1: Site map with locations of resistivity lines, seismic survey line, pavement cracking, total station, and borings

4.3 SITE GEOLOGY

The surface geology at the site has been mapped within the Oligocene series undifferentiated geologic unit (Figure 4-2). The Oligocene unit near the project area generally consists of medium to coarse grained sands; thin-bedded limestone; calcareous and carbonaceous clays; underlain by soft limestone and marl (Szabo et al. 1988, Cook et al. 2004). Figure 4-2 also shows that a Miocene series undifferentiated unit lies within 55 m of the project site. The Miocene unit near the project are generally consists of fine to coarse grained sand, sandy clays, and plastic clays (Szabo et al. 1988, Cook et al. 2004). Alluvial coastal and low terrace deposits also exist about 1 km from the project site (Figure 4-2). Sinkholes have also been observed along the interstate near this area (GSA 2010), but no evidence of sinkhole activity has been observed at this site.

Figure 4- 2: Site map showing geologic units and site location (geologic map after Szabo et al. 2004). Roadway locations are from Google Earth.

4.4 METHODOLOGY

This study utilizes geophysical methods combined with traditional geotechnical explorations and lab tests to characterize the landslide site described above. Borings were drilled in December 2020 and clay samples were collected for index and ring shear testing. Electrical resistivity and seismic data were collected in April and May 2021. Each of the characterization tools utilized in this study are described below.

4.4.1 *Total Station*

Total station data is collected to identify the locations of important features and estimate topography along the geophysical survey lines. Total station surveys are performed using a Topcon GTS-230W electronic total station. Total station data is primarily used to estimate topography along each geophysical survey line. The locations of landmarks and known boreholes are also surveyed with the total station to create a detailed site map.

4.4.2 *Drilling and SPT*

Drilling and SPT testing at this site was performed by ALDOT in December 2020. Borings were drilled using a CME 550X ATV rig, a CME 850X track mounted rig, and a CME 45LC track mounted ATV rig. Hollow stem augurs with inner diameters of 5.7 cm (2.25”) were used for these boreholes. Each rig was also equipped with a 623 N (140 Lbf) automatic hammer that was used to perform SPT testing. A total of 8 borings were drilled (Figure 4-1) at the site. The borings near the roadway shoulder (B1, B2, B3 and B4) were each drilled to a depth of 10.7 m (35’). The borings performed lower on the slope (B5, B6, B7 and B8) were each drilled to a depth of 7.6 m (25’). SPT testing was also performed in each boring at intervals of 46 cm (18”) in the upper 2 m (6’) and at intervals of 1.5 m (5’) below this depth. Recovered samples were tested to determine the Atterberg limits for clayey soils and used to create remolded specimens for the ring shear tests.

4.4.3 *Electrical Resistivity Imaging (ERI)*

Two electrical resistivity surveys were performed on April 13, 2021 (R2) and May 26, 2021 (R4). A summary of the resistivity surveys performed including date performed, number of electrodes used, electrode spacing, and line length are shown in Table 4-1. All surveys are performed with a commercial 8-channel SuperSting system from Advanced Geosciences Incorporated (AGI 2014). All surveys utilized both dipole-dipole and strong gradient arrays. Inversion of the measured resistivity data is performed using the commercial software EarthImager 2D (AGI 2014) to estimate 2D pseudo-sections of subsurface resistivity distribution. The terrain along each survey line is incorporated into the inversions as estimated using a Topcon GTS-230W electronic total station. The strong gradient and dipole-dipole data is inverted jointly for each survey.

Table 4- 1: Summary of resistivity surveys

Line	Date Performed	# Electrodes	Electrode Spacing (m)	Line Length (m)	Downslope or Cross-Slope
R2	4/13/2021	56	1.5	82.5	Cross-Slope
R4	5/26/2021	51	0.5	25	Downslope

4.4.4 Seismic Testing

Seismic data was collected on April 13, 2021. A set of 48 R.T. Clark and Geostuff 4.5-Hertz geophones spaced at 2m and a Geometrics Geode seismograms recorder is used to collect the seismic data. A geophone spacing of 2 m (6.6 ft) was used for a total line length of 94 m. Active surveys are performed using a 45 Newton (10 lb.) sledgehammer with a sampling frequency of 2000 Hz. Passive data is also collected at a sampling frequency of 250 Hz. The seismic data is processed using the multichannel analysis of surface waves (MASW) technique. Dispersion curves are created and combined for the passive and active data. An inversion procedure is then performed to determine a one-dimensional velocity model within the desired threshold for least squares fit.

The open-source software Geopsy (Wathelet 2005) is used to select dispersion curves and perform inversions.

Resolution of MASW data at shallow depths depends on the shortest wavelengths that can be represented in the dispersion curve which is controlled by geophone spacing (Lin et al. 2004). The thinnest layer that can be accurately detected by MASW has been shown to be approximately equal to the geophone spacing (Park et al. 1999). MASW data shallower than the geophone spacing may therefore be unreliable and should be interpreted with caution. MASW may be able to identify soil layers thinner than the geophone spacing at greater depths due to the interaction of surface waves with different frequencies and velocities. The maximum depth of investigation for MASW surveys depends primarily on the input source and frequency characteristics of the subsurface and the survey length (Taipodia and Dey 2018). The maximum depth of investigation for active surveys using a sledgehammer as a seismic source is typically limited to about 20 m (Taipodia and Dey 2018). The depth of investigation for passive surveys can be greater due to the longer wavelengths typically associated with passive wavefields (Baglari et al. 2018). The maximum depth of investigation is usually considered to be about half the longest wavelength represented by the dispersion curve (Park and Carnevale 2010).

4.4.5 Ring Shear Testing

Remolded clay specimens from borings B6 and B7 from depths of 1.37 m (4.5’) to 1.83m (6 ‘) are tested in a Bromhead ring shear apparatus. A specimen from boring B7 from depths of 4.12 m (13.5’) to 4.57 m (15’) is also tested. The ring shear tests are used to determine the fully softened drained strength (τ_{fss}) and the residual drained strength (τ_{res}) of the clay at the landslide site. Atterberg limits of each specimen are also determined with liquid limits ranging from 102% to 118%, plasticity limits ranging from 42% to 53%.

The ring shear tests for this study are performed by reconstituting the clay specimens are first to a desired water content and allowing them to rehydrate for 24 hours. The clay specimens are then placed in the ring shear container and pre-consolidated to 4.6 kPa. Clay specimens are then consolidated to the desired stress level. Vertical displacements versus time are measured during consolidation to determine appropriate shearing rates for the ring shear test according to ASTM D7608. The clay specimens are then sheared to determine the fully softened drained strength and residual drained strength envelope for each sample location.

4.4.6 Slope Stability Analyses

Slope stability analyses for this site are performed using both LEM and SRM. LEM analyses are performed using the commercial software SLIDE 2 (Rocscience 2021). Factors of safety for both circular and noncircular failure surfaces are determined with Spencer's Method. Both linear and nonlinear strength envelopes are considered for the drained strengths for LEM, while the undrained strengths are modeled using a strength ratio. SRM analyses are performed using FLAC V8.0 (Itasca 2016). Undrained shear strengths ($S_{u,pk}$) are represented using the Mohr-Coulomb constitutive model. The cohesion value in each zone is set to the appropriate value of $S_{u,pk}$ by multiplying the selected peak undrained shear strength ratio ($S_{u,pk}/\sigma'_v$) by the vertical effective stress in the zone and the friction angle (ϕ) is set to zero. Fully softened and residual strengths are represented using the MHB constitutive model to account for the nonlinear strength envelope of the clay. MHB parameters are calibrated to the measured strength envelopes using single element consolidated drained triaxial drivers (CDTX) in FLAC V8.0.

4.5 SITE CHARACTERIZATION

4.5.1 Integrated Characterization

Site stratigraphy is determined using information from the drilling explorations, index tests, electrical resistivity imaging and seismic testing (Figure 4-3 and 4-4). Boring logs show 1m to 4m of clayey sands at the surface underlain by fat and lean clays with some elastic silts in borings B2 and B8. Thin intervals of limestone are also reported in the clay layers. A 20 cm (8”) thick limestone interval was encountered near boring B6 at a depth of 3.2 m (10.5’). Borings indicate the limestone interval to be a bit deeper for the borings on the roadway shoulder. The water table is estimated to exist at the top of the clay layer from borings B5, B6 and B7. Water table information is not reported for the other borings. The slide plane location shown in Figures 4-3 and 4-4 is estimated by ALDOT personnel based on site observations and boring information. Geophysical testing and slope stability analyses are used in this study to confirm the location of the slide plane.

The resistivity results in Figure 4-3 were collected near B6 and B7 (R2) and show a high resistivity layer (14 to 100 ohm-m) near the surface (above 80 m) that corresponds to the clayey sand layer encountered in the borings. A lower resistivity layer (< 5 ohm-m) is shown between elevations of 76 m to 80 m that corresponds to the to upper portion of the fat clay and lean clay (B6) encountered in the borings. Liquid limits tend to be higher in this low resistivity layer (100% to 135%) than the other than the deeper moderate resistivity layer (40% to 100%). The slide plane is estimated to exist in this low resistivity layer with high liquid limits. A zone of intermediate resistivity (10 to 25 ohm-m) exists between elevations of 73 and 76 m. This zone corresponds to fat clay and elastics silts from the borings and has slightly lower liquid limits. A deeper low resistivity zone (< 5 ohm-m) also exists below an elevation of about 73 m. This layer exists below the bottom of the borings so estimating the soil type is uncertain, but it is likely saturated limestone or marl based on the site geology. This layer is far below the expected failure planes and so it has no effect on the analyses in this study.

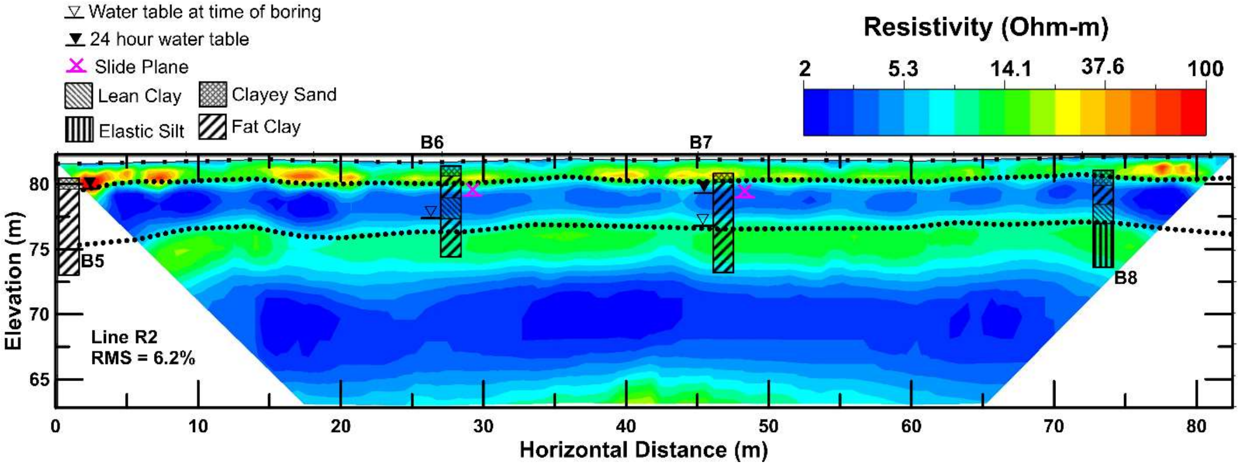

Figure 4- 3: Inverted resistivity profile for line R2 with boring information and estimated slide plane location

The results shown in Figure 4-4 are for the downslope resistivity line (R4). The resistivity line is placed between borings B2, B6 and borings B3, B7. The results are therefore compared to each respective set of borings and compare well with the results of Figure 4-3. A high resistivity layer (>50 ohm-m) is shown near the surface. This high resistivity layer is about 1 m thick near borings B6 and B7 and becomes thicker near the roadway shoulder. This high resistivity layer generally corresponds with the location of the clayey sand layer encountered in the borings that is also thicker near the roadway shoulder. The lower 1 m of this layer is classified as silty clay in boring B2. The resistivity in the clayey sand is about 5 times higher than shown in Figure 4-3. This may be due to the fact that it had rained for a few days prior to data collection of line R2 and it had not rained for over a week prior to data collection of line R4.

A low resistivity layer (2 to 10 ohm-m) exists beneath the clayey sand layer and is about 2.5 m thick. This low resistivity layer generally corresponds to fat clay from the borings B3, B6 and B7. Elastic silt is also encountered in this zone in boring B2. Liquid limits (LL) in the fat clay tend to be significantly higher than the other soil layers. A zone of alternating low and high resistivity can be seen in Figure 4-4 at horizontal distances of 2.5 m to 5 m and elevations of 82 m to 85 m. This alternating pattern may be due to numerical artifacts associated with the inversion attempting to fit the measured data in that area or it is possible that a lower resistivity zone exists due to preferential infiltration along cracks and shear zones in this location. Either way, the results in this area should be interpreted with caution.

A layer of intermediate resistivity (10 to 25 ohm-m) exists beneath the low resistivity layer. This intermediate resistivity layer corresponds to lean clay in boring B6, elastic silt in boring B2, and fat clay in borings B3 and B7. A thin limestone layer is also encountered at a depth corresponding to the top of the intermediate resistivity layer near boring B6 and limestone intervals are also reported in this region in the other borings. The increase in resistivity may be due to the reduction in LL values and/or the presence of limestone.

Figure 4-4 also contains the shear wave velocity profiles obtained from the MASW survey. The different velocity profiles shown on Figure 4-4 correspond to different picks for the combined active and passive dispersion curves. The upper 2m of the velocity profile is not included as data shallower than the geophone spacing of 2 m used for this survey may be unreliable (Park et al. 1999). The shortest wavelength observed in the dispersion curves is about 3.5 m suggesting the upper 1.8 m of the velocity profile may be unreliable. The longest wavelength observed in the MASW dispersion curves is estimated to be 65m, so the maximum depth of investigation for this site is at least 30 m which is much deeper than the expected slide plane at the site. The velocity profile for this site is therefore applicable for depths ranging from 2 m to 30 m.

The velocity profiles for the different dispersion curve picks are in general agreement with each other at depths shallower than 5 m. The seismic results show a relatively low velocity (130 m/s) zone between 2 m to 4 m depth which corresponds to upper clay layer identified in the borings. The velocity decreases to 60 m/s near the bottom of the low resistivity layer which may indicate the location of the slide plane. The velocity then increases to values ranging from 600 m/s to 2000 m/s at greater depths depending on the dispersion curve pick. These results suggest the inversion is poorly constrained at greater depths. The higher range of the measured velocities are consistent with shear wave velocities of limestone measured in Alabama (Montgomery et al. 2020) limestone and the lower range is consistent with reported values for Oligocene marl (Mayne 2001) as expected based on geology at the site. The shear wave velocity results generally agree with the resistivity results, but the velocity layer transitions occur at slightly greater depths than the resistivity layer transitions. The results from ERI, seismic testing, geotechnical exploration results are considered together for estimating soil stratigraphy at the site in the next section.

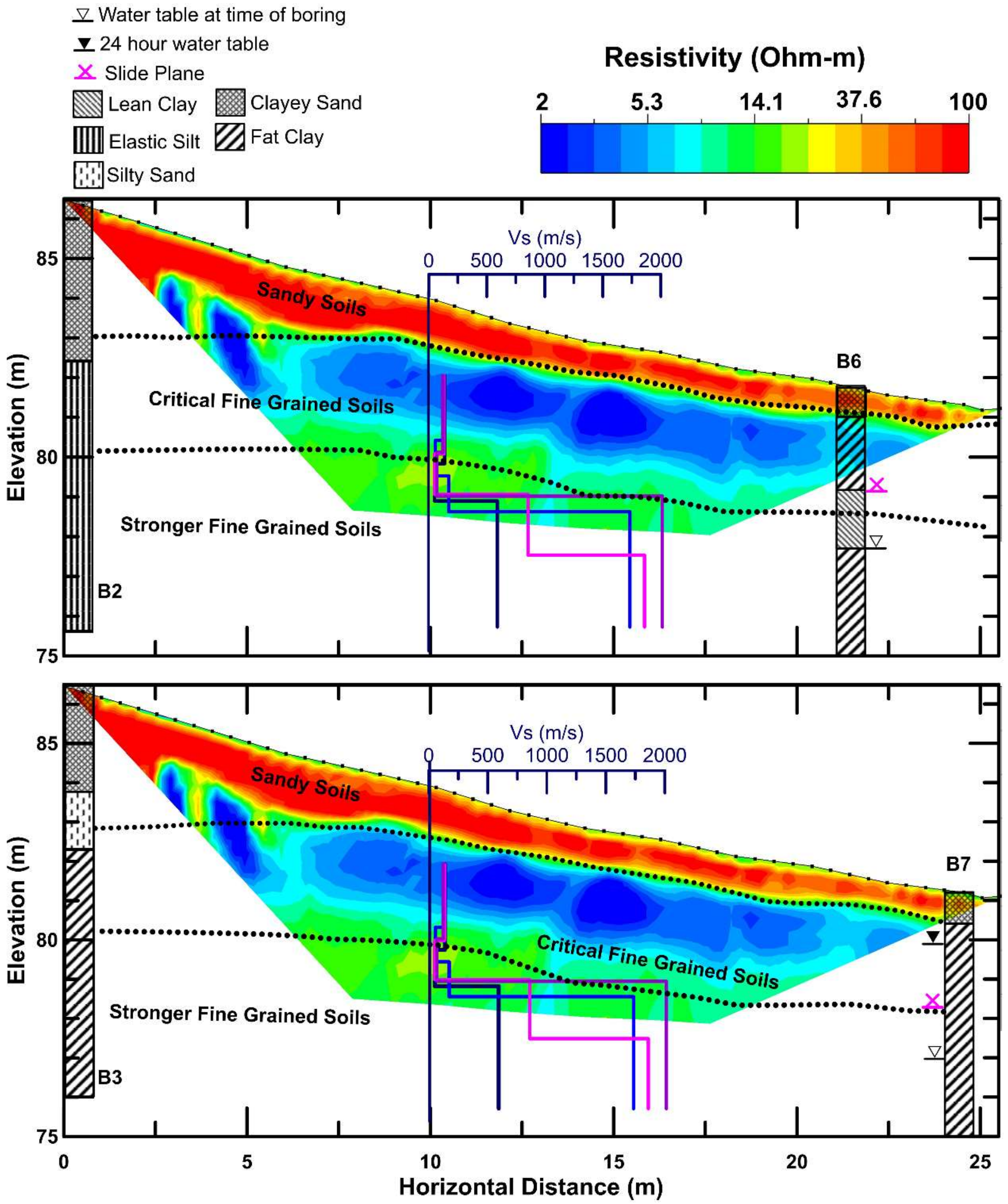

Figure 4- 4: Inverted resistivity profile for line R2 compared to borings B2/B3 and B6/B7 with shear wave velocity (V_s) profile from MASW line S1, boring information, and estimated slide plane location (Note: the different seismic profiles shown in blue, dark blue, purple and pink represent different dispersion curves selected for inversion of the measured MASW data)

4.5.2 Selected Site Model for Analyses

A simplified estimate of site stratigraphy to be used for analysis purposes is shown in Figure 4-5. This site model is developed by comparing the results of the geophysical and geotechnical explorations. ERI results are first compared to the boring data and Atterberg limits to identify soil layers corresponding to changes in resistivity. More credibility is given to the data in borings B2 and B3 due to uncertainty in the resistivity profile at horizontal distances less than 5 m from the start of the line. MASW results are then compared to ERI and borings to provide additional information regarding site stratigraphy as well as an estimate of shear wave velocities at the site. Stratigraphy at the site is then estimated to agree with all available data at the site.

The horizontal location of 0 m in Figure 4-5 is set to the location of the crest of the slope. Borings B1 – B4 exist near the roadway shoulder and borings B5 – B8 exist near the ALDOT right of way (ROW). Topography of the slope is estimated using total station measurements. A clayey sand layer is included near the surface which becomes thicker near the roadway shoulder. A clay layer is located beneath this sand layer which is about 2.5 m thick and represents soil within the suspected failure mass. The resistivity of this clay layer is lower than the surrounding soils which is consistent with resistivity results for landslides reported by Perrone et al. (2014). The top of the clay layer is interpreted from borings B2 and B3. Relatively low shear wave velocities are also reported in this clay layer. A thin limestone layer is located about 2.7 m below the top of the clay surface which is consistent with the location of the limestone layer encountered near B6 and with the depth of the interbedded clay and limestone from the other borings.

A significant increase in shear wave velocity is also observed near the expected location of the limestone interval. The clay layer beneath the thin limestone interval may also contain thin limestone intervals as reported in the borings. The presence of limestone is consistent with increases in resistivity and shear wave velocity. The soils in the deeper low resistivity layer (Figure 4-3) could not be confirmed from the geotechnical explorations and so is listed as unknown in Figure 4-3. This layer is likely either limestone or marl based on the site geology.

The water table at the site is also shown in Figure 4-5. The water table is assumed to exist near the top of clay layer beneath the roadway shoulder and at the ground surface beyond the ALDOT ROW. This assumption is consistent with site observations of standing water at the ground surface beyond the ROW. The location of the water table shown in Figure 4-5 is also assumed to represent elevated ground water levels after high intensity or long duration rain events after which additional ground movements at the site are typically observed.

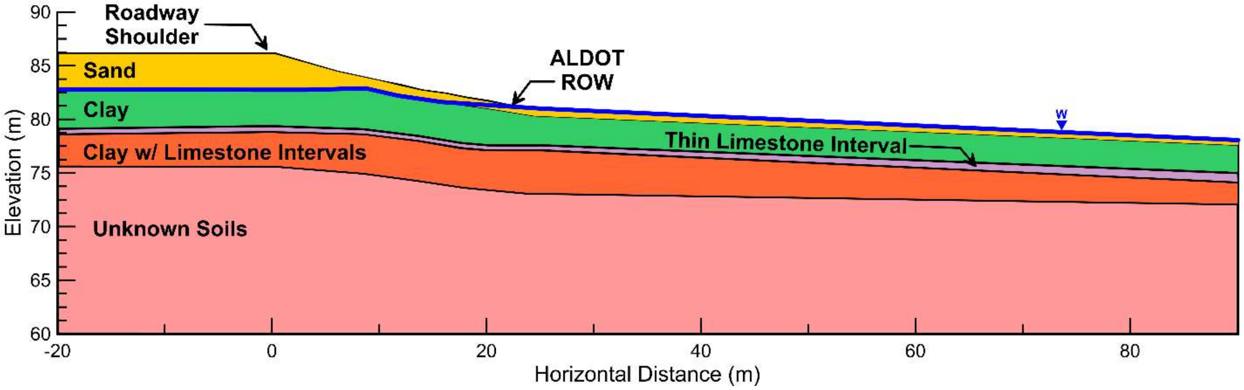

Figure 4- 5: Simplified site model to be used in slope stability analyses as estimated from integrated site characterization for analysis purposes

4.6 ESTIMATION AND IMPLEMENTATION OF SOIL PROPERTIES

4.6.1 Unit Weight and Elastic Modulus of Clay

The saturated unit weight of clay at the site is estimated to be about 16.7 kN/m^3 based on measurements collected during the ring shear testing. Soil moduli are estimated using the density of the clay and a shear wave velocity of 130 m/s as measured by the MASW testing. Elastic moduli are not needed for LEM but is used in SRM. Cheng et al. (2007) found FS values in SRM analyses are relatively insensitive to the chosen value of elastic modulus.

4.6.2 Peak Undrained Shear Strength of Clay

Peak undrained strength ($S_{u,pk}$) for clay is unavailable at the site so published correlations are used to estimate the undrained peak strength ratios ($S_{u,pk}/\sigma'_v$). Mesri (1989) suggested $S_{u,pk}/\sigma'_v$ is equal to 0.22 for normally consolidated clays, while Jamiliokowski et al. (1985) suggested a range from 0.19 to 0.23. This study examines $S_{u,pk}/\sigma'_v$ values of 0.19, 0.21, and 0.23 to account for uncertainty of normally consolidated strength and OCR. The LEM analyses in this study utilize a vertical stress ratio to represent undrained shear strength. SRM analyses utilize a Mohr-Coulomb model with a friction angle of zero and cohesion set to a value of $S_{u,pk}/\sigma'_v$ multiplied the initial value of vertical effective stress in each zone.

4.6.3 Fully Softened Drained Shear Strength of Clay

The drained shear strength of the clay at the site is estimated by ring shear tests performed on reconstituted specimens. The fully softened shear strength (τ_{fss}) is defined as the peak drained shear strength of a clay soil under normally consolidated conditions (Skempton 1970). Previous research has shown the fully softened strength to be appropriate for analyzing slope stability in first time failures in high plasticity clay soils (e.g., Wright et al. 2007, Xuan et al. 2021). Ring shear data for specimens collected from borings B6 and B7 is shown in Figure 4-6. The data in Figure 4-6 shows a nonlinear relationship between τ_{fss} and the applied vertical effective stress (σ'_v) for each specimen in which the shear strength increases more rapidly at lower values of σ'_v. The clay samples collected for ring shear testing correspond to in-situ vertical effective stresses of roughly 20 kPa (1.83 m) and 40 kPa (4.57 m) which is at the lower range of stresses shown in

Figure 4-6. A power curve of the form $\tau_{fss} = a(\sigma'_v)^b$ is therefore fit to the ring shear data for use in LEM analyses. The fitted parameters 'a' and 'b' selected for each specimen are also shown in Figure 4-6. The power curves are fitted to the ring shear data at effective stresses up to 250 kPa. Coefficient of determination (R^2) values are also shown in Figure 4-6 which illustrates how well each power curve fits the data and describes the percentage of variation of shear strength that can be explained by changes in vertical effective stress for each power curve fit. The value of R^2 is above 0.99 for the shallower specimens (1.37 – 1.83 m) and is about 0.98 for the deeper specimen (4.11 – 4.57 m).

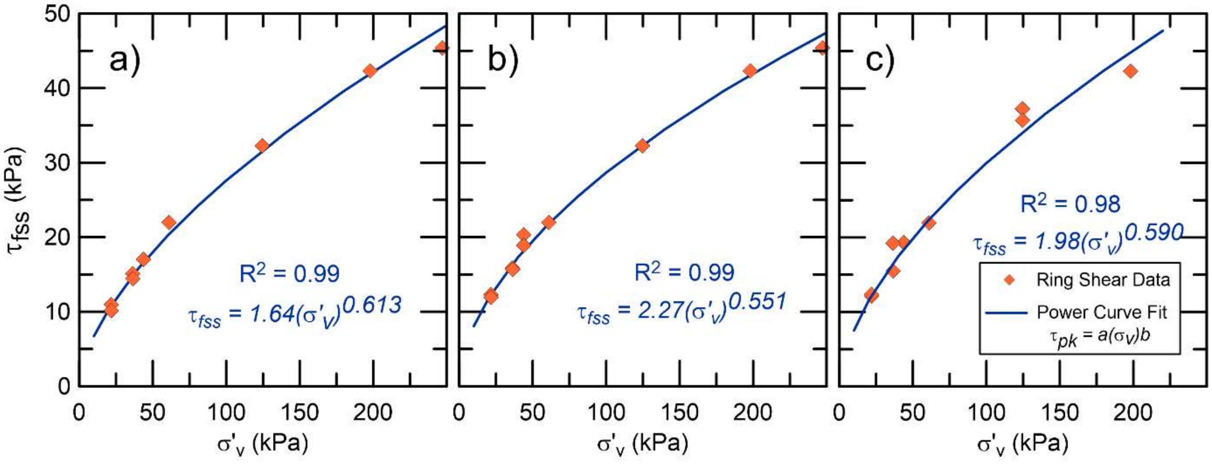

Figure 4- 6: Ring shear reconstituted fully softened drained strength data and power curve fits to be used in LEM analyses for specimens collected from a) B6 (1.37 to 1.83 m); b) B7 (1.37 - 1.83 m); c) B7 (4.11 – 4.57 m)

4.6.4 Residual Drained Shear Strength of Clay

Residual drained shear of clay at the site is estimated by ring shear tests performed on reconstituted specimens of clay collected from the site. Residual strengths obtained from reconstituted specimens (τ_{res}) are thought to accurately represent in-situ residual strengths since residual strength occurs when the soil fabric is completely broken down. Ring shear data for specimens collected from borings B6 and B7 is shown in Figure 4-7. The data in Figure 4-7 shows a nonlinear relationship between τ_{res} and the applied vertical effective stress (σ'_v) for each specimen in which the residual shear strength increases more rapidly at lower values of σ'_v. The clay specimens used for ring shear testing correspond to in-situ vertical effective stresses of roughly 20 kPa (1.83 m) and 40 kPa (4.57 m) which is at the lower range of stresses shown in Figure 4-8. A power curve of the form $\tau_{fss} = a(\sigma_v')^b$ is therefore fit to the ring shear data for use in LEM analyses. The fitted parameters 'a' and 'b' selected for each specimen are also shown in Figure 4-8. The power curves are fitted to the ring shear data at effective stresses up to 250 kPa. Coefficient of determination (R^2) values are also shown in Figure 4-6 which illustrates how well each power curve fits the data and describes the percentage of variation of shear strength that can be explained by changes in vertical effective stress for each power curve fit. The value of R^2 is above 0.99 for the shallower specimens (1.37 – 1.83 m) and is about 0.97 for the deeper specimen (4.11 – 4.57 m).

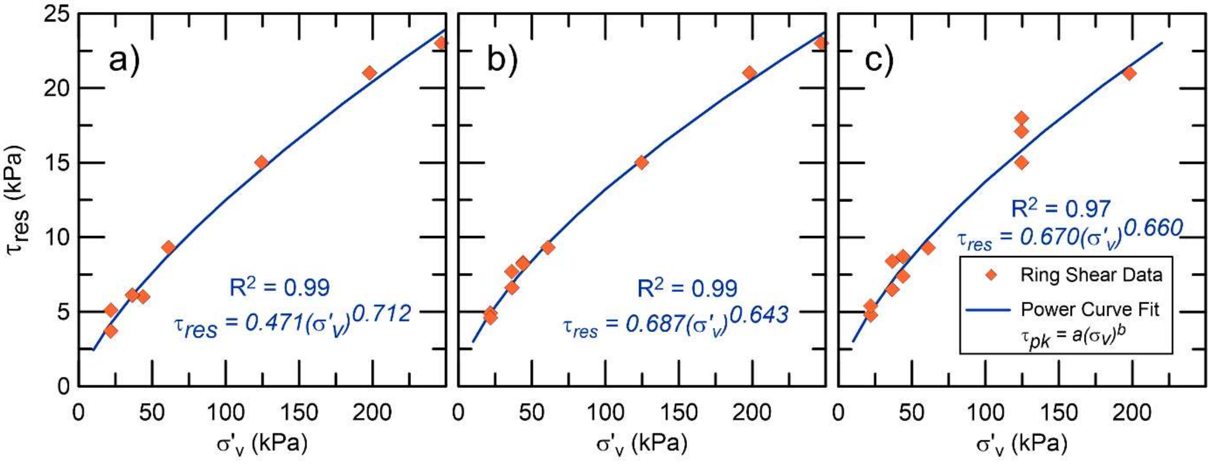

Figure 4- 7: Ring shear residual drained strength data and power curve fits to be used in LEM analyses for specimens collected from a) B6 (1.37 to 1.83 m); b) B7 (1.37 - 1.83 m); c) B7 (4.11 – 4.57 m)

4.6.5 Calibration of the Modified Hoek-Brown Constitutive model

SRM analyses are performed using FLAC V8.0 which does not include a power curve option for representing the nonlinear strength envelopes observed in the ring shear data. The Modified Hoek-Brown (MHB) constitutive model is therefore used to represent drained strengths in SRM analyses due to its ability to represent nonlinear shear strength behavior. Calibration of the MHB parameters to fully softened and residual drained strength is performed using a single element consolidated drained triaxial (CDTX) driver in FLAC. The MHB parameters σ_{ci}, m_b, a, and s are iteratively adjusted to fit the ring shear data at σ'_v values up to 250 kPa. Results from the model calibration are compared to the fully softened ring shear results in Figure 4-8. Results from the model calibration are compared to the residual strength ring shear results in Figure 4-9. The selected MHB parameters for the fully softened and residual drained shear strength calibrations are shown in Tables 4-3 and 4-7 respectively.

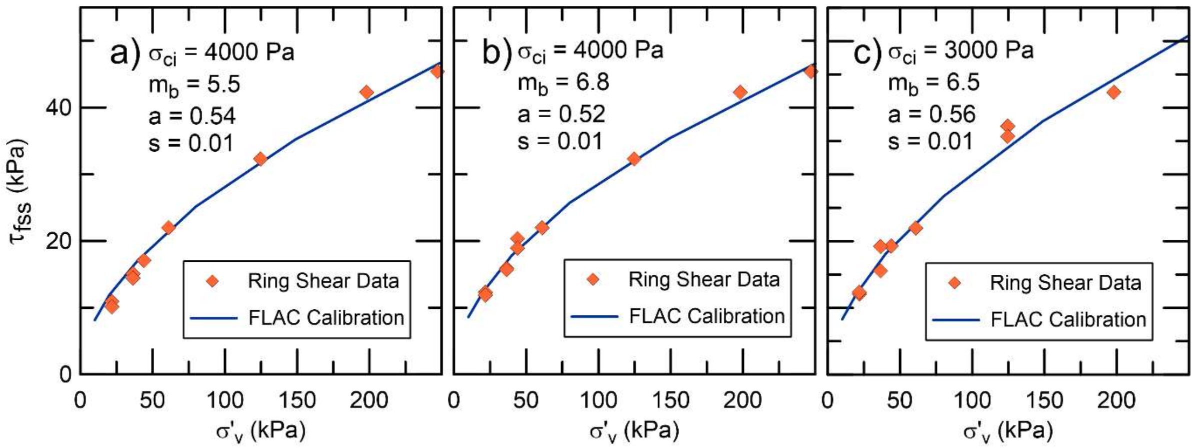

Figure 4- 8: Ring shear reconstituted drained fully softened strength data and MHB calibration curves to be used in SRM analyses for specimens collected from a) B6 (1.37 to 1.83 m); b) B7 (1.37 - 1.83 m); c) B7 (4.11 – 4.57 m)

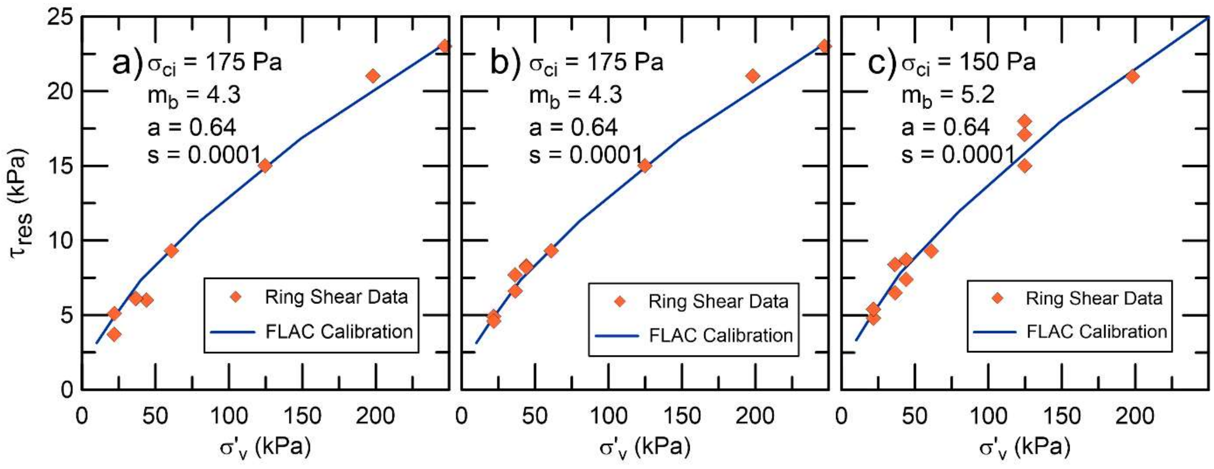

Figure 4- 9: Ring shear residual drained strength data and MHB calibration curves to be used in SRM analyses for specimens collected from a) B6 (1.37 to 1.83 m); b) B7 (1.37 - 1.83 m); c) B7 (4.11 – 4.57 m)

4.6.6 Properties of Non-Clay layers

SPT test data is used to estimate the effective stress friction angle and unit weight of the sand layer using raw blow counts (N) corrected to 70% energy at 95.76 kPa (1 tsf) of vertical stress (N'_{70}). The average N'_{70} values in the sand layer are found to be about 25. Correlations provided by Bowles (1996) are used to estimate the effective stress friction angle of the sand to be 34° and the wet unit weight to be 20 kN/m^3 based on N'_{70} values. The friction angle based on the average N_{60} value of 15 is determined to be 32° based on correlations provided by Wolff (1989), but friction angle estimates in this study are based on N'_{70} as they consider the influence of vertical effective stress. The shear wave velocity of the sand is estimated to be 130 m/s based on the results from the seismic testing.

The thin limestone interval, and deeper unknown soils, are assumed to have significantly larger strength than the other soil layers at the site. These layers are modeled using infinite strength in LEM analyses and the Mohr-Coulomb constitutive model in SRM analyses. Both layers are assumed to be limestone with an undrained shear strength of 2300 kPa based on reported values of unconfined compressive strength of limestone in Florida (McVay et al. 1992). The unit weight of the limestone interval and deeper soil layer is assumed to be 25 kN/m^3 based on values published in literature (e.g., Gaviglio 1989, Yaşar and Erdoğan 2014). The shear wave velocity of the limestone is estimated to be 1700 m/s based on the results from the seismic testing. None of the failure surfaces intersect this layer, so the results would not be affected by reasonable variations in these properties.

4.7 SLOPE STABILITY ANALYSIS

Slope stability analyses are performed to investigate probable failure mechanisms at the landslide site and to compare results using LEM and SRM. Fully softened drained shear strength is investigated first to determine if they the initial failure could have occurred under drained conditions. Peak undrained shear strengths are examined next to investigate the possibility of an initial undrained failure. Residual drained strengths are then examined to estimate stability of the slope on a pre-existing shear surface.

Slope stability analyses are performed using LEM in SLIDE2 (Rocscience 2021) with circular and noncircular surfaces. The critical circular surfaces are found using a grid search and critical noncircular surfaces are found using an iterative Cuckoo search. All FS values reported for the LEM analyses are calculated using Spencer's method. Nonlinear drained strength envelopes are represented using the power curve option included in SLIDE2. Undrained strengths are represented using the vertical stress ratio included in SLIDE2.

Slope stability analyses are also performed using SRM in FLAC V8.0 (Itasca 2016). Nonlinear drained strength envelopes are represented using the Modified Hoek-Brown constitutive model. The MHB model is formulated for use with rocks so input parameters cannot be estimated from correlations described in the model formulation (e.g., Hoek et al. 2002). MHB parameters for the clay are therefore calibrated to ring shear data using single element consolidated drained triaxial drivers, as previously discussed. Undrained shear strength in SRM analyses is represented using the Mohr-Coulomb constitutive model with the friction angle set to zero and the cohesion (undrained shear strength) is set by multiplying the undrained shear strength ratio ($S_{u,pk}/\sigma'_v$) by the vertical effective stress in each element.

4.7.1 Initial Drained Failure

LEM analyses are performed using fully softened drained strength parameters estimated for each of the sample locations from ring shear testing. The power curve parameters used in LEM analyses for each sample location and associated factors of safety are shown in Table 4-2. FS values range from 1.57 to 1.74 for the circular failure surfaces and 1.49 to 1.67 for the noncircular failure surfaces. The noncircular surfaces produce FS values about 10% lower than the circular surfaces. Failure planes using circular and noncircular surfaces from LEM analyses for the B6 strength parameters are shown in Figure 4-10. The failure planes shown in Figure 4-10 are generally consistent with those obtained for the remaining sample locations. The noncircular surface reaches the ground surface behind the location where cracking is observed along the shoulder and follows the limestone layer closely across the central portion of the embankment. The toe of the failure surface is located near the ALDOT ROW boundary. The circular failure surface is generally similar to the noncircular surface, but is a bit shallower due to the infinite strength assumed in the limestone layer.

Table 4- 2: Fully softened drained shear strengths as measured from ring shear testing, selected power fit parameters for LEM analyses, and factors of safety (FS) from LEM analyses

Fully Softened Drained Strength: $\tau_{fss} = a(\sigma'_v)^b$				
Location	a	b	FS Circular Surfaces	FS Noncircular Surfaces
B6 (1.37 - 1.83 m)	1.6381	0.6133	1.57	1.49
B7 (1.37 - 1.83 m)	2.2689	0.5541	1.71	1.63
B7 (4.11 - 4.57 m)	1.9800	0.5900	1.74	1.67

The calibrated MHB parameters and associated FS values from the SRM for each sample location are shown in Table 4-3. FS values range from 1.42 to 1.47, which is slightly lower than the FS values obtained from LEM analyses using noncircular surfaces. The MHB calibrations do not exactly match the power curves used in SRM which may lead to slight differences in FS values. Shear strain contours from the SRM results are shown in Figure 4-10 for the analyses using the B6 strength parameters. SRM do not provide a single failure surface, but the area of highest shear strain generally corresponds to the slide plane. The failure surfaces from the LEM analyses closely match the areas of greatest shear strain from the SRM giving additional confidence in the use of the MHB model to represent the strength of this clay. FS values generally agree with the LEM providing evidence that MHB is a practical tool for representing nonlinear strength envelopes of clays. SRM has been shown to more accurately represent complex failure surfaces compared to LEM as SRM is not constrained by the location and shape of the failure surface or assumptions regarding the inclination of interslice forces (VandenBerge and McGuire 2019).

Table 4-3: Fully softened drained shear strengths as measured from ring shear testing, MHB calibration for SRM analyses, and factors of safety (FS) from SRM analyses

Fully Softened Drained Strength (MHB)					
Location	σ_{ci} (Pa)	m_b	a	s	FS
B6 (1.37 – 1.83 m)	4000	5.5	0.54	0.01	1.42
B7 (1.37 – 1.83 m)	4000	6.8	0.52	0.01	1.46
B7 (4.11 – 4.57 m)	3000	6.5	0.56	0.01	1.47

The FS values obtained for each method using drained fully softened strength parameters are all higher than 1.4, indicating adequate stability against first time drained failure. The failure surfaces also indicate that cracking would be expected in the travel lanes, but the cracking has only occurred along the shoulder. Both the FS and failure patterns from these analyses suggest that the initial failure did not likely occur under drained conditions. Initial failure of the slope under undrained conditions is investigated in the next section.

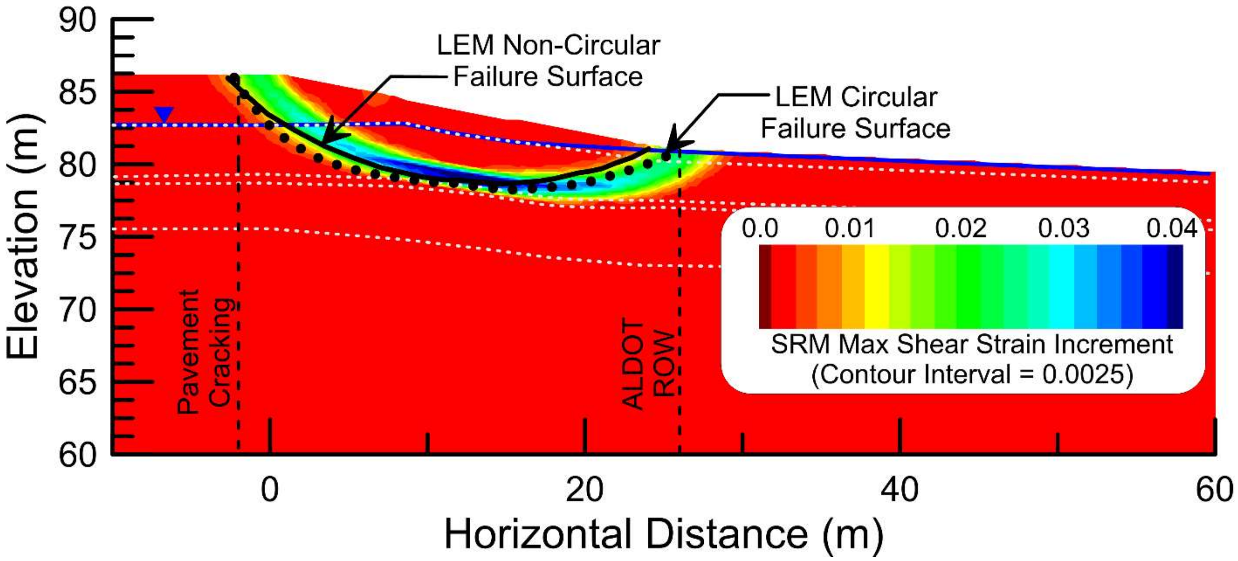

Figure 4- 10: Maximum shear strain interval contours (zoomed in on failure surface location) from SRM analysis using fully softened drained strengths from B6 with critical noncircular failure surface from LEM shown as solid black line and critical failure surface from LEM with circular surfaces shown by dotted black line. Locations of ALDOT ROW and observed pavement cracking are shown as dashed lines. Soil boundaries are shown by dotted light grey lines.

4.7.2 Initial Undrained Failure

The possibility of an undrained failure is investigated by using a vertical stress ratio equal to $S_{u,pk}/\sigma'_v$ for the clay layer, while keeping the other properties constant. The associated FS values are shown in Table 4-4. FS values range from 0.89 to 1.04 for the circular failure surfaces and 0.84 to 0.98 for the noncircular failure surfaces. The higher FS values observed for the circular failure surfaces are consistent with the LEM results of the initial drained failure investigation. The critical failure surfaces for $S_{u,pk}/\sigma'_v$ equal to 0.21 are shown in Figure 4-11. The noncircular surface is similar to the drained failure, but intersects the ground surface closer to the crest of the slope and is near vertical at this location. The critical circular surface is located on the face of the slope downhill from the roadway.

Table 4- 4: Selected peak undrained shear strength ratios and factors of safety (FS) from LEM analyses

Peak Undrained Strength		
$S_{u,pk}/\sigma'_v$	FS Circular Surfaces	FS Noncircular Surfaces
0.19	0.89	0.84
0.21	0.97	0.91
0.23	1.04	0.98

The FS values for each $S_{u,pk}/\sigma'_v$ value from the SRM are shown in Table 4-5. FS values range from 0.94 to 1.10, which is slightly higher than the FS values obtained from the circular surfaces and approximately 10% higher than the noncircular surfaces. This differs from the SRM analyses using fully softened drained strengths in which the LEM FS values are higher. The shear strain contours from the SRM analysis for $S_{u,pk}/\sigma'_v$ equal to 0.21 are shown in Figure 4-11. The contours indicate a failure surface similar to the critical noncircular surface would be expected, although the location of likely cracking (where the failed and intact portions meet) is slightly further away from the crest of the slope.

The location of this failure plane also aligns with the location of the drop in shear wave velocity observed in the MASW testing. Figure 4-12 plots a 1D shear wave velocity profile from the MASW results on top of the shear strain contours for $S_{u,pk}/\sigma'_v = 0.21$. The decrease in velocity from the MASW profile corresponds well with the location of the critical failure surface from the SRM analysis. These results indicate that low velocity in the MASW results may correspond to the location of the failure plane which is slightly deeper than originally estimated based on the resistivity results.

Table 4- 5: Selected peak undrained shear strength ratios and factors of safety (FS) from SRM analyses

Peak Undrained Strength	
$S_{u,pk}/\sigma'_v$	FS
0.19	0.94
0.21	1.02
0.23	1.10

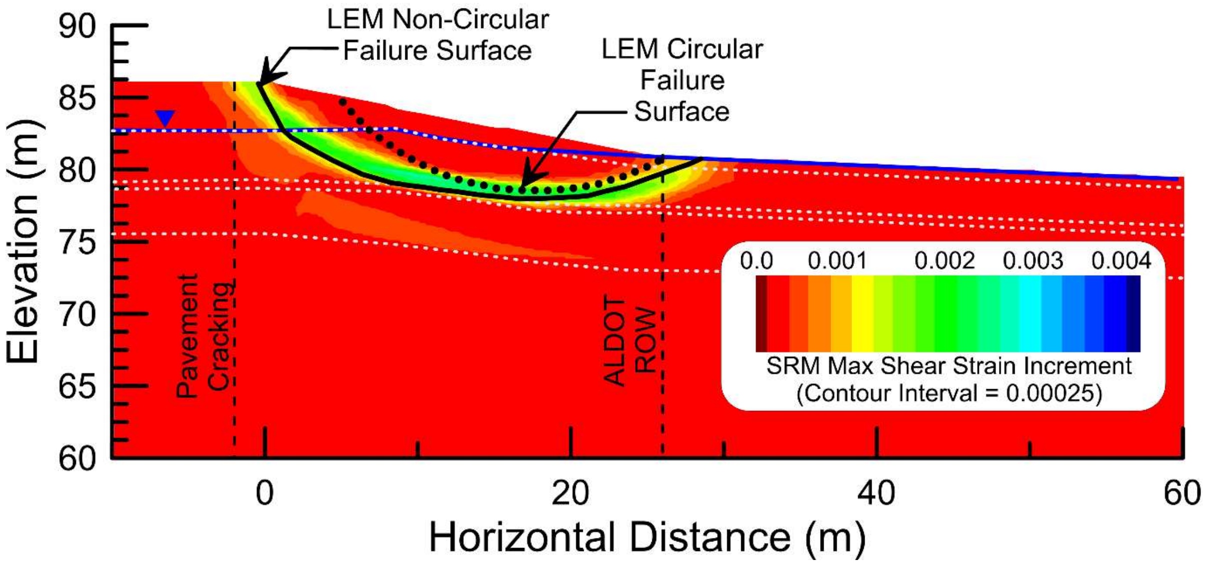

Figure 4- 11: Maximum shear strain interval contours (zoomed in on failure surface location) from initial peak undrained ($S_{u,pk}/\sigma'_v = 0.21$) SRM analysis with critical noncircular failure surface from LEM shown as solid black line and critical failure surface from LEM with circular surfaces shown by dotted black line. Locations of ALDOT ROW and pavement cracking shown by dashed black lines. Soil layer boundaries shown by dotted light grey lines.

The FS values obtained for SRM and LEM using undrained shear strength parameters are close to 1 for most $S_{u,pk}/\sigma'_v$ values. This indicates that the slope would be susceptible to undrained failure under current conditions. Undrained failure would need to be triggered by rapid loading, but it is unclear what that mechanism would be for the current slope. It is possible that the slope experienced an undrained failure during initial embankment construction when effective stresses in the clay, and therefore undrained strengths, would have been even lower than they are now. This initial failure would then have created a failure plane within the slope on which movements may still be occurring. The next section examines the stability of the slope under residual drained strength conditions, that would be expected to be mobilized on any existing failure surface.

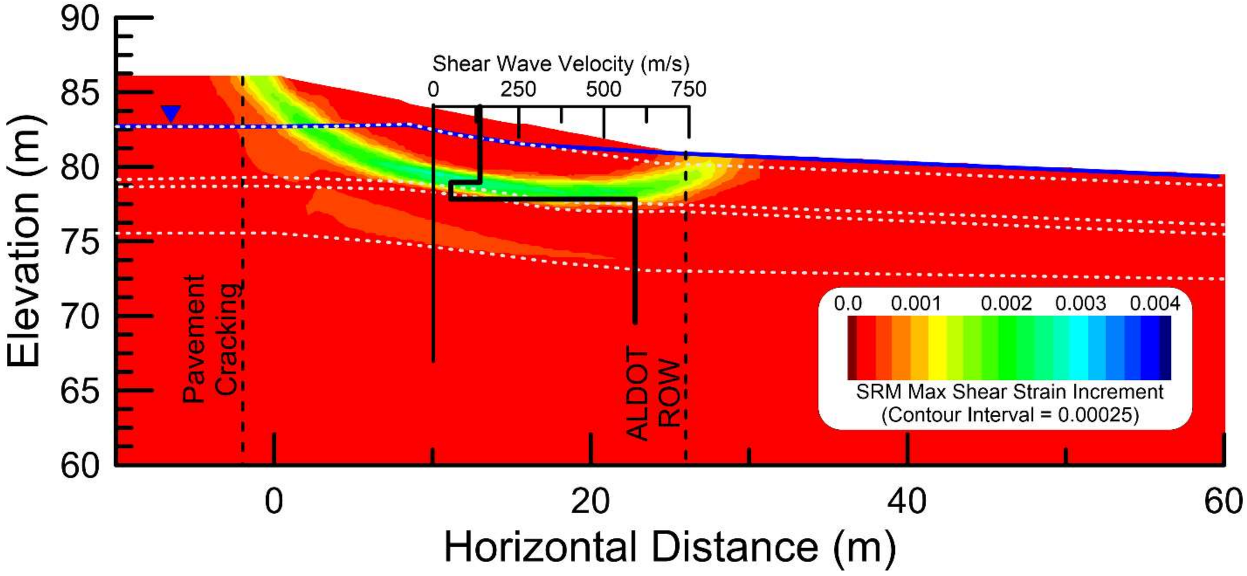

Figure 4- 12: Maximum shear strain interval contours (zoomed in on failure surface) from initial peak undrained SRM analysis with single 1D shear wave velocity profile from MASW results

4.7.3 Residual Drained Failure

LEM analyses are performed using power curve residual drained strength parameters estimated for each of the sample locations from ring shear testing. The power curve parameters used in LEM analyses for each sample location and associated factors of safety are shown in Table 4-6. FS values range from 0.81 to 0.91 for the circular failure surfaces and 0.71 to 0.80 for the noncircular failure surfaces. The noncircular FS are approximately 10% less than the circular results, which is consistent with the previous analyses. Failure planes using circular and noncircular surfaces from LEM analyses using the B6 strength parameters are shown in Figure 4-13. The failure planes shown in Figure 4-13 are generally consistent with those obtained for the remaining sample locations. The noncircular surface is generally similar to the previous analyses with the surface intersecting the roadway near the location of observed cracking and traveling along the limestone layer through the central portion of the slope before exiting just beyond the ROW boundary. The circular surface is shifted a bit further upslope and would indicate that cracking would be likely to occur in the travel lanes and that the toe of the slope would be within the ROW, neither of which are consistent with observations.

Table 4- 6: Residual drained shear strengths as measured from ring shear testing, selected power fit parameters for LEM analyses, and factors of safety (FS) from LEM analyses

	Residual Drained Strength $\tau_{res} = a(\sigma'_v)^b$			
Location	a	b	FS Circular Surfaces	FS Noncircular Surfaces
B6 (1.37 - 1.83 m)	0.471	0.712	0.81	0.71
B7 (1.37 - 1.83 m)	0.687	0.643	0.88	0.78
B7 (4.11 - 4.57 m)	0.670	0.660	0.91	0.80

The calibrated MHB parameters from the SRM and associated FS values for each sample location are shown in Table 4-7. The shallower B6 and B7 sample strength characteristics using SRM produce slightly higher FS values than LEM with noncircular surfaces, while strength characteristics from the deeper B7 sample are lower than LEM. The results from SRM and LEM appear to generally agree so the differences between SRM and LEM with noncircular surfaces may be due to the different representations of residual drained shear strength used with each method. The shear strain contours from the SRM analysis using the B6 strength parameters are shown in Figure 4-13. The contours indicate a failure surface similar to the critical noncircular surface would be expected. The location of this failure plane also aligns with the location of the drop in shear wave velocity shown in Figure 4-4.

Table 4- 7: Residual drained shear strengths as measured from ring shear testing, MHB calibration for SRM analyses, and factors of safety (FS) from SRM analyses

	Residual Drained Strength				
Location	σ_{ci} (Pa)	m_b	a	s	FS
B6 (1.37 – 1.83 m)	175	4.3	0.64	0.0001	0.76
B7 (1.37 – 1.83 m)	175	4.3	0.64	0.0001	0.76
B7 (4.11 – 4.57 m)	150	5.2	0.64	0.0001	0.79

The FS values obtained for each method using drained fully softened strength parameters are significantly lower than 1 indicating that continued movement of the slope may occur on a preexisting failure plane under drained loading. However, such low FS values would indicate that large movements would be expected at the site, which is not consistent with observations. It is possible that the mobilized strength is between the residual and fully softened strengths due to either strength gain or the slope may not have moved enough to fully remold the materials along the failure plane. Previous research indicates that that once movement stops soil within the failure plane may gain strength (e.g., D'Appolonia et al. 1967, Ramiah et al. 1973, Skempton 1985), but little movement may be required to re-mobilize the drained residual shear strength (Stark and Hussain 2010). The effect of strength gain on the failure plane is investigated in sensitivity studies present later in this chapter.

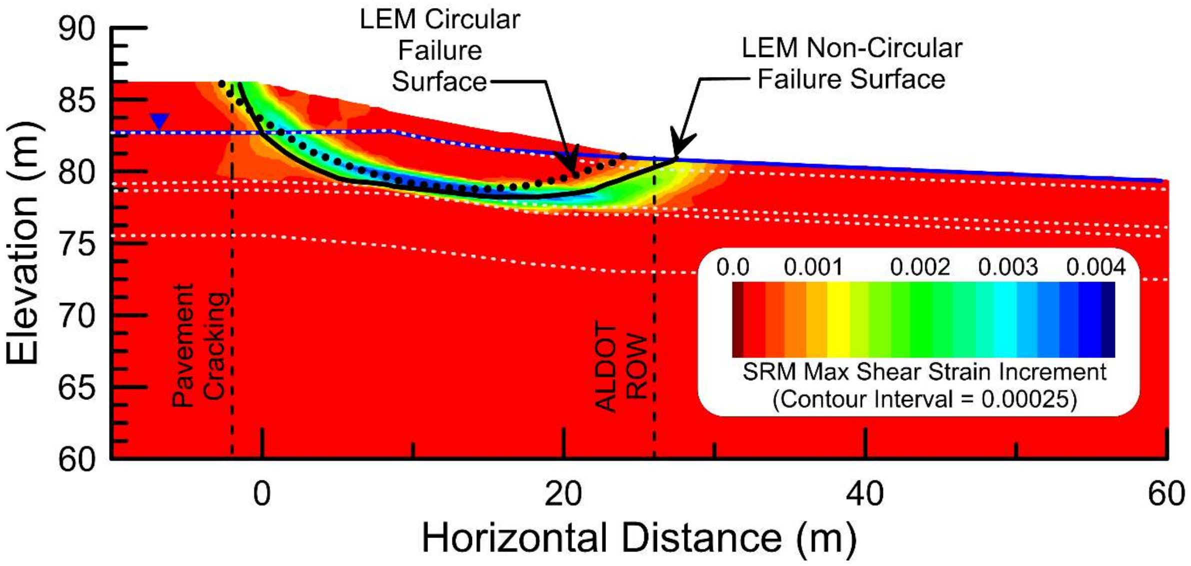

Figure 4- 13: Maximum shear strain interval contours (zoomed in on failure surface) from SRM analysis with residual drained strength from B6. Critical noncircular failure surface from LEM are shown as solid black line and critical failure surface from LEM with circular surfaces are shown by dotted black line. Locations of ALDOT ROW and pavement cracking shown by dashed black lines. Soil layer boundaries shown by dotted light grey lines

4.8 SENSITIVITY STUDIES

This section investigates the sensitivity of slope stability analysis results to some of the chosen input parameters. Analyses are performed using a linear strength envelope for the drained strength, as is more commonly used in practice. The effect of changes in the water table elevation and different levels of strength gain are also investigated. The sensitivity studies are performed using LEM with noncircular failure surfaces, as these are the critical mode for LEM analyses and are generally similar to the results from the SRM.

4.8.1 Effect of Linear Failure Envelope

The effect of using a linear envelope to represent drained strength is examined using LEM analyses with noncircular surfaces and residual drained strength parameters for the sample from B6. The linear strength envelope is modeled using the Mohr-Coulomb failure criterion in SLIDE2.

A linear trendline is fit to the residual drained strength ring shear data from B6 at vertical effective stresses below 75 kPa (Figure 4-14), as these lower stresses are more applicable to the failure surfaces in this slope. A cohesion intercept of zero is used and the residual drained friction angle is determined to be 9°. The FS of the slope using this linear fit produces a FS value of 0.78 which is approximately 10% higher than the value estimated using a power curve fit FS value of 0.71. These results suggest that a linear envelope may produce reasonable results provided that is fit over the stress range expected at the site. Had the full range of stresses from the experiments been used, the friction angle would have been underestimated significantly. The use of a nonlinear failure envelope eliminates the need to consider different fits for sites with a larger variation in in-situ effective stresses.

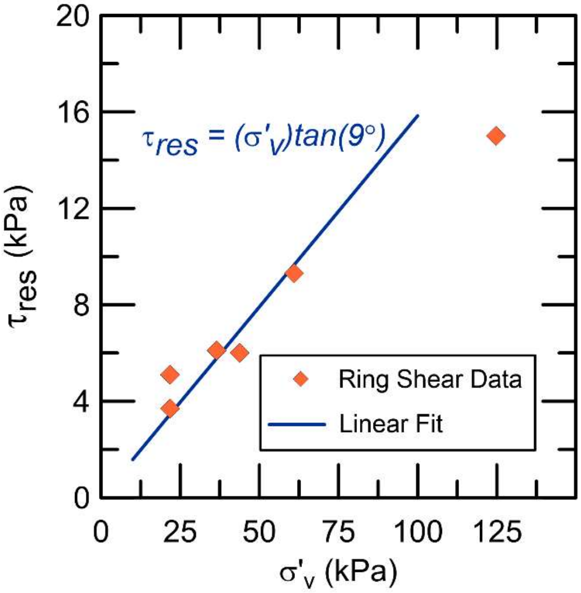

Figure 4- 14: Linear fir to ring shear data at vertical effective stresses below 75 kPa for use with Mohr-Coulomb failure criterion in LEM analyses

4.8.2 *Effect of Water Table Elevation*

The effect of the water table (WT) elevation on slope stability is examined using LEM analyses and drained strength power curve parameters for the sample from B6. Analyses are performed with the water table at the ground surface, 2m lower than the baseline WT, and at the top of the limestone interval (see Figure 4-5). The FS values for the LEM analysis with different WT locations are shown in Table 4-8. FS values are shown to increase with decreasing WT elevation as expected. The FS value using the fully softened strength and the water table at the ground surface suggests that the slope would not initially fail under initial drained conditions even if the water table raised to ground surface. The FS values for the two lowered WT scenarios suggest that the WT would need to exist somewhere between the top of the limestone interval and the center of the clay layer for the slope to become stable with soil on the failure plane at the residual drained strength value.

Table 4- 8: FS values at different water table elevations for B6 drained residual strength power curve parameters

Lower Water Table		
Location	FS Residual Drained Strength	FS Fully softened Drained Strength
Baseline WT	0.71	1.49
WT at Ground Surface	0.51	1.37
Baseline WT (-2m)	0.88	2.05
WT at Top of Limestone Interval	1.33	2.18

4.8.3 *Effect of Strength Gain on Failure Plane*

Previous research suggests that soil within a preexisting landslide failure plane may recover strength with time (e.g., D’Appolonia et al. 1967, Ramiah et al. 1973, Skempton 1985). Stark and

Hussain (2010) present data from previous researchers regarding the amount of strength recovery compared to residual drained shear strength values. The results presented by Stark and Hussain (2010) indicate that clay soils may recover 10% to 40% of the residual drained shear strength over a period of 3 days to 5 months. The amount of strength recovery has been shown to be greater for clays with a higher plasticity index (PI).

This section investigates the effect of strength recovery above the residual drained shear strength on stability of the slope using LEM analyses for the residual drained strength ring shear data from B6 using noncircular surfaces. The power curve parameter '*a*' is increased to achieve strength recovery of 20%, 30% and 40% for vertical stresses up to 150 kPa. The updated power curve fits for each strength recovery scenario are shown in Figure 4-15 along with the updated power curve relationships. The increase in strength is still significantly less than the FSS strength for these specimens. The associated FS values for each strength recovery scenario are compared to the residual strength FS in Table 4-9. FS values are shown to increase as strength is recovered on the assumed preexisting failure plane. A strength recovery of 40% produces a FS value fairly close to 1.

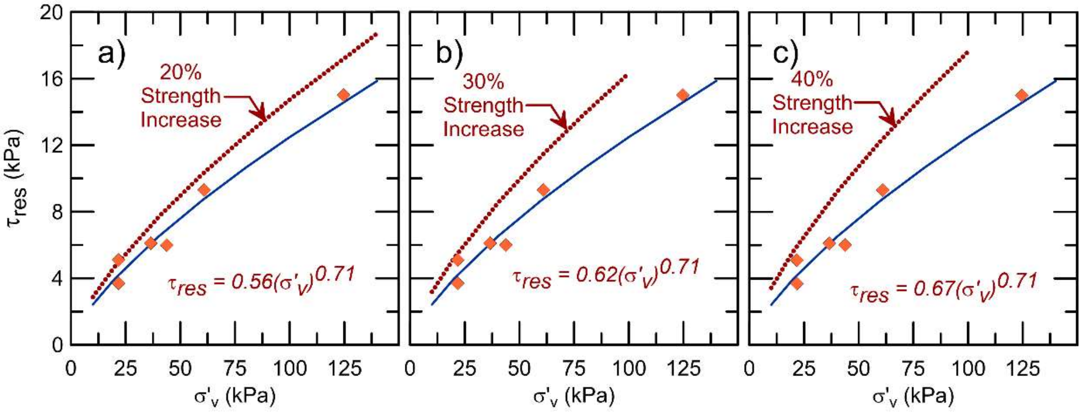

Figure 4- 15: Power curve fit for a drained residual shear strength increase of a) 20%; b) 30%; c) 40% for the B6 ring shear results

4.8.4 Combined Effect of Strength Recovery and Water Table Elevation

Lowering the WT and strength recovery have both been shown to increase the FS of the slope, but it is likely that these two effects would occur together, as a lowering of the WT due to seasonal fluctuations may lead to a reduction in movement and subsequent strengthening. The results for combining these two effects are also shown in Table 4-9 for a WT that is approximately 2 m lower than baseline. The critical circular and noncircular failure planes for this scenario are found to be fairly consistent with previous results except the toe of the failure planes breach the ground surface slightly upslope of the ALDOT ROW which was not observed in the field (Figure 4-16). The combined effect of a lower water table and strength recovery on the failure plane produce a stable slope for strength recovery values as low as 20%. These results suggest that slope movements may cease as the water table elevation decreases and strength is recovered on the preexisting failure plane. However, the relationship between decreasing the water table elevation and strength recovery on the failure is not well understood and requires further research.

Table 4- 9: Updated power curve parameters for strength recovery using drained residual strength ring shear results from B6 with FS values for elevated and lowered WT

	Strength Recovery $\tau = a(\sigma'_v)^b$			
Location	a	b	FS Noncircular Surfaces	FS (WT at Baseline -2m)
Residual Strength	0.47	0.71	0.71	0.88
20% Strength Recovery	0.56	0.71	0.81	1.01
30% Strength Recovery	0.62	0.71	0.88	1.10
40% Strength Recovery	0.67	0.71	0.94	1.17

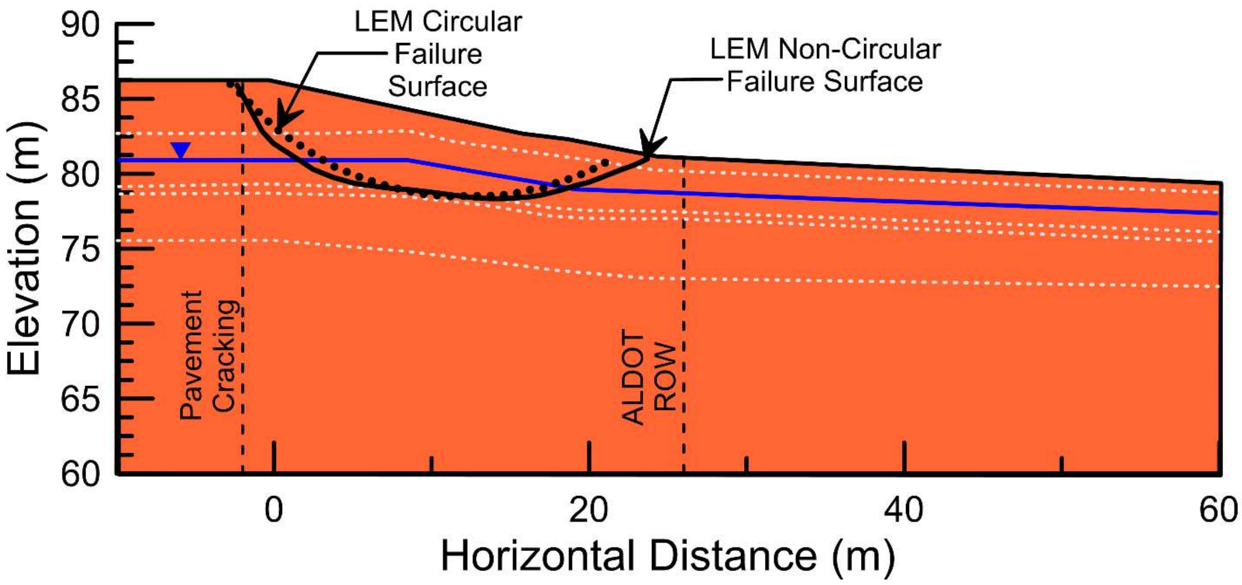

Figure 4- 16: Circular and noncircular failure surfaces for water table at center of upper clay layer and 20% strength recovery on the failure plane. Locations of ALDOT ROW and pavement cracking shown by dashed black lines. Soil layer boundaries shown by dotted light grey lines

4.8.5 Effect of Mesh Density on SRM Results

The effect of mesh density on calculated SRM FS values is analyzed by repeating the initial undrained failure analyses using a coarser and finer mesh with a peak undrained shear strength ratio ($S_{u,pk}/\sigma'_v$) of 0.21. The baseline (medium) mesh and WT (Figure 4-5) in this chapter uses element heights of 0.75 m. The coarse mesh uses element heights of 1.5 m and the fine mesh uses element heights of 0.25 m. The fine and medium mesh produce the same FS value indicating that the baseline (medium) mesh used in this study is sufficiently discretized. The coarse mesh produces a FS value of 1.28 which is significantly larger than the fine and medium meshes (Table 4-10). This increase in FS for the coarse mesh illustrates the importance of discretizing the mesh so that the solution would not be affected using smaller mesh sizes (e.g., Zablotonii et al. 2021). Accurate representation of the site model (Figure 4-5) is also difficult using the coarse mesh. The thickness of the thin limestone interval is limited to the element height of 1.5 m. Boundary locations and layer thickness for the clay and sand layers is also affected by the large element heights in the coarse mesh. Resolution of the site model also likely contributes to the increase in FS for the coarse mesh but further research is needed to confirm this.

Table 4- 10: Effect of mesh size on FS values in undrained SRM analyses with $S_{u,pk}/\sigma'_v = 0.21$

Mesh Size	FS
Coarse Mesh	1.28
Medium (Baseline) Mesh	1.02
Fine Mesh	1.02

4.9 DISCUSSION

This study provides guidance regarding the integration of electrical resistivity imaging (ERI) and multichannel analysis of surface waves (MASW) with traditional geotechnical explorations, lab tests, and site geology to characterize a landslide site for the purpose of slope stability analysis. Data from each investigation techniques are used to inform each other to produce a geologically based site model that is consistent with the collected data. ERI and MASW data are compared to borings and Atterberg limits to estimate site stratigraphy. Traditional geotechnical explorations alone require the engineer to interpolate between data points resulting in greater uncertainty due to the lower resolution of data collected at discrete points. A continuous representation of the soil layers encountered at the site can be confidently estimated from the ERI results after confirming the interpretations agree with results from MASW, borings and Atterberg limits.

MASW provides an estimate of elastic modulus via shear wave velocity for use in SRM analyses. A thin layer with a drop in shear wave velocity in the MASW results is also found to correspond to the critical failure plane obtained from slope stability analyses. The estimated site stratigraphy is also found to agree with local site geology which reports high plasticity clays and limestone in the vicinity of the landslide site. It should be noted that the stratigraphy at this site relatively simple and that more complex sites may require more interpretation. Additional testing locations and studies to quantify spatial variability (e.g., dell'Arciprete et al. 2011, DeJong et al. 2016) may also be required for accurate characterization of sites with high spatial variability in stratigraphy or properties.

Ring shear testing is performed to estimate drained fully softened (τ_{ff}) and residual (τ_{res}) strength envelopes for clay at the site. The ring shear results show a nonlinear strength envelope for the clay at low vertical effective stresses (20 to 40 kPa) corresponding to the in-situ stresses estimated for each ring shear sample location. Previous researchers (e.g., Jiang et al. 2003, VandenBerge et al. 2013, Xuan et al. 2021) illustrate the importance of using a nonlinear envelope, as opposed to a linear strength envelope, in slope stability analyses involving clay at low stresses. Drained shear strengths in this chapter are represented using a power function (LEM) or the MHB model (SRM) to account for observed nonlinearity from ring shear testing. The residual strength of the clay at this site is found to 2 to 3 times lower than the measured fully softened strength values.

The nonlinear drained strength envelopes are implemented in the SRM analyses using the Modified Hoek-Brown constitutive model. MHB is formulated to represent the strength of rocks and is not typically used for modeling soils. VandenBerge and McGuire (2019) used MHB in SRM analyses for a simple homogeneous slope and the rockfill shell of the Oroville Dam. Their calculated FS values are found to compare well with LEM analyses using power curves performed by previous researchers. The results of this study found FS values obtained using MHB to represent the nonlinear shear strength envelope of the clay in SRM compare well with the results from LEM analyses that used power curves. The MHB model therefore appears to be a practical tool for modeling nonlinear strength envelopes of clays, but further research is required to better understand the limitations of this approach.

The ongoing movements indicate that an initial failure occurred at some time in the past and a pre-existing failure plane is present within the foundation. The shear strength on the failure plane is likely at some value between τ_{res} and τ_{ff} (Stark and Hussain 2010), which is supported by the analyses presented in this chapter. Initial failure of the slope under drained conditions is determined to be unlikely due to the high FS values obtained from LEM and SRM analyses using τ_{ff}. Initial failure of the slope during undrained loading seems more plausible as the LEM analyses produced FS values below 1 and SRM analysis produced FS values slightly above or below 1 depending on the value of S_u used. LEM and SRM analyses using residual strengths produced FS values between 0.71 and 0.80 depending on the parameters used to represent τ_{res}. These low FS values support that additional slope movements may occur under drained loading with strength on the failure near τ_{res}. However, the low FS values suggest that more rapid slope movements may occur if soil in the preexisting failure plane sustains a strength near τ_{res}. Previous research suggests that soil in the failure may recover 40% of τ_{res} strength with time (e.g., Stark and Hussain 2010). Soil in the preexisting failure plane at the site therefore likely has a strength somewhere between τ_{res} and τ_{fss}.

LEM analyses are performed using circular and noncircular failure surfaces. The circular surfaces are shown to consistently produce higher FS values compared to noncircular surfaces. Circular failure surfaces in this study reasonably match the noncircular surfaces and the critical surface from SRM for the drained loading investigations but the maximum depth of the circular failure planes tend to be slightly shallower. The circular failure surfaces in the initial undrained failure investigation are much shallower than the noncircular LEM and SRM failure surfaces and are not consistent with site observations. These results illustrate that the constraint of a circular failure surface may misrepresent the critical surface; especially for more complex failures as discussed by previous researchers (e.g., Duncan 1996, Cheng 2003).

The results from SRM using MHB are compared to the noncircular failure surface results from LEM. SRM produces lower bound FS values for the initial drained failure investigation, but not for the residual drained failure investigations. Noncircular failures from LEM in the drained are in reasonable agreement with the critical failure planes determined from SRM suggesting that the LEM results producing lower bound FS values may actually be reliable. Differences in FS values may then be attributed to differences in the power curve representation of shear strength used for drained LEM analyses versus the drained MHB calibrations used with SRM. Noncircular surfaces in LEM also produce lower bound FS values compared to SRM for the initial undrained failure investigations even though each method utilizes a vertical shear stress ratio to represent undrained shear strength. The comparison of both methods illustrates that LEM and SRM each have benefits and limitations, but are both valid methods for determination of slope stability. LEM and SRM analyses should both be performed for a given case history for comparison of the results; particularly for cases where the friction angle is zero.

A limited sensitivity study is also performed to examine the effect of chosen model parameters. The effect of using a linear strength envelope, as opposed to a nonlinear strength envelope, is examined through LEM analyses with noncircular failure surfaces at residual strength conditions. A linear envelope is fit to the ring shear data over the range of stresses expected for the ring specimens collected from the site and implemented in LEM analyses using Mohr-Coulomb failure criterion with a cohesion intercept of zero. The resulting FS is slightly higher than the value using the power curve fit indicating that the linear fit overestimates the soil strength at low stresses.

The effect of WT elevation on slope stability is examined by varying the WT level in LEM analyses. The drained residual strength power curve from B6 is used to analyze stability of the slope in LEM under residual strength conditions once the WT drops to a lower elevation. The lowered WT increases the FS value to 0.89 compared to 0.71 using the elevated WT. These results indicate that slope may become more stable after an elevated WT from rain events has time to subside. This may partially explain why slope movements are not observed during dry periods. Strength recovery on the failure plane may also contribute to increased stability which is discussed next.

The effect of strength recovery on the failure plane is examined using power curve fits that provide shear strength values 20%, 30% and 40% greater than τ_{res}. FS values considering strength recovery range 0.81 to 0.94 compared to 0.71 for analyses utilizing τ_{res}. These results indicate the strength recovery along the failure may significantly increase FS values, but strength recovery alone may not be adequate to prevent further slope movement. The combined effect of strength recovery and a lowered WT are also investigated to determine if the combined effect may produce a stable slope. FS values considering strength recovery and a lowered WT produce FS values ranging from 1.02 to 1.19 for strength recovery increases ranging from 20% to 40%. These results suggest that the combined effect of strength recovery and lowering of the water table likely result in a stable slope condition. Wright et al. (2007) examine the effects of wetting and drying cycles on the peak drained strength of clay, but the relationship between strength recovery on a failure plane during wetting and drying cycles remains a topic of future research.

4.10 SUMMARY AND CONCLUSIONS

This chapter integrates geophysics with traditional geotechnical explorations, index tests, and lab testing to characterize a slow-moving landslide site in Alabama. The data from all sources are used to inform each other to build a site model for use in slope stability analyses. Geophysical results are shown to correspond well with boring information. ERI provides a continuous 2D profile, is shown to delineate the clay layer from the surrounding soil mass, and corresponds well with Atterberg limits of the fine grained layers. MASW helps delineate lower velocity soils in the failure mass from stiffer soils outside the soil mass and appears to identify a shear plane of lower velocity. The ERI and MASW can therefore be used to create a detailed model of the site with high confidence compared to interpolating between point data collected from the boring locations. ERI and MASW are reliable tools for estimating site stratigraphy but interpretation required integrating these results with results from other methods. Results from traditional geotechnical explorations (i.e., borings and SPT) and index test (i.e., Atterberg limits) and should be used to guide interpretation of geophysical results to arrive at an accurate estimate of site stratigraphy.

Ring shear testing is used to determine drained fully softened and residual shear strength for clay samples collected from boring B6 and B7. The drained fully softened and residual strength envelopes obtained from ring shear testing are shown to be nonlinear. A power curve is used to represent the nonlinear strength envelopes in LEM, and the Modified Hoek-Brown constitutive model is used to represent the nonlinear strength envelopes for SRM analyses in FLAC. FS values from LEM analyses using the power curve representation of shear strength are comparable to SRM analyses. The MHB model is therefore shown to provide a practical option for representing nonlinear strength envelopes of soils in SRM analyses. A linear strength envelope is also fit to ring shear data at low effective stresses and represented using the Mohr-Coulomb failure criterion in

LEM analyses. The linear analyses result in slightly higher FS values, but the difference is not significant. Linear envelopes may therefore provide a reasonable estimate of soil strength if they are fit to data in the effective stress range of interest. The use of a single linear envelope may not be appropriate for sites with large variations in effective stress.

Circular and noncircular failure surfaces are compared in LEM analyses. Circular surfaces are shown to produce slightly higher FS values compared to noncircular surfaces. Circular surfaces produced shallower failure planes than noncircular surfaces but are generally consistent with site observations when drained fully softened and residual strength envelopes are used. The difference between circular and noncircular surfaces is most prevalent when undrained shear strength is analyzed. Differences in FS values obtained using circular and noncircular surfaces are larger in the undrained analyses. The undrained circular failure plane is also observed to breach the ground surface on the face of the slope which is not consistent with site observations. The constraint of a circular failure surface in LEM may misrepresent the critical surface for cases involving more complex failure plane geometries as appears to be the case for the landslide studied in this chapter. This limitation is expected to be more significant involving undrained analyses where the friction angle is zero.

The results of LEM analyses are also compared to SRM analyses. SRM produces lower bound FS values for the initial drained failure investigation, but not for the residual drained failure, or peak undrained failure investigations. Itasca (2016) state that LEM should never produce a lower bound FS compared to SRM and suggest that LEM may be unreliable in cases where LEM provides a lower bound FS. This statement contradicts the findings in this study as well as the conclusions of Cheng et al. (2007). Noncircular LEM failure planes in this study sometimes produce slightly higher FS values compared to SRM, but the noncircular failure planes are generally consistent with the critical failure plane locations produced by SRM. The comparison of both methods illustrates that LEM and SRM are both valid methods for determination of slope stability. LEM and SRM analyses should both therefore be performed for a given case history for comparison of the results. This is particularly true for analyses where the friction angle is zero, such as modeling undrained loading.

The main objective is to understand the failure mechanism for this landslide. Repeated failure along a preexisting shear plane is assumed to occur at the site due to the recurrent movements observed. The time and mechanism of the initial failure causing the preexisting shear plane is not known. FS values obtained using the fully softened drained strengths envelopes indicate that initial failure likely did not occur under drained loading. FS values obtained using undrained shear strength ratios produce FS values just above or below 1 indicating that initial failure of the slope likely occurred under undrained loading, possibly shortly after construction. Analyses utilizing the residual drained strength envelopes produce FS values significantly lower than 1 indicating the slope to be unstable when soil on the failure plane exists at the residual state. The low FS values obtained using residual drained strengths suggest that more rapid deformations than observed in the field may be expected if the residual shear strength is sustained on the failure plane.

Clays at a residual state have been shown to recover strength with time. The effect of shear strength increase due to strength recovery on the failure plane is examined in this study using failure envelopes that produce shear strengths 20% to 40% greater than the measured residual values. Strength recovery on the failure plane is shown to significantly increase FS values, but the strength increase alone is not large enough to produce a stable slope. An elevated water table, compared to observed at the site is assumed for the analysis in this chapter to represent groundwater conditions after a rain event. The effect of lowering of the water table after a rain event on slope stability is also examined. Lowering of the water table increase FS values significantly but does not produce a stable slope. The combined effect of strength recovery and a lowered water table is also examined and is found to produce FS values greater than 1 indicating a stable slope.

The results of slope stability analyses indicate that the slope likely became unstable due to undrained loading. Continued movement of the slope observed after rain events likely occurs as the water table rises with drained shear strength on the failure plane somewhere between the residual and fully softened values. The combined effect of the WT elevation decreasing after rain events and strength recovery along the failure plane produces a stable slope during dry periods when movement is not observed. The relationship between strength recovery and changes in water table elevation are not well understood and remain a topic for future research.

CHAPTER 5: SUMMARY, CONCLUSIONS, PRACTICAL BENEFITS AND FUTURE RESEARCH

5.1 SUMMARY AND CONCLUSIONS

The potential for strength loss in fine grained soils poses a significant hazard for many geotechnical projects. Damage to infrastructure attributed to strain-softening of clayey soils has been documented in many case histories involving both static and cyclic loading. For critical infrastructure projects, potential deformations due to cyclic loading are increasingly being analyzed using nonlinear deformation analyses (NDAs). These analyses rely on constitutive models which can represent the aspects of soil behavior important to the problem being analyzed. Strain localization in NDAs presents additional modeling challenges including mesh size dependence. Simple methods to reduce mesh dependency are needed for use by practicing engineers.

Slow-moving landslides and embankment failures along roadways disrupt traffic and lead to repeated repair costs as the slopes continue to move. Limit Equilibrium Method (LEM) and Strength Reduction Method (SRM) analyses are typically performed for these cases which typically involve static loading. Limit equilibrium and strength reduction analyses each present their own benefits and limitations. Clays have also been observed to display nonlinear drained shear strength envelopes at low effective stresses making selection of strength parameters for slope stability analyses more challenging. Accurate characterization of a landslide site is key to building models for use in such analyses. Traditional geotechnical explorations provide data only at discrete points, but geophysical methods can provide continuous site profiles that can be interpreted with confidence when the results are confirmed using traditional explorations.

The primary objectives of this study are:

- Develop a procedure for calibrating the PM4Silt for strain-softening clays
- Validate the PM4Silt constitutive model against a well-documented case history of an earthquake-induced landslide in a sensitive clay deposit.
- Examine the ability of a displacement-based calibration procedure to reduce mesh dependency of the PM4Silt solution
- Identify differences in results for simulations using an advanced effective stress-based constitutive model and a total stress-based strain-softening model
- Use geophysical exploration tools to characterize a landslide in a strain-softening clay deposit
- Examine the ability of the Modified Hoek-Brown constitutive model to represent nonlinear drained strength envelopes in SRM analyses of a landslide underlain by strain-softening clay
- Compare stability analysis methods for static landslides in strain-softening clays.

Chapter 2 evaluates the ability of the PM4Silt constitutive model to reproduce deformations at the Fourth Avenue Landslide site. Fourth Avenue simulation results using the proposed PM4Silt calibration procedure are generally consistent with the observed deformations when using peak and residual strengths that are slightly below the average values from laboratory tests. A limited sensitivity study is performed to investigate the effects of changing the strength of the BCC, the rate of softening, the input motion, and the mesh size on the final displacements. The results follow expected trends, with higher displacements occurring for lower peak and residual strengths, faster softening rates, and more intense ground motions. The solution is observed to be mesh dependent with finer meshes tending to show larger displacements. Differences in displacements from simulations using different mesh sizes can be reduced by ensuring the calibrations are performed with the same size elements as will be used in the simulations. This may not be practical in all circumstances (i.e., irregular meshes) and does not address all aspects of mesh dependency, so future users must be aware of the effects of mesh dependence if their simulation has significant softening.

Chapter 3 compares the ability of the effective stress-based PM4Silt constitutive model versus a total stress-based model (RSSMC) to represent aspects of cyclic softening at the element and field scale level. PM4Silt produced a more realistic nonlinear stress-displacement curve in undrained monotonic loading. RSSMC produced a piecewise linear representation of stress and displacement which made it difficult to accurately match nonlinear stress-displacement curves observed in strain-softening clays. Both models are able to reasonably match modulus reduction and damping ratio curves in the calibration drivers, but RSSMC requires additional hysteretic and stiffness-proportional Rayleigh damping. Failure to include appropriate damping with the RSSMC model in the field-scale simulations results in delayed softening (no hysteretic damping) or suppressed yielding of BCC in the failure zone (mass-proportional Rayleigh damping included). The effective stress-based PM4Silt model produces generation of excess pore pressure and changes in effective stress and strength in both the single element and field-scale simulations. The total stress-based RSSMC model produces stress paths which are relatively independent of changes in effective stress and do not generate excess pore pressure within the failure zone in field-scale simulations. Both models produced reasonable deformation patterns and magnitudes within the Fourth Avenue failure mass, but PM4Silt produces small deformations outside of the failure mass as is observed in the field. RSSMC displays almost zero ground displacement outside of the primary failure mass.

This chapter also examines the ability of the displacement-based calibrations to reduce mesh dependency of the PM4Silt solution. The displacement-based calibration is shown to produce consistent upper crest displacement magnitudes using different mesh sizes, but previous research suggests that final displacement magnitudes are primarily dependent on the residual strength (Chapter 2). The displacement-based calibration allows BCC elements of different heights to fully soften under similar displacement magnitudes but does not eliminate other aspects of mesh depnedency including resolution and shape of the failure plane. Practicing engineers may use the displacement-based to calibration approach to reduce mesh dependency in simulations involving strain-softening clays but should be aware that other aspects of mesh dependence may still exist.

One main goal of Chapter 3 is to provide guidance as to when it may be necessary to use more advanced effective stress-based models (e.g., PM4Silt) versus total stress-based models (e.g., RSSMC). The results in this study suggest that advanced effective stress-based models may be necessary if element level response or a more complete estimation of ground deformation patterns both inside and outside of the failure mass are important to the scenario being modeled. Simple total stress-based models may be adequate if the user is primarily interested in whether failure will occur but were not able to capture intermediate deformation cases. Total stress-based models are often described as easier to calibrate, but this study showed that calibration to modulus reduction and damping behavior is more complicated for the RSSMC model and had a significant influence on field-scale results. The brittle failure modes observed with RSSMC showed that sensitivity studies to examine the effect of chosen strength and softening parameters are more critical for the

RSSMC model. Mesh dependency is an important consideration regardless of the type of constitutive model and should be included in sensitivity studies.

Chapter 4 uses electrical resistivity imaging (ERI) and multichannel analysis of surface waves (MASW) combined with traditional geotechnical explorations and lab testing to characterize a landslide site along an interstate in Alabama. The data from all sources are used to inform each other to build a site model for use in slope stability analyses. Electrical resistivity results are shown to correspond well with boring information and Atterberg limits of the fine grained layers. MASW helps delineate lower velocity soils in the failure mass from stiffer soils outside the soil mass and appears to identify a shear plane with lower velocity. The continuous 2D ERI profile and MASW results can therefore be used to create a detailed model of the site with high confidence compared to interpolating between point data collected from the boring locations. ERI and MASW are reliable tools for estimating site stratigraphy but should not be the only tool used. Results from traditional geotechnical explorations (i.e., borings and SPT) and index test (i.e., Atterberg limits) and should be used to guide interpretation of geophysical results to arrive at an accurate estimate of site stratigraphy.

Ring shear testing is used to determine drained fully softened and residual shear strength for clay samples collected from boring B6 and B7. The drained fully softened and residual strength envelopes obtained from ring shear testing are shown to be nonlinear. A power curve is used to represent the nonlinear strength envelopes in LEM, and the Modified Hoek-Brown constitutive model is used to represent the nonlinear strength envelopes for SRM analyses in FLAC. FS values from LEM analyses using the power curve representation of shear strength are found comparable to SRM analyses. The Modified Hoek-Brown model therefore seems a practical option for representing the drained shear strength of clays at low effective stresses. A linear strength envelope is also fit to ring shear data at low effective stresses and represented using the Mohr-Coulomb failure criterion in LEM analyses. The linear envelope analyses result in slightly higher, yet comparable, FS values indicating that linear envelopes may be sufficient if they are fit over an appropriate range of effective stresses for soils at the site. However, linear envelopes may not be appropriate for sites with larger effective stress ranges in critical soils beneath the slope.

Circular and noncircular failure surfaces are compared in LEM analyses. Circular surfaces are shown to produce slightly higher FS values compared to noncircular surfaces. Circular surfaces produce shallower failure planes than noncircular surfaces but are generally consistent with site observations when drained fully softened and residual strength envelopes are used. The difference between circular and noncircular surfaces is most prevalent when undrained shear strength is analyzed. The location of the failure plane in the undrained analyses is also not consistent with site observations. The constraint of a circular failure surface in LEM may misrepresent the critical surface for cases involving more complex failure plane geometries as appears to be the case for the landslide studied in this chapter. This limitation is expected to be more significant involving undrained analyses where the friction angle is zero.

The results of LEM analyses are also compared to SRM analyses. SRM produces lower bound FS values for the initial drained failure investigation, but not for the residual drained failure, or peak undrained failure investigations. Noncircular failure planes in LEM sometimes produce slightly higher FS values compared to SRM, but the noncircular failure planes are generally consistent with the critical failure plane locations produced by SRM. The comparison of both methods illustrates that LEM and SRM are both valid methods for determination of slope stability. LEM and SRM analyses should both therefore be performed for a given case history for comparison of the results. This is particularly true for analyses where the friction angle is zero, such as modeling undrained loading.

The main objective is to understand the failure mechanism for this landslide. The time and mechanism of the initial failure causing the preexisting shear plane at this site is not known. FS values obtained using the fully softened drained strengths envelopes indicate that initial failure likely did not occur under drained loading. FS values obtained using undrained shear strength ratios produce FS values just above or below 1 indicating that initial failure of the slope likely occurred under undrained loading, possibly shortly after construction. Analyses utilizing the residual drained strength envelopes produce FS values significantly lower than 1 indicating the slope to be unstable when soil on the failure plane exists at the residual state. The low FS values obtained using residual drained strengths suggest that more rapid deformations than observed in the field may be expected if the residual shear strength is sustained on the failure plane. Sensitivity analyses suggest that the combined effect of lowering the water table and strength gain over time may stabilize the slope, but additional work is needed to understand how these two factors interact.

5.2 DISCUSSION ON PRACTICAL BENEFITS OF RESEARCH

This dissertation provides specific conclusions regarding site characterization and analysis of landslides involving strain-softening clays. This section describes the practical application of these conclusions to a wider range of geotechnical problems faced by practicing engineers. PM4Silt is shown capable of reproducing deformation patterns and magnitudes at the Fourth Avenue Landslide site. PM4Silt is only validated for this single case history in the current study but this sets up the possibility for further validation of the model needed to provide practicing engineers a reliable choice for modeling cyclic softening of clays over a broad range of loading scenarios and problem geometries.

The effective stress-based PM4Silt model is shown to be a better option for estimating deformations patterns outside of the major failure mass and produced a more realistic response at the element level compared to the total stress-based RSSMC model. The comparisons drawn in this dissertation are specific to the constitutive models chosen, but they do provide a baseline for practicing engineers to understand general differences between total and effective stress-based models and help them to select an appropriate constitutive model for a given project. The displacement-based calibration procedure is shown to reduce mesh size dependence in PM4Silt. The displacement-based procedure is a relatively simple regularization option that can be implemented during calibration and does not require any modification to the model formulation. This provides an available option for engineers to reduce mesh dependence using PM4Silt. The displacement-based calibration procedure may also reduce mesh dependency in other constitutive models, but this remains a topic of study for future researchers.

ERI and MASW results are shown to correspond well with geotechnical explorations and characteristics of the failure mass were consistent with previous research (e.g., Jongmans and Garambois 2007, Perrone et al. 2014). Embankment failures in compacted clay fills along roadways are common in many areas (Wright et al. 2007). The results of the integrated characterization in this study provide an example of how geophysics can be incorporated with traditional geotechnical explorations to develop models for such sites that can be used in slope stability analyses. This information should benefit engineers and department of transportation personnel.

The MHB model is shown to be a practical method for representing nonlinear drained strength envelopes of clays in SRM analysis. Commercial FEM and FDM software typically include very few options for representing soil strength in SRM analyses. For example, in FLAC V8.0 SRM analyses must be performed using the Mohr-Coulomb, or the Mohr-Coulomb derived, ubiquitous joint or MHB model. The MHB model may therefore be a practical option for engineers to represent nonlinear drained strength envelopes in SRM analyses.

5.3 FUTURE RESEARCH

PM4Silt is shown to reasonably reproduce deformation patterns in simulations of the Fourth Avenue landslide. Further validation of PM4Silt on the utilized calibration approach are needed using additional case histories and lab tests. A displacement-based calibration approach is shown to reduce, but not eliminate, mesh dependency in PM4Silt. Additional research is needed to better understand the benefits and limitations of the displacement-based calibration procedure. The Modified Hoek-Brown (MHB) constitutive model is shown to be a practical option for representing drained shear strength of clays in strength reduction analyses. Additional studies in SRM analyses and NDAs are needed to better understand the benefits and limitations of the MHB model for representing drained strength of clays in slope stability analyses. Slope stability analyses of the Alabama landslide site indicate that the slope is only stable after strength recovery occurs and the water table is lowered. The relationship between strength recovery on a failure plane and fluctuations in water table elevation is not well understood and should be studied further.

CHAPTER 6: REFERENCES

Advanced Geosciences Inc. (AGI), 2014, EarthImager 2D Manual, Austin, TX.

Alabama Tombigbee Regional Commission (ATRC). (2014). "Conecuh County Hazard Mitigation Plan." *Alabama Tombigbee Regional Commission*.

Aylsworth, J.M., and Lawrence, D.E. (2003). "Earthquake-induced landsliding east of Ottawa; a contribution to the Ottawa Valley Landslide Project." *In Proceedings of the 3rd Canadian Conference on Geotechnique and Natural Hazards*, Edmonton, Alberta, pp. 77–84.

Anastasopoulos, I., Gazetas, G., Bransby, M. F., Davies, M. C., and El Nahas, A. (2007). "Fault rupture propagation through Sand: Finite-element analysis and validation through centrifuge experiments." *Journal of Geotechnical and Geoenvironmental Engineering*, 133(8), 943–958.

Ancheta, T.D., Darragh, R.B., Stewart, J.P., Seyhan, E., Silva, W.J., Chiou, B. S.-J., Wooddell, K. E., Graves, R.W., Kottke, A.R., Boore, D.M., Kishida, T., and Donahue, J.L. (2013). "PEER NGA-West2 database." *PEER Report No. 2013/03*, Pacific Earthquake Engineering Research Center, University of California, Berkeley, CA, 134 pp

Andresen, L. and Jostad, H.P. (1998). "Effect of strain-softening in interpretation of laboratory compression tests." *Application of Numerical Methods to Geotechnical Problems*, Springer; 223-232.

Andresen, L. and Jostad, H.P. (2005). "ANISOFT – Constitutive Model for Undrained Loading of Anisotropic and Strain-Softening Clay." *Proc. Geo-Frontiers Congress 2005*, Austin, Texas.

ASTM D2573 / D2573M-18. (2018). "Standard Test Method for Field Vane Shear Test in Saturated Fine-Grained Soils." ASTM International, West Conshohocken, PA

ASTM D6467-13e. (2018). “Standard Test Method for Torsional Ring Shear Test to Determine Drained Residual Shear Strength of Fine-Grained Soils.” ASTM International, West Conshohocken, PA

ASTM D7608-18. (2018). “Standard Test Method for Torsional Ring Shear Test to Measure Drained Fully Softened Shear Strength and Stress Dependent Strength Envelope of Fine-Grained Soils.” ASTM International, West Conshohocken, PA

Atkinson, J. (2007). “Peak strength of overconsolidated clays.” *Géotechnique*, 57(2), 127–135.

Baglari, D., Dey, A., and Taipodia, J. (2018). “A state-of-the-art review of passive MASW survey for subsurface profiling.” *Innovative Infrastructure Solutions*, 3(1).

Basu, D. (2021). “Numerical Modeling of Liquefaction-induced Settlement due to Reconsolidation.” Ph.D. Dissertation, Auburn University, Auburn, AL, USA.

Baker, R. (2004). “Nonlinear Mohr envelopes based on triaxial data.” *Journal of Geotechnical and Geoenvironmental Engineering*, 130(5), 498–506.

Beaty, M.H. and Byrne, P.M. (2011). "UBCSAND constitutive model: version 904aR." *Documentation report on Itasca UDM Web Site*, February 2011

Beaty, M.H. and Dickenson, S.E. (2015). “Numerical Analysis for Seismically-Induced Deformations in Strain-Softening Plastic Soils.” *Proc. 6th Intern. Conference on Earthquake Geotechnical Engineering*, Christchurch, NZ.

Biscontin, G. and Pestana, J. M. (2001). “Influence of Peripheral Velocity on Vane Shear Strength of an Artificial Clay,” *Geotechnical Testing Journal* Vol. 24, No. 4, pp. 423–429.

Bjerrum, L., and Landva, A. (1966). “Direct simple-shear tests on a Norwegian quick clay.” *Géotechnique*, 16(1), 1–20.

Boulanger, R.W., Meyers, M.W., Mejia, L.H., and Idriss, I.M. (1998). “Behavior of a fine-grained soil during the Loma Prieta earthquake.*” Canadian Geotechnical Journal*, V35, 146-158.

Boulanger, R.W. and Idriss I.M. (2004) “Evaluating the potential for liquefaction or cyclic failure of silts and clays.” *Report UCD/CGM-04/01*, Center for Geotechnical Modeling, University of California, Davis.

Boulanger, R. W., and Idriss, I. M. (2007). "Evaluation of cyclic softening in silts and clays." *J. of Geotech. and Geoenvir. Eng.*, 10.1061/(ASCE)1090-0241(2007)133:6(641).

Boulanger, R.W. and Ziotopoulou, K. (2017). “PM4Sand (version 3.1): A sand plasticity model for earthquake engineering applications.” *Report No. UCD/CGM-17/01*, Center for Geotechnical Modeling, Department of Civil and Environmental Engineering, University of California, Davis, CA, March, 112 pp.

Boulanger, R.W. and Ziotopoulou, K. (2018). “PM4Silt (Version 1): A silt plasticity model for earthquake engineering applications.” *Report No. UCD/CGM-18/01*, Center for Geotechnical Modeling, Department of Civil and Environmental Engineering, University of California, Davis, CA.

Bowles, J.E. (1996). *Foundation Analysis and Design*. 5th edn. McGraw-Hill, Singapore.

Brinkgreve, R.B.J. (1994). “Geomaterial models and numerical analysis of softening.” PhD thesis. Delft University of Technology, Netherlands.

Burland, J. B. (1990). “On the compressibility and shear strength of natural clays.” *Géotechnique*, 40(3), 329–378.

Caracciolo, D., Arnone, E., Conti, F. L., and Noto, L. V. (2017). “Exploiting historical rainfall and landslide data in a spatial database for the derivation of critical rainfall thresholds.” *Environmental Earth Sciences*, 76(5).

Carrier, W. D., and Beckman, J. F. (1984). "Correlations between index tests and the properties of remoulded clays." *Géotechnique*, 34(2), 211–228.

Casey, B., and Germaine, J. T. (2013). "Stress dependence of shear strength in fine-grained soils and correlations with liquid limit." *Journal of Geotechnical and Geoenvironmental Engineering*, 139(10), 1709–1717.

Castellanos, B.A., Brandon, T.L., VandenBerge, D.R. (2016). "Use of fully softened shear strength in slope stability analysis." *Landslides.* 13, 697–709

Center for Eng. Strong Motion Data (CESMD) (2017). <http://www.strongmotioncenter.org/> (Jun. 17, 2017).

Chaudhary, B., Hazarika, H., and Krishan, A. M. (2016). "Effect of backfill reinforcement on retaining wall under dynamic loading." *Geotechnical Hazards from Large Earthquakes and Heavy Rainfalls*, 535–544.

Chen, C.-Y., and Martin, G. R. (2002). "Soil–structure interaction for landslide stabilizing piles." *Computers and Geotechnics*, 29(5), 363–386.

Cheng, Y. M. (2003). "Location of critical failure surface and some further studies on slope stability analysis." *Computers and Geotechnics*, 30(3), 255–267.

Cheng, Y. M., Lansivaara, T., and Wei, W. B. (2007). "Two-dimensional slope stability analysis by limit equilibrium and strength reduction methods." *Computers and Geotechnics*, 34(3), 137–150.

Cho, S. E. (2009). "Infiltration analysis to evaluate the surficial stability of two-layered slopes considering rainfall characteristics." *Engineering Geology*, 105(1-2), 32–43.

Collins, B. D., and Znidarcic, D. (2004). "Stability analyses of rainfall induced landslides." *Journal of Geotechnical and Geoenvironmental Engineering*, 130(4), 362–372.

Constable, S.C., Parker, R.L. and Constable, C.G. (1987). “Occam’s inversion: A practical algorithm for generating smooth models from electromagnetic sounding data.” *Geophysics*, 52, 289–300

Cook, M., Baker, R. M., Henderson, P., McGregor, S., and Moss, N. (2004). “Conecuh-Sepulga-Blackwater Rivers Watershed Protection Plan.” Alabama Geologic Survey. Tuscaloosa, Alabama, USA

Cunningham, M. R., Ridley, A. M., Dineen, K., and Burland, J. B. (2003). “The mechanical behaviour of a reconstituted unsaturated silty clay.” *Géotechnique*, 53(2), 183–194.

Dafalias, Y.F. and Manzari, M.T. (2004). "Simple plasticity sand model accounting for fabric change effects." *J. of Eng. Mech.,* 10.1061/(ASCE)0733-9399(2004)130:6(622).

D’Appolonia, E., Alperstein, R., and D’Appolonia, D. J. (1967). “Behavior of a colluvial slope.” *J. Soil Mech. and Found. Div.*, 93(4), 447–473.

Degroot-Hedlin, C., and Constable, S., (1990). “Occam’s inversion to generate smooth, two-dimensional models from magnetotelluric data.” *Geophysics*, 55(12), 1613–1624.

DeJong, J. T., Sturm, A. P., and Ghafghazi, M. (2016). “Characterization of gravelly alluvium.” *Soil Dynamics and Earthquake Engineering*, 91, 104–115.

dell’Arciprete, D., Bersezio, R., Felletti, F., Giudici, M., Comunian, A., and Renard, P. (2011). “Comparison of three geostatistical methods for hydrofacies simulation: A test on alluvial sediments.” *Hydrogeology Journal*, 20(2), 299–311.

Dawson, E. M., Roth, W. H., and Drescher, A.(1999). ‘‘Slope stability analysis by strength reduction.’’ *Geotechnique*, 49~6, p. 835– 840.

Diaz-Rodriguez, J.A., Martinez-Vasquez, J.J., and Santamarina, J.C. (2009). "Strain-rate effects in Mexico City soil." *Journal of Geotechnical and Geoenvironmental Engineering*, Vol. 135, No. 2, pp 300-305.

Duncan, J. M. (1996). “State of the art: Limit equilibrium and finite-element analysis of slopes.” *Journal of Geotechnical Engineering*, 122(7), 577–596.

Duncan, J.M., Wright, S.G., and Brandon, T.L. (2014), *Soil Strength and Slope Stability*. John Wiley. Hoboken, N. J.

Elgamal, A., Yang, Z., and Parra, E. (2002). “Computational modeling of cyclic mobility and post-liquefaction site response”. *Soil Dynamics and Earthquake Eng*., 10.1016/S0267-7261(02)00022-2

Fine, I.V., Rabinovich, A.B., Bornhold, B.D., Thomson, R.E., and Kulikov, E.A. (2005). “The Grand Banks landslide-generated tsunami of November 18, 1929: preliminary analysis and numerical modeling.” *Marine Geololgy,* 215 (1) (2005), pp. 45-57

Gao, L., Xia, J., Pan, Y., and Xu, Y. (2015). “Reason and condition for mode kissing in MASW method.” *Pure and Applied Geophysics*, 173(5), 1627–1638.

Gaviglio, P. (1989). “Longitudinal waves propagation in a limestone: The relationship between velocity and density.” *Rock Mechanics and Rock Engineering*, 22(4), 299–306.

Geologic Survey of Alabama (GSA). (2010). *GSA website*, <https://www.gsa.state.al.us/gsa/geologic/hazards/sinkholes> (Oct. 11, 2021).

Ghorbani, A., Jahanpour, R., and Hasanzadehshooiili, H. (2019). “Evaluation of liquefaction potential of marine sandy soil with piles considering nonlinear seismic soil–pile interaction; a simple predictive model.” *Marine Georesources & Geotechnology*, 38(1), 1–22.

Giannecchini, R., Galanti, Y., and D'Amato Avanzi, G. (2012). “Critical rainfall thresholds for triggering shallow landslides in the Serchio River Valley (Tuscany, Italy).” *Natural Hazards and Earth System Sciences*, 12(3), 829–842.

Gregersen, O. (1981). “The quick clay landslide in Rissa, Norway; The sliding process and discussion of failure modes.” *Proc. International Conference on Soil Mechanics and Foundation Engineering*, 10. Stockholm 1981. Proceedings, Vol. 3, pp. 421-426.

Griffiths, D.V., and Lane, P.A. (1999). ‘‘Slope stability analysis by finite elements.’’ *Geotechnique*, 49-3, p. 387–403.

Gylland, A.S., Jostad, H.P., and Nordal, S. (2014). “Experimental study of strain localization in sensitive clays”. *Acta Geotechnica*, *9*(2), 227-240.

Hansen, W.R. (1965). “The Alaska Earthquake, March 27, 1964 -- Effects on Communities.” *Geological Survey Professional Paper 542-A*, US Dept. of the Interior, Geological Survey.

Henkel, D. and Skempton, A. (1955). “A landslide at Jackfield, Shropshire, in a heavily over-consolidated clay.” *Géotechnique*, 5(2), pp.131-137.

Heritage, R.J. (2013). “Cyclic softening case study: Wendover Retirement Village.” *Proc. 19th NZGS Geotechnical Symposium*, Christchurch, Queensland.

Holtz, R.D. and Kovacs, W.D. (1981). *“An Introduction to Geotechnical Engineering.”* Prentice Hall, Englewood Cliffs, NJ, USA.

Holtz, R. D., Kovacs, W. D., and Sheahan, T. C. (2013). *An introduction to geotechnical engineering*. Pearson, Upper Saddle River, NJ.

Hoek, E., Carranza-Torres, C., Corkum, B. (2002). “Hoek-brown failure criterion—2002 edition.” In: *Proceedings of 5th North American rock mechanics 17th tunnelling association of Canada conference NARMS-TAC*, pp 267–273

Hyodo, M., Hyde, A. F. L., Yamamoto, Y., and Fujii, T. (1999). "Cyclic shear strength of undisturbed and Remoulded Marine Clays." *Soils and Foundations*, 39(2), 45–58.

Ichinose, G., Somerville, P., Thio, H. K., Graves, R., and Oconnell, D. (2007). "Rupture process of the 1964 Prince William Sound, Alaska, earthquake from the combined inversion of seismic, tsunami, and geodetic data." *Journal of Geophysical Research*, 112(B7)

Idriss, I.M. (1985). "Evaluating seismic risk in engineering practice." *Proc. 11th Int. Conf. on Soil Mech. and Found. Eng.,* San Francisco, CA. 255-320.

Idriss, I.M. and Boulanger, R.W. (2008). "Soil liquefaction during earthquakes." *Monograph MNO-12, Earthquake Engineering Research Institute*. Oakland: CA.

Itasca. (2016). FLAC, "Fast lagrangian analysis of continua." Version 8.0. Itasca Consulting Group, Minneapolis, MN, 2017.

Jamiolkowski, M., Ladd, C.C., Germaine, J.T., and Lancellotta, R. (1985). "New developments in field and laboratory testing of soils." *Proc. 11th Int. Conf. on Soil Mechanics*. 57-153. San Francisco, CA.

Jiang, J.-C., Baker, R., and Yamagami, T. (2003). "The effect of strength envelope nonlinearity on slope stability computations." *Canadian Geotechnical Journal*, 40(2), 308–325.

Jongmans, D., and Garambois Stéphane. (2007). "Geophysical investigation of landslides : A Review." *Bulletin de la Société Géologique de France*, 178(2), 101–112.

Jostad, H.P. and Andresen, L. (2004). "Modeling of shear band propagation in clays using interface elements with finite thickness." *Proc. 9th international symposium on numerical models in geomechanics*, NUMOG IX, Ottawa, Canada, pp. 121–128.

Jostad, H.P., Andresen, L., and Thakur, V. (2006). “Calculation of shear band thickness in sensitive clays.” *6th Numerical methods in geotechnical engineering NUMGE*, H Schweiger Eds, Austria, pp: 27-32

Kayyal, M.K., Wright S.G. (1991). “Investigation of long-term properties of Paris and Beaumont Clays in earth embankments.” Center for Transportation Research, University of Texas at Austin, Austin

Kennedy, L. (2019). “Drained Residual Strength of Expansive Soils Causing Pavement Distress Along Alabama Highway 5.” M.S. Thesis, Auburn University.

Kiernan, M. and Montgomery, J. (2018). “Numerical simulations of the Fourth Avenue landslide considering strain-softening.” *Proc. Geotechnical Earthquake Engineering and Soil Dynamics V*, Austin, TX.

Kiernan, M. (2019). “Numerical Simulations of the Fourth Avenue Landslide Considering Cyclic Softening.” Master’s Thesis. Auburn University

Kutter, B.L. and R.G. James (1989) "Dynamic centrifuge model tests on clay embankments." *Geotechnique*, Vol. 39, No. 1, pp 91-106.

Ladd, C. C., and Foott, R. (1974). “New design procedure for stability of soft clays.” *Journal of the Geotechnical Engineering*, 100(7), 763–786.

Lefebvre, G. and Leboeuf, D. (1987) "Rate effects and cyclic loading of sensitive clays." *Journal of Geotechnical Engineering*, Vol. 113, No. 5, pp 476-489.

Lefebvre, G. and Pfendler, P. (1996) "Strain rate and preshear effects in cyclic resistance of soft clay." *Journal of Geotechnical Engineering*, Vol. 122, No. 1, pp 21-26.

L'Heureux Jean-Sébastien, Locat, A., Leroueil, S., Demers, D., and Locat, J. (2014). *Landslides in sensitive clays: From geosciences to risk management*. Springer, Dordrecht.

Lim A., Ou, C., and Hsieh, P. (2010). “Evaluation of clay constitutive models for analysis of deep excavation under undrained conditions.” *Journal of Geoengineering*. 5(1), 9–20.

Lin, C.P., Chang, C.C., and Chang, T.S. (2004). “The use of MASW method in the assessment of soil liquefaction potential.” *Soil Dynamics and Earthquake Engineering*, 24(9-10), 689–698.

Locat, A., Locat, P., Demers, D., Leroueil, S., Robitaille, D., and Lefebvre, G. (2017). “The Saint-Jude landslide of 10 May 2010, Quebec, Canada: Investigation and characterization of the landslide and its failure mechanism.” *Canadian Geotechnical Journal*, 54(10), 1357–1374.

Loke, M.H., (2004). “Tutorial: 2-D and 3-D Electrical Imaging Surveys: Geotomo Software.” www.geoelectrical.com.

Manzari, M.T. and Dafalias, Y.F. (1997). "A critical state two-surface plasticity model for sand." *Géotechnique*, 47(2), 255-272.

Martelloni, G., Segoni, S., Fanti, R., and Catani, F. (2011). “Rainfall thresholds for the forecasting of landslide occurrence at regional scale.” *Landslides*, 9(4), 485–495.

Mayne, P. W. (1985). “A review of undrained strength in direct simple shear.” *Soils and Foundations*, 25(3), 64–72.

Mayne, P. (2001). “Stress-strain-strength-flow parameters from enhanced in-situ tests.” International Conference on In-Situ Measurement of Soil Properties & Case Histories [In-Situ 2001]. Bali, Indonesia. 27–48.

Mavroeidis, G.P., Zhang, B., Dong, G., Papageorgiou, A.S., Dutta, U., and Biswas, N.N. (2008). “Estimation of strong ground motion from the great 1964 Mw 9.2 Prince William Sound, Alaska, earthquake.” *Bulletin of the Seismological Society of America*, 98(5), 2303–2324.

McVay, M. C., Townsend, F. C., and Williams, R. C. (1992). “Design of socketed drilled shafts in Limestone.” *Journal of Geotechnical Engineering*, 118(10), 1626–1637.

Mesri, G. (1989). “A reevaluation of $S_{u(mob)} = 0.22\sigma'_p$ using laboratory shear tests.” *Canadian Geotechnical Journal*, 26(1), 162–164.

Meyerhof, G.G. (1976). “Bearing capacity and settlement of pile foundations.” 11th Terzaghi Lecture. *Journal of Geotechnical Engineering*. Div. Am. Sot. Civ. Engrs 102, GT3, 195-228

Mohammadi, S., and Taiebat, H. (2016). “Finite element simulation of an excavation-triggered landslide using large deformation theory.” *Engineering Geology*, 205, 62–72.

Montgomery, J. (2015). “Issues in nonlinear deformation analyses of embankment dams affected by liquefaction.” Ph.D. Dissertation, University of California, Davis, Davis, CA, USA.

Montgomery, J., Jackson, D., Kiernan, M., and Anderson, J. B. (2020). “Use of Geophysical Methods for Sinkhole Exploration.” Highway Research Center, *ALDOT Report 930-945*, Alabama Department of Transportation.

Moriwaki, Y., Vicente,E.E., Lai, S.S., Moses, T.L. (1985), "A reevaluation of the 1964 "L" street slide.” *Final Report*, State of Alaska, Department of Transportation and Public Facilities

Moug, D.M., Boulanger, R.W., DeJong J.T., and Jaeger, R.A. (2019) “Axisymmetric simulations of cone penetration in saturated clay.” *J. of Geotech. and Geoenvir. Eng.,* 145 (4)

Nakamura, S., Wakai, A., Umemura, J., Sugimoto, H., and Takeshi, T. (2014). “Earthquake induced landslides: Distribution, motion and mechanisms.” *Soils and Foundations*, 54(4), 544–559.

Nath, S.K., Chatterjee, D., Biswas, N.N., Dravinski, M., Cole, D.A., Papageorgiou, A., Rodriguez, J.A., and Poran, C.J. (1997). “Correlation study of shear wave velocity in near surface geological formations in Anchorage, Alaska.” *Earthquake Spectra*, 13(1), 55–75.

National Climatic Data Center (NCDC). (2005). “*Storm Data and Unusual Weather Phenomena*.” United States Department of Commerce.

National Oceanic and Atmospheric Administration (NOAA) (2005). National Weather Prediction Center (WPC) website. https://www.wpc.ncep.noaa.gov/tropical/rain/arlene2005.html (Oct. 11, 2021).

Oathes, T. J. and Boulanger, R. W. (2020). “Influence of Strain-Rate on Localization and Strain-Softening in Normally Consolidated Clays with Varying Strength Profiles.” *Proc., Geo-Congress 2020: Modeling, Geomaterials, and Site Characterization,* ASCE, 247-255.

Oka, F., Shahbodagh, B., and Kimoto, S. (2018). “A computational model for dynamic strain localization in unsaturated elasto-viscoplastic soils.” *International Journal for Numerical and Analytical Methods in Geomechanics*, 43(1), 138–165.

Park, C. B., Miller, R. D., and Xia, J. (1999). “Multichannel analysis of Surface Waves.” *Geophysics*, 64(3), 800–808.

Park, C. B., and Miller, R. D. (2008). “Roadside passive multichannel analysis of Surface Waves (MASW).” *Journal of Environmental and Engineering Geophysics*, 13(1), 1–11.

Park, C. B., and Carnevale, M. (2010). “Optimum MASW survey—revisit after a decade of use.” *GeoFlorida 2010*.

Park, D.S. (2011). “Strength loss and softening of sensitive clay slopes.” Doctoral Dissertation. University of California, Davis.

Perrone, A., Lapenna, V., and Piscitelli, S. (2014). “Electrical resistivity tomography technique for landslide investigation: A Review.” *Earth-Science Reviews*, 135, 65–82.

Perry, J. (1994). “A technique for defining nonlinear shear strength envelopes, and their incorporation in a slope stability method of analysis.” *Quarterly Journal of Engineering Geology and Hydrogeology*, 27(3), 231–241.

Pietruszczak, S. and Mróz, Z. (1981). “Finite element analysis of deformation of strain-softening materials.” *Int. Jour. for Numerical Methods in Engineering*, 17(3), 327-334.

Pinzón, L. A., Mánica, M. A., Pujades, L. G., and Alva, R. E. (2020). “Dynamic soil-structure interaction analyses considering directionality effects.” *Soil Dynamics and Earthquake Engineering*, 130, 106009.

Potts, D., Dounias, G., and Vaughan, P. (1990). “Finite element analysis of progressive failure of Carsington embankment.” *Géotechnique*, 40(1), 79-101.

Price, A.B., Boulanger, R.W., DeJong, J.T., Parra Bastidas, A.M., and Moug, D. (2015). "Cyclic strengths and simulated CPT penetration resistances in intermediate soils." *Proc. 6th Int. Conf. on Earthquake Geotechnical Engineering*, November 14, Christchurch, New Zealand

Ramiah, B. K., Purushothamaraj, P., and Tavane, N. G. (1973). “Thixotropic effects on residual strength of remoulded clays.” *Indian Geotech. J.*, 3(3), pp. 189–197.

Reza Tabatabaiefar, S. H., Fatahi, B., and Samali, B. (2013). “Seismic behavior of building frames considering dynamic soil-structure interaction.” *International Journal of Geomechanics*, 13(4), 409–420.

Robertson, P. K. (1990). “Soil Classification using the cone penetration test.” *Canadian Geotechnical Journal*, 27(1), 151–158.

Robertson, P.K. (2009). “CPT interpretation – a unified approach.” *Canadian Geotechnical Journal*, 46: 1-19

Rocscience Inc. (2021). “Slide 2 Version 9.013 - 2D limit equilibrium analysis for slopes.” www.rocscience.com, Toronto, Ontario, Canada.

Scaringi, G. and Di Maio, C. (2016). “Influence of displacement rate on residual shear strength of clays” *Procedia Earth Planet. Sci*., 16, pp. 137-145.

Schmertmann, J. (1978). “Guidelines for CPT: performance and design.” *Report FHWA-TS-78-209*, Federal Highway Administration, p 145.

Seidalinov, G. and Taiebat, M. (2014). “Bounding surface SANICLAY plasticity model for cyclic clay behavior.” *Int. J. Numer. Anal. Meth. Geomech.,* 38: 702–724. doi:10.1002/nag.2229

Septanika, E., Thakur, V., Brinkgreve, R.B.J., and Nordal, S. (2007). “Modelling undrained instability in geomaterial using extended finite element method (PUX/XFEM).” *Proc. Int. Geomechanics Conf.*, Nessebar, Bulgeria

Shannon and Wilson (1964). “Report on Anchorage area soil studies.” *Rep. to USACE District, Anchorage, Alaska*. Contract no. DA-95-507-CIVENG-64-18.

Skempton, A. W. (1970). “First-time slides in over-consolidated clays.” *Géotechnique*, 20(3), 320–324.

Skempton, A. W. (1977). “Slope stability of cuttings in brown London clay.” *Proc., 9th Int. Conf. on Soil Mech. and Found. Eng.*, Vol. 3,

Tokyo, 261–270.

Skempton, A. W. (1985). “Residual strength of clays in landslides, folded strata and the Laboratory.” *Géotechnique*, 35(1), 3–18.

Soga, K., Alonso, E., Yerro, A., Kumar, K., and Bandara, S. (2016). “Trends in large-deformation analysis of landslide mass movements with particular emphasis on the material point method.” *Géotechnique*, 66(3), 248–273.

Spencer, E. (1967). “A method of analysis of the stability of embankments assuming parallel inter-slice forces.” *Géotechnique*, 17(1), 11–26.

Stark, T. D., & Vettel, J. J. (1992). “Bromhead Ring Shear Test Procedure.” Philadelphia: American Society for Testing and Materials.

Stark, T.D. and Contreras, I.A. (1996). “Constant Volume Ring Shear Apparatus.” *Geotechnical Testing Journal.,* 19(1), 3-11.

Stark, T.D. and Contreras, I.A. (1998). “Fourth Avenue landslide during 1964 Alaskan Earthquake.” *J. of Geotech. and Geoenviron. Eng.,* 124(2), 99–109.

Stark, T. D., Choi, H., and McCone, S. (2005). “Drained shear strength parameters for analysis of landslides.” *Journal of Geotechnical and Geoenvironmental Engineering*, 131(5), 575–588.

Stark, T. D., and Hussain, M. (2010). “Shear strength in preexisting landslides.” *Journal of Geotechnical and Geoenvironmental Engineering*, 136(7), 957–962.

Stark, T. D., Beaty, M. H., Byrne, P. M., Castro, G., Walberg, F. C., Perlea, V. G., Axtell, P. J., Dillon, J. C., Empson, W. B., and Mathews, D. L. (2012). “Seismic deformation analysis of Tuttle Creek Dam.” *Canadian Geotechnical Journal*, 49(3), 323–343.

Taiebat, M., Kaynia, A.M., and Dafalias, Y.F. (2011). “Application of an anisotropic constitutive model for structured clay to seismic slope stability.” *J. of Geotech. and Geoenviro. Eng.*, 137(5), 492–504.

Taipodia, J., Baglari, D., and Dey, A. (2018). "Recommendations for generating dispersion images of optimal resolution from active MASW survey." *Innovative Infrastructure Solutions*, 3(1).

Taipodia, J., and Dey, A. (2018). "Impact of strike energy on the resolution of dispersion image in active MASW survey." *Proceedings of GeoShanghai 2018 International Conference: Multi-physics Processes in Soil Mechanics and Advances in Geotechnical Testing*, 419–427.

Tang, D., Jiang, Z., Yuan, T., and Li, Y. (2020). "Stability Analysis of soil slope subjected to perched water condition." *KSCE Journal of Civil Engineering*, 24(9), 2581–2590.

Thakur, V., Nordal, S., Jostad, H.P., and Andresen, L. (2005). "Study on pore water pressure dissipation during shear banding in sensitive clays." *11th Int. Conf. on Computer Methods and Advances in Geomech.,* G Barla and M Barla Eds, Vol. 4, 289-296

Thakur, V. (2006). "Shear band analyses in sensitive soft clays using inherent regularization technique." *Proc. The 17th European Young Geotechnical Engineers Conference*, Zagreb, Croatia, pp: 247-260

Thakur, V., Grimstad, G., and Nordal, S. (2006). "Instability in sensitive soft clays." *Proc. ECI: geohazards and risk evaluation conference*, Farrokh Nadim, Rudolf Pöttler, Herbert Einstein, Herbert Klapperich, and Steven Kramer Eds., ECI Symposium Series, Norway, Vol. P7

Thakur, V. (2007). "Strain localization in sensitive soft clays." Dissertation, Norwegian Univ. of Science and Technology, Trondheim. Norway

Thakur, V., Nordal, S., G. Viggiani, G., and P. Charrier, P. (2017). “Shear bands in undrained plane strain compression of norwegian quick clays.” *Canadian Geotechnical Journal*, 55(1):45–56, 2017.

Tiwari, B., Pradel, D., Ajmera, B., Yamashiro, B., and Khadka, D. (2018). “Landslide movement at Lokanthali during the 2015 earthquake in Gorkha, Nepal.” *Journal of Geotechnical and Geoenvironmental Engineering*, 144(3), 05018001.

Travasarou, T., Bray, J. and Abrahamson, N. (2003). “Empirical attenuation relationship for Arias Intensity.” *Earthquake Engineering & Structural Dynamics*, 32(7),1133-1155.

Tsiambaos, G., and Sabatakakis, N. (2010). “Empirical estimation of shear wave velocity from in situ tests on soil formations in Greece.” *Bulletin of Engineering Geology and the Environment*, 70(2), 291–297.

Updike, R.G. (1984). "The Turnagain Heights landslide—an assessment using the electric cone penetration test." *Alaska Division of Geological and Geophysical Surveys*, Report of Investigations 84 13, 48.

VandenBerge DR, Duncan JM, Brandon TL (2013). “Fully softened strength of natural and compacted clays for slope stability.” In: *Geo-congress 2013, stability and performance of slopes embankments III*, pp 221–233

VandenBerge, D. R., Castellanos, B. A., and McGuire, M. P. (2018). “Comparison and use of failure envelope forms for slope stability analyses.” *Geotechnical and Geological Engineering*, 37(3), 2029–2046.

VandenBerge, D. R., and McGuire, M. P. (2019). “Practical use of Modified hoek–brown criterion for soil slope stability analysis.” *Geotechnical and Geological Engineering*, 37(6), 5441–5455.

Viggiani, G., Finno, R.J., Harris, W.W. (1994) “Experimental observations of strain localization in plane strain compression of a stiff clay.*” Localization and Bifurcation Theory for Soils and Rocks*, R. Chambon, J.Desrues & I. Vardoulakis editors, Balkema: 189-198

Vucetic, M. and Dobry, R. (1991). "Effect of soil plasticity on cyclic response." *J. Geotech. Engrg.,* 10.1061/(ASCE)0733-9410(1991)117:1(89).

Wakai, A., Cai, F., Ugai, K., Soda, T. (2014). “Finite element simulation for an earthquake-induced catastrophic landslide considering strain-softening characteristics of sensitive clays.” *Proceedings: World Landslide Forum 3*, Beijing

Wathelet, M.,(2005). “Array recordings of ambient vibrations:surface-wave inversion.” Ph.D. thesis. Faculté des Sciences Appliquées, Liege University, Belgium.

Wolff, T. F. (1989). “Pile capacity prediction using parameter functions.” *ASCE Geotechnical Special Publication No. 23*, 96–107

Wood, D. M. (1990). *Soil behavior and critical state soil mechanics*, Cambridge University Press, Cambridge, U.K

Wood, D. M. (2014). *Geotechnical Modelling*. CRC Press, Florence

Woodward-Clyde Consultants (1982). "Anchorage Office Complex, Geotechnical Investigation, Anchorage, Alaska." *Rep. to Alaska DOT. and Public Facilities, Design and Constr.,* Anchorage, Alaska.

Wright, S.G., Zornberg, J.G., Aguettant, J.E. (2007). “The fully softened shear strength of high plasticity clays.” Center for Transportation Research, University of Texas at Austin, Austin

Xuan, M., Montgomery, J., Anderson, J.B. (2021). “Examining the effects of suction and nonlinear strength enve-lopes on the stability of a high plasticity clay slope.” *Geosciences*.

Yaşar, E., and Erdoğan, Y. (2004). “Estimation of rock physicomechanical properties using hardness methods.” *Engineering Geology*, 71(3-4), 281–288.

Yu, Y., Damians, I. P., and Bathurst, R. J. (2015). “Influence of choice of FLAC and PLAXIS interface models on reinforced soil–structure interactions.” *Computers and Geotechnics*, 65, 164–174.

Zabolotnii, E., Morgenstern, N. R., and Wilson, G. W. (2021). “Mesh sensitivity in numerical models of strain-weakening systems.” *Computers and Geotechnics*, 136, 104253.